ABSTRACT

Title of Dissertation: *IN VIVO* BIODISTRIBUTION, LUNG TARGETING, AND PARAMETRIC MODULATION OF A DNA-BASED DRUG DELIVERY SYSTEM ADDRESSED TO ICAM-1

Nikša Roki, Doctor of Philosophy, 2020

Dissertation directed by: Associate Research Professor, Silvia Muro, Institute for Bioscience and Biotechnology Research

The design goal of ligand-targeted nanoparticles (NPs) is to achieve site-specific targeting to specific biological targets, which can maximize therapeutic efficacy and safety. However, site-specific delivery remains suboptimal due to biological barriers, particularly non-specific interactions and sequestration of NPs by the immune system and anatomic structures of clearance organs *in vivo*. This formidable challenge prompted the exploration of novel ligand-based NP designs. Due to their exceptional precision, versatility, and biocompatibility, NPs composed of DNA (DNA-NPs) and targeted via ligands, have emerged as a promising strategy to deliver therapeutic effects with unique precision. One such formulation is anti-ICAM/3DNA, a multibranched DNA-made nanocarrier (3DNA®) functionalized with antibodies (Abs) against intercellular adhesion molecule-1 (ICAM-1), a cell surface glycoprotein accessible for targeting from the bloodstream and overexpressed in the lungs in many diseases. In particular, a prototype formulation of anti-ICAM/3DNA had demonstrated high cell-specific targeting and therapeutic potential *in vitro*. In this dissertation, we explored the kinetics, biodistribution, and lung-specific targeting *in vivo* of a new anti-ICAM/3DNA design that enabled precise surface functionalization with Abs to provide and modulate targeting. In Aim 1, we modified a radiotracing-based method to correct ^{125}I-NP biodistribution results by separating the signal arising from the free ^{125}I label, providing more accurate measurements of the NP biodistribution. In Aim 2, intravenous injection of anti-ICAM/3DNA in mice resulted in profuse and specific lung targeting, which had an unprecedently high specificity index over non-specific control. In Aim 3, we demonstrated that below the lung delivery saturation conditions and within the

parametric range tested, anti-ICAM density on 3DNA played a key role in modulating lung specificity compared to the dose concentration and size of anti-ICAM/3DNA. Additionally, we estimated how this would impact targeting of drugs that can be intercalated into the DNA carrier core or linked to carrier outer arms. Overall, this study demonstrates that anti-ICAM/3DNA bio-physicochemical properties allow for efficient, specific, and tunable lung targeting. This new knowledge will help guide future DNA-NP designs for targeted therapeutic delivery and set the basis for investigational applications aimed at the treatment of pulmonary diseases.

IN VIVO BIODISTRIBUTION, LUNG TARGETING, AND PARAMETRIC MODULATION OF A DNA-BASED DRUG DELIVERY SYSTEM ADDRESSED TO ICAM-1

by

Nikša Roki

Dissertation submitted to the Faculty of the Graduate School of the University of Maryland, College Park, in partial fulfillment of the requirements for the degree of

Doctor of Philosophy

2020

Advisory Committee:
Professor Silvia Muro, Co-Chair
Professor William E. Bentley, Co-Chair
Dr. Robert Getts
Professor Peter Kofinas
Professor Yu Chen

Dedication

This work is dedicated to my wife, Rithu, for her love, encouragement, and endless support. Thank you for being by my side every step of the way.

Acknowledgements

First and foremost, I would like to thank my mentor and advisor, Dr. Silvia Muro. Your expertise in drug delivery combined with your passion for research is inspiring. Thank you for always encouraging me and pushing me to be my best. Your guidance and mentorship during my years at The University of Maryland has helped me hone my skills and knowledge to become a better researcher. I am also thankful for all the present and past Muro Lab members, especially Dr. Melani Solomon, Dr. Kevin Gray, Dr. Rachel Manthe, Dr. Zois Tsinas, Dr. Eameema Muntimadugu, and Dr. Edgar Herrero. I could not have asked for a better lab team and am thankful for your friendship and support. I am truly appreciative that my graduate work was supported by the University of Maryland Graduate Assistantship, Genisphere® LLC Graduate Fellowship, the Ann G. Wylie Semester Dissertation Fellowship, and Dr. Muro's National Institute of Health Award HL098416.

My heartfelt thanks go to Dr. Silvia Muro, Dr. Melani Solomon, Dr. Robert Getts, and Jessica Bowers for assisting me in the completion of this work. Thank you to all my committee members, Dr. William Bentley, Dr. Robert Getts, Dr. Peter Kofinas, and Dr. Yu Chen. I am truly grateful for all your insight, guidance, and time.

I am very grateful to the Genisphere® LLC team for always providing mentorship and support. I am truly honored to have had the opportunity to collaborate with Dr. Robert Getts, Jessica Bowers, Dr. Lori Getts, and Lou Casta and learn about

one of the most exciting drug delivery platforms, 3DNA. Thank you for providing me with the opportunity to be part of an innovative research project supported by great collaborative teamwork.

I would also like to thank the wonderful friends I have made during my graduate studies. Kevin, thank you for showing me the countless opportunities to grow as a researcher and entrepreneur and for being a wonderful friend. Melani, thank you for your boundless positive energy, kindness, and guidance. Rachel, thank you for your generosity, hard work, and for always believing in me. Eric, you are one of the smartest and most wonderful people I have ever met. I enjoyed all our workouts, lunch breaks, and in-depth conversations. Simon, thank you for being a great friend. Bentley lab members, Eric, Kristina, Ashley, Chen-Yu, Sally, Donna, thank you for all the laughter and good times.

Finally, I would like to thank my family for all their love and support in helping me follow my dreams. I love you and would not be where I am today without all of you. To my parents, Luko Tata and Milana Mama, thank you for your boundless love, for instilling in me good beliefs and values, and for helping me achieve my goals of being an Olympian and a research scientist. Antonio, thank you for always being there. Your determination and passion are inspiring, and I am so proud that you are my brother. Thank you, Rama Amma, Murli Appa, and Loki, for all the long talks, encouragement, and laughter even through the tough times. To my wife, Rithu, you are

the joy of my life. Thank you for all your love, unwavering support, for always putting a smile on my face, and for championing me to be my best.

Table of Contents

List of Tables

List of Figures

List of Abbreviations

Ab……..Antibody

Ab-oligo……..Antibody-oligonucleotide

ADC…….Antibody-drug conjugate

Anti-ICAM……...(IgG) antibody targeted to intercellular adhesion molecule-1

Anti-ICAM/3DNA……..Antibody-DNA multivalent nanoconstruct targeted to intercellular adhesion molecule-1

Anti-ICAM-oligo……Oligonucleotide conjugated antibody targeted to intercellular adhesion molecule-1

Anti-ICAM/PLGA……..Antibody-PLGA nanoconstruct targeted to intercellular adhesion molecule-1

Anti-PECAM-1……...Polyclonal antibody against platelet-endothelial cell adhesion molecule-1

AUC……....Area under the curve

BCA……...Bicinchoninic acid

BSA……..…….Bovine Serum Albumin

BW……..…Body Weight

CAM……...Cell adhesion molecule

COPD…….Chronic obstructive pulmonary disease

CPM……..…..Counts per minute

Cy3……Cyanine 3 dye

DAPI……...4′,6-diamidino-2-phenylindole

DLS……...Dynamic light scattering

DNA…….Deoxyribonucleic acid

EDTA……Ethylenediaminetetraacetic acid

FITC……..Fluorescein isothiocyanate

4L……..…Four layer 3DNA

h…….Hour/s

H&E stain……Hematoxylin and eosin stain

^{125}I……..……Iodine-125

ICAM-1……..Intercellular adhesion molecule-1

IgG…….Immunoglobulin G

IgG-oligo……...Immunoglobulin G conjugated oligonucleotide

I.V…….Intravenous

LC-SMCC…….Succinimidyl 4-(N-maleimidomethyl)cyclohexane-1-carboxy-(6-amidocaproate)

LR……..…..Localization ratio

MARCO……...Macrophage receptor with collagenous structure

MRT……....Mean residence time

min…….Minute/s

MW……..Molecular weight

MWCO…….……Molecular weight cut-off

NC…….……Nanocarrier

NHE……....Sodium-hydrogen antiporter

NIS……..Sodium-iodide symporter

NP[a]……...……Nanoparticle

NHE……...…….Na^+/H^+ exchanger

NHS……N-Hydroxysuccinimide

Oligo…….DNA Oligonucleotide

PBS…….…….Phosphate buffered saline

PDI……...Polydispersity index

%ID……...……..Percent injected dose in the whole blood or organ

---

[a] NP in this thesis encompasses the simple and lose definition of objects or energy in the 1 nm to around 100-1000 nm size-range regardless of their aspect ratio. This includes nanomedicines, nanopharmaceuticals, nanotherapeutics, nanocarriers, nanodevices, and anything associated with the nanoscale regardless of the origin, physical form, or function.

%ID/g…….Percent injected dose per gram of blood or organs

PECAM-1…….....Platelet-endothelial cell adhesion molecule-1

PLGA…….…….Poly(lactic-co-glycolic acid)

RNA…….….Ribonucleic acid

RPM……Revolutions per minute

RT……...Room temperature

SD……...……Standard deviation

SEM……..…….Standard error of the mean

SI……..….Specificity index

SR……..Scavenger receptor

TCA……..Trichloroacetic acid

TCEP……..Tris(2-carboxyethyl)phosphine

TLR……..Toll-like receptor

Tm……...Melting temperature

Tris……..Tris(hydroxymethyl)aminomethane

t(1/2)……...…Half-life

3DNA® (3DNA)……..…Three-dimensional, nanoscale, multivalent scaffold made from proprietary, synthetic DNA formed in a flexible, branched structure

2L……..Two layer 3DNA

vs…….…..Versus

Chapter 1: Motivation and Goals

Targeted nanoscale particles (i.e., nanoparticles, NPs), including drug nanocarriers (NCs) and nanomedicines, can be used to improve biodistribution of drugs to specific sites within the body[1,2] and can have a tremendous impact in patient treatment, particularly in the areas of oncology, inflammation, and autoimmune diseases.[3–8] Localized drug delivery via targeted NPs can reduce the: 1) needed administration dose, 2) systemic drug exposure, 3) off-site drug delivery, and 4) concomitant side effects due to the potential off-site toxicity.[4,9,10] Targeted injectable therapeutics represent > $10 billion market in the US, with the projected growth of ~5-18% annually.[11,12]

An ideal targeted NP for therapeutic use consists of a drug and other NP materials whose functions are to promote precise spatiotemporal delivery (i.e., in the specific cellular or extracellular location and during a particular time) of drugs in correct therapeutic amounts. To accomplish this epitome, NP materials need to redirect the bio-physicochemical properties of therapeutic molecules to help them conform to the specific and distinct requirements associated with the pathology of a disease, and the requirements of the chosen delivery route (e.g., intravenous, I.V. route). These bio-physicochemical properties are associated with NP composition, structure, size, shape, surface character (e.g., targeting moieties and their presentation), dosage, etc., which profoundly influence the biodistribution of drugs.[13–18] As such, several nanomaterials

have the potential to provide many important functions, spanning drug targeting, improved drug solubility, increased drug carrying capacity, controlled drug release, controlled degradation, bioactivity, toxicity, etc.[1,7,10,19–31]

Both passive and active targeting mechanisms have been employed in the clinics to improve drug delivery and reduce side effects of nanomedicines (e.g., Doxil, Abraxane, Patisiran, various antibody-drug conjugates, etc.).[32,33] The most common strategy to achieve active targeting is through utilization of moieties that can target specific cell-surface molecules preferentially expressed at the sites of interest within the body; for example, antibody-drug conjugates (ADCs) contain antigen binding sites (i.e. targeting moieties) that can bind specific biological markers.[34–37] Despite the successful translation of these useful targeting technologies, drug delivery remains suboptimal for many therapeutic NPs which require additional or improved functionalities to overcome physiological barriers at the blood, organ, cell, and subcellular level.[2,4,10,13,19,37–45] For example, formulations such as ADCs generally lack protective function to prevent premature degradation of drugs and have limited drug carrying capacity, limited size options, etc.[42] These functions are particularly necessary for the delivery of biotherapeutics which are prone to premature degradation upon their administration,[1,22,46–56] and have difficulty in overcoming physiological barriers such as the immune system, endothelial linings, and cell and intracellular membranes.[46,57–65] Consequently, the clinical translation for a plethora of therapeutic NPs is hindered due to lack of aforementioned functionalities. Additional challenges for NPs include

lack of uniform and precise size, shape, and number of targeting moieties, as well as complex and unpredictable interactions with the biological environment *in vivo*, which hinder their performance.[1,10,29,31,32,45,66–72]

Under these considerations, many novel nanomaterials with robust and unique functionalities have been developed. NPs constructed from deoxyribonucleic acid (DNA-NPs[b]) have sparked interest in drug delivery due to their exceptional versatility, reproducibility, tunability and precision of their architecture down to a single atom definition, as well as their built-in responsiveness to various physiological cues (e.g., pH, temperature etc.).[19,20,73,74] Consequently, DNA-based NPs can deliver therapeutic effects with unique level of precision and programmability, which has not currently been achieved for other NPs,[27,39–41,75–80] and are starting to emerge as a relatively safe and promising technology to help overcome physiological barriers.[20,41,58,61,81–88] Another unique functionality of DNA-NPs, particularly relevant in oncology applications, is their capacity to intercalate anthracycline drugs such as doxorubicin.[81] Furthermore, drugs such as gene regulating molecules, protein, and small drug therapeutics can also be hybridized via oligonucleotide linkages or directly coupled to NPs.

[b] Many unique properties of DNA-NPs are also shared with RNA made NPs.

While DNA-NPs offer versatile functionalities that are still being explored, their specific targeting has been accomplished with limited success, particularly *in vivo*, due to novelty of the field. Hence, the goal of this dissertation is to explore and design the targeting functionality of DNA-NPs through parametric modulation of their properties such as the specificity, number, and density of their surface antibodies (Abs), their size, and their concentration. 3DNA®[c] NC, a DNA-made and stably crosslinked tridimensional (3D) scaffold, is a good candidate to explore targeting functionalities of DNA-NPs because it has precise and tunable size and surface topography of outer areas.[89] 3DNA is a repetitively branched construct that can be coupled with a precise number and spatial arrangement of oligonucleotide-conjugated molecules (e.g., targeting molecules, therapeutics, etc.) on its peripheral regions, controlled through complementary DNA hybridization.[19,89–92] Molecules can also be directly conjugated to the outer ends of 3DNA, while intercalating drugs can be incorporated within the core 3DNA scaffold.[91,93]

A good target to test I.V. targeting functionalities of DNA-NPs is intercellular adhesion molecule-1 (ICAM-1) because it is accessible from the circulation and expressed on the surface of the endothelium.[2,7,14,94–105] Since there is an abundance of

[c] 3DNA® are proprietary designs by Genisphere® LLC and were manufactured and provided by Genisphere® LLC under an agreement with the University of Maryland for the studies described in this dissertation.

endothelium in the lungs,[106,107] there is also high ICAM-1 content,[96,99,107,108] making the lungs a primary target.[7,99] ICAM-1 is a transmembrane glycoprotein located on the surface of various cell types, and it is overexpressed in inflammation.[7,107] Hence, it is a particularly promising target for specific delivery to diseased sites. ICAM-1 can be targeted with anti-ICAM ligands of various types, including Abs, peptides, aptamers, etc. Many cases of anti-ICAM functionalized NPs have been shown to provide enhanced specific targeting to ICAM-1 compared to anti-ICAM ligands alone, due to their distinct bio-physicochemical parameters affecting their binding interactions and transport.[7,95,109] The enhanced specificity and avidity of NP binding to ICAM-1 is due to the inflammation-induced ICAM-1 overexpression and their improved ligand presentation (e.g., localized ligand density and multivalent binding) at the NP-cell interface. Moreover, the biodistribution of ICAM-1-targeted NPs has been extensively characterized, providing a benchmark model to evaluate ICAM-1 targeting of DNA-NPs.[7]

Our laboratory has shown that Abs against ICAM-1 (anti-ICAM) can provide specific, highly efficient targeting functionality to prototype 3DNA[d] in endothelial and other cell types *in vitro*.[58] The work in this dissertation focuses on exploring targeting efficiency and specificity of various new anti-ICAM/3DNA formulations *in vivo*[110]

[d] The results for the prototype anti-ICAM/3DNA *in vivo* are published here[110].

which have not been previously tested *in vitro* or *in vivo*. Based on the promising targetability of anti-ICAM/3DNA in the endothelial cell culture model, the high endothelial and ICAM-1 content in the lungs, and currently published research supporting high lung accumulation of multivalently targeted anti-ICAM NPs, in this study we hypothesized that multivalent anti-ICAM/3DNA would allow for efficient and ICAM-1-specific lung targeting *in vivo*. We also explored the effects of targeting valency (i.e. number of Abs per NP), valency density (number of Abs per NP surface), anti-ICAM/3DNA size and dose concentration, on the efficacy of anti-ICAM/3DNA targeting and biodistribution to the lungs and other sites within the body. In addition, we estimated the relevance of the aforementioned targeting and biodistribution in delivery through two distinct modes of drug cargo incorporation: carrying within core 3DNA scaffold and linking to peripheral 3DNA regions. To accurately evaluate the radiotracing-based biodistribution of radiolabeled anti-ICAM/3DNA without confounding effects of the potential release of label, we first tested the modification of a biodistribution method with trichloroacetic acid (TCA) precipitation assay commonly used to separate free label. Various anti-ICAM/3DNA formulations were injected I.V. in healthy mouse models to assess the hypothesis in the following aims:

Specific Aim 1: Improve a radiotracing-based method for measurements of *in vivo* biodistribution.

Specific Aim 2: Evaluate the biodistribution and targeting specificity of anti-ICAM/3DNA *in vivo*.

Specific Aim 3: Decipher the role of targeting valency, valency density, size, and dose of ICAM-1-targeted 3DNA in biodistribution and specific targeting, and ultimate impact on drug delivery *in vivo*.

This dissertation is organized in eight chapters. Chapter 1 introduces the motivations and goals of this dissertation. Chapter 2 reviews the relevant background information regarding NP properties that are involved in targeting and biodistribution via the IV route. It also describes the clinical relevance of DNA NPs, particularly 3DNA and ICAM-1 targeting. Chapter 3 contains the significance and innovation of the study performed for this dissertation. Chapter 4 encompasses materials and methods used throughout Aims 1-3. In Chapter 5, we describe the modification of a radiotracing method in order to improve tracing of biodegradable NPs I.V. administered in a healthy mouse model *in vivo* and improve the robustness of biodistribution measurements. In Chapter 6, we utilize the improved radiotracing method to test whether anti-ICAM/3DNA targeting functionality can be successfully used in a healthy mouse model *in vivo*, by looking at biodistribution and targeting specificity compared to non-specific control formulations. In Chapter 7, we explore how parametric dependencies of properties such as NP targeting valency, valency density, NP size and dose concentration modulate anti-ICAM/3DNA targeting in a mouse model *in vivo*. In Chapter 8, we conclude the dissertation with final remarks and future directions.

Chapter 2: Background

2.1. Bio-Physicochemical Properties and Drug Delivery Functions of Targeted Nanoparticles

2.1.1. Design Considerations

In order to ameliorate their delivery, drugs benefit from augmentation of their properties with new functionalities provided by NPs.[2,10,19,32,37,111,112] As mentioned in the Motivation and Goals section, nanomaterials are used for various components of NPs that provide functions such as that of a scaffold, drug carrier, providing drug protection and solubility, controlled drug release, targeting, and even altering intracellular fate and function, to mention a few (**Figure 1**).[48,58,113,114] These new functions can not only improve the therapeutic efficacy and safety of currently approved drugs, but can provide the opportunity to reevaluate drugs previously deemed unusable in the clinical setting.[2,10,19,37]

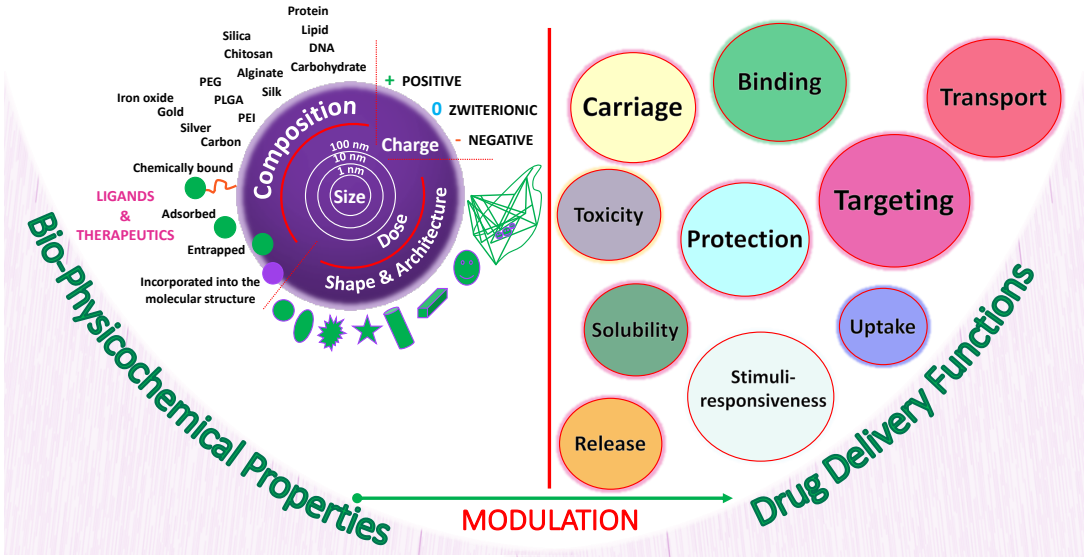

Figure 1. Bio-physicochemical properties and drug delivery functions of NPs.
NPs have unique bio-physicochemical properties that can be tuned to modulate drug delivery functions and improve therapeutic outcomes. Modulating NP composition, dose, drug loading and release mechanisms, size, shape, charge, ligands such as targeting molecules can modulate drug carriage, targeting, protection, solubility, responsiveness to physiological stimuli, and others.

Furthermore, NPs have unique and versatile bio-physicochemical properties that can be tuned in order to modulate the aforementioned drug delivery functions and further improve therapeutic outcomes.[10,21,26,30,66,115–122] For example, in addition to controlling their dose and composition, NPs can have different drug loading and release mechanisms, as well as different size, shape (e.g., spheres, cubes, stars), and surface features (e.g., charge, topography of molecules and ligands with various functions, etc.) which can all modulate drug delivery.[28,100,123,1249,125]

Surface ligands that can direct specific interactions of NPs with the biological environment (e.g., Abs) are particularly useful in boosting targeting and site-specific

drug delivery, as demonstrated by our and many other laboratories.[2,10,19,37,44,60,67,120,126–129] Moreover, the presentation of these targeting ligands (e.g., their surface density and number), as well as the size and dose of NPs, are additional factors modulating their targeted drug delivery.[13,14,29,43,45,75,95,115,130] For successful organ targeting, the total binding strength (referred to as avidity) must overcome resistive forces such as the thermal motion of NPs, blood flow shear stress, membrane undulations, and membrane elasticity.[2,131,132]

Modulation of targeting and other bio-physicochemical properties related to drug delivery greatly depend on the chosen materials and the overall composition of NPs.[19,28,70,133–136] NPs made of fatty-, amino-, and nucleic- acids, metals, carbon, silica, etc. have all been investigated to improve biodistribution and targeted drug delivery (**Figure 2**).[28,30,37,121,121,137–144] So far, only phospholipid-based (e.g., Doxil and Patisiran) and amino acid (protein)-based formulations (e.g., Abraxane and ADCs) have been approved for clinical use as mentioned in the Motivation and Goals.[37] Indeed, NP material and composition is one of the fundamental design considerations, impacting overall therapeutic performance, including the safety and regulatory aspects.[23,145,146] The materials used also influence the production of NPs,[49,75,147] pertaining to their cost, scalability, reproducibility, uniformity, etc.[74,148,149] As discussed in more detail later in the Background section, DNA-based devices hold great promise in drug delivery as they provide unprecedented control over their design and bio-physicochemical properties compared to other NPs.[19,57,119]

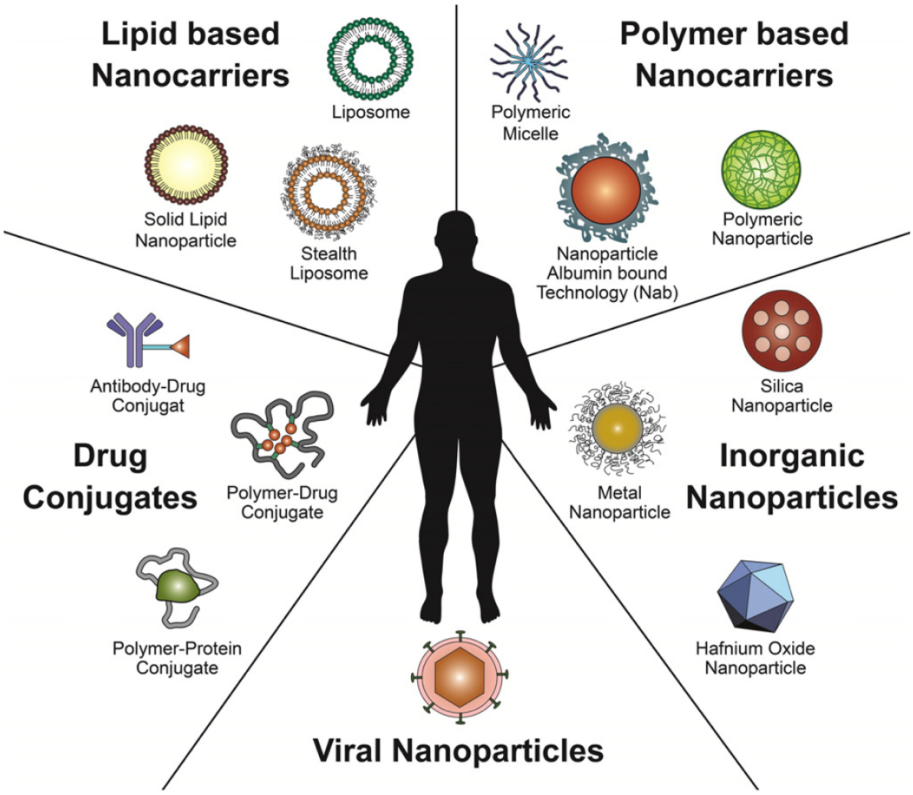

Figure 2. Common NPs and NP materials used in drug delivery.
Shown are some of the materials, their form and composition used in biomedical applications, some of which are inspired by natural NPs.[37] Reprinted with permission.[e]

The targeting functionalities associated with many NP properties are still not well understood due to the complexity associated with both the NPs and the *in vivo* environment, but also the lack of standardized measurements of various aspects of NP

[e] Reprinted from Journal of Controlled Release, 200, Wicki A, Witzigmann D, Balasubramanian V, Huwyler J., Nanomedicine in cancer therapy: challenges, opportunities, and clinical applications, 138-57, 2015, with permission from Elsevier.

performance with respect to their stability, transport, specific targeting, etc. in cell culture and animal models. Nevertheless, their benefits necessitate a discussion of what is currently known, which is presented in this chapter. A particular focus is on the properties explored in this thesis, which are known to affect biodistribution and the targeting at the organ level, pertaining to 1) the specific ligand-based binding interactions, 2) the density and the number of available sites for binding, 3) the overall NP size, and 4) the NP dose.

Lastly, while reformatting biotherapeutics into NPs can provide known beneficial functions such as targeting and protection from premature degradation, it is still desirable to utilize functions of the I.V route pertaining to direct access to the cardiovascular delivery system. Doing so can reduce the complexity of the drug delivery design and shorten the path to the target sites accessible from the bloodstream.[2,10,23,24,150] As such, the I.V. route was utilized in this work. Hence, this section reviews primary design considerations utilized in this thesis for ligand-based NP targeting to the endothelium, their drug delivery functions, and from the aspect of the I.V. administration route whenever applicable.

2.1.2. Ligand-Based Targeting of Nanoparticles

Ligand-based targeting is one of the most dominant functions that can enhance the site-specific accumulation of NPs. It is also utilized naturally in the body and by some pathogens.[151] This functionality is possible through highly specific interactions

and affinity between targeting ligands that are present on the surface of NPs and cell surface molecules that are predominantly present on the body sites that are intended to be targeted (**Figure 3**).[10] This not only allows for the efficient and specific delivery at the organ level, but also the tissue, cell, and sub-cellular levels.[10,58,75,94,109,122,152–154]

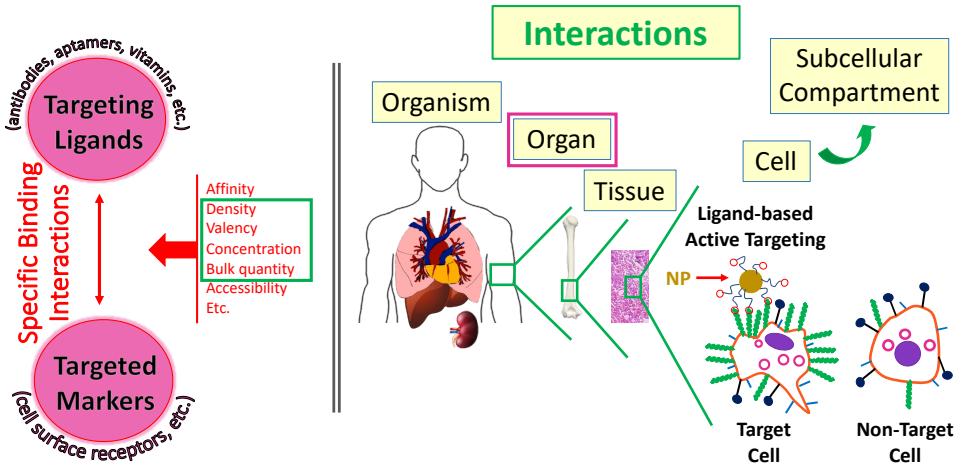

Figure 3. Ligand-based targeting of NPs.
Specific binding interactions between the targeting ligands displayed on the NP surface and targeted biological markers localized on the cell surface can allow for specific accumulation of ligand-coupled NPs and drug delivery at the organ, tissue, cell, and subcellular levels. Ideally, biological markers are predominantly present on target cells but not on the non-target cells. These transport and binding interactions are modulated by ligand affinity, ligand and target accessibility, ligand-NP targeting density, valency, concentration, bulk quantity, etc.

Peptides, vitamins, proteins, Abs, and aptamers are all examples of molecule types that can be used as targeting ligands, but also represent the first examples of targeted nanomedicines (e.g., ADCs, doxorubicin loaded aptamers, etc.).[10] Among these ligands, Abs can be beneficial due to their high affinity and specificity of binding. Accessible targets from the bloodstream encompass several cell types pertaining to the

blood, reticuloendothelial system (phagocytes in liver and spleen), and endothelium.[2] Endothelial targeting of cytokine receptors and cell adhesion molecules (CAMs) is especially attractive as these molecules are upregulated during pathologies such as inflammation, tumor growth, and abnormal changes in the shear stress experienced by the endothelium.[2,155]

Besides the expression profile and accessibility of biological markers, many other factors modulate the behavior of ligand-based targeted NPs pertaining to their circulation time, organ biodistribution, and site-specific targeting.[26,32,108] For example, the specificity and affinity of targeting ligands, their presentation by NPs (e.g., topography, density, and the number of targeting ligands), the size, shape and concentration of NPs, their surface chemistry, etc. all influence the transport and binding phenomena of NPs in the blood and organs.[15,28,30,156,157158]

These NP properties can not only affect specific ligand interactions but can also determine their immunogenicity and recognition by scavenger receptors. Scavenger receptors are involved in the removal of foreign and waste materials, and are mostly present in the spleen and liver.[30,33,123,159,160] For example, neutral or slightly negatively charged NPs with a high surface curvature can generally lower accumulation in the clearance organs (e.g., spleen and liver) by decreasing non-specific binding interactions with proteins and reducing the subsequent binding to cell membranes.[13,161,162] Hence, it is important to optimize the properties of targeted NPs to minimize the non-specific interactions, as they can lead to off-site drug delivery and compromise the therapeutic

efficacy and safety. The following sections focus on the key properties that affect the ligand-based targeting of NPs, specifically the density and the number of targeting moieties presented by the NPs, their size, and their dose.

2.1.3. Ligand Presentation by Nanoparticles: Targeting Ligand Density and Number

The number (i.e., valency, called targeting valency in this dissertation) and density of targeting ligands presented on the surface of NPs (i.e., ligand density, also called targeting density, and referred to as "valency density"[163] in this dissertation from this point onward) play a key role in targeting and biodistribution.[2,67,161,164] For example, with regard to targeting, the intermediate valency density of anti-HER2 and folic acid-targeted NPs (~1×10^4 ligands/μm^2) outperform their counterparts of lower and higher valency density, regardless of cell receptor surface density.[67] Interestingly, although pathogens with different valency densities can enter and be transported to destinations within the body, current data points to viruses having an average valency density on the order of 1×10^4 ligands/μm^2.[120] Nevertheless, the targeting parameters remain inadequately understood. In theory, the perfectly matched presentation of NP targeting moieties to available target molecules in the organs or on the surface of the endothelium can allow for maximal binding and organ targeting.[10,95,102,165] This perfect ligand presentation does not only involve a geometric match, but also involves the probability and equilibrium of successful collision for each ligand, which collectively

become more favorable for multivalent NP binding. The multivalent binding may also provide an advantage for anchoring NPs to the endothelium in terms of counteracting the shear stress and other forces acting against NPs binding to organs, especially for sturdier or larger particles.

Nevertheless, there are several reports showing that overcrowding ligands on the NP surface may in fact negatively impact targeting.[66,166,167] One of the reasons for this may be steric hindrance, which can prevent ligands from achieving the required orientation and/or accessibility for successful collisions with the targeted molecules (**Figure 4A**).[10,166,168] While computer simulations show that this scenario is possible in theory for high density ligand-receptor interactions,[66,120,127] it has been hard to study in practical terms for several reasons. For example, most NPs rely on the random and inconsistent functionalization of surface ligands due to their design capability limitations, preventing evaluation of ligand density and "over-crowding" in a controlled manner. This is further complicated since most studies do not characterize the relation between the valency density and the precision of functionalization, or the relation between the valency density and the affinity or availability of the binding region on the ligand. Namely, the precision, availability, and the affinity of functionalized ligands are usually assumed to stay constant with the modulation of ligand density, but experimental evidence suggests differently, at least for the ligands adsorbed on the NP surface.[166] Only up to 4 % of the surface-adsorbed ligands may have their binding functions preserved, and this drastically drops with the increased Ab

density (**Figure 4B**).[166] This kind of characterization is not commonly performed or reported for targeted NPs, hindering our understanding of NP valency density and targeting valency. Hence, it is unclear whether steric hindrance in such experiments is due to the ligand density or limitations in the precision of ligand functionalization and ligand affinity. Although perfect functionalization may only be possible in theory, one way to better understand valency density-modulated targeting is to keep the relationship constant between the valency density and ligand availability or valency density and ligand affinity. Introducing a controlled minimum distance among ligands on the NP surface can ensure a consistent fraction of available ligands that are displayed on the NP surface, regardless of the valency density and regardless of the orientation of the ligands. As an example, 3DNA arms have precise spacing between the outer arms, and regardless of the ligand orientation, the ligands will still be separated by the minimum distance between the arms. Furthermore, technology that would allow for the functionalization of a single layer of ligands (e.g., Abs) on the NP surface and for ligand coupling to precise or consistent locations on the NP surface, would ensure a consistent fraction of active ligands on the NP surface. For example, 3DNA allows a single layer of ligands to be attached on the surface.

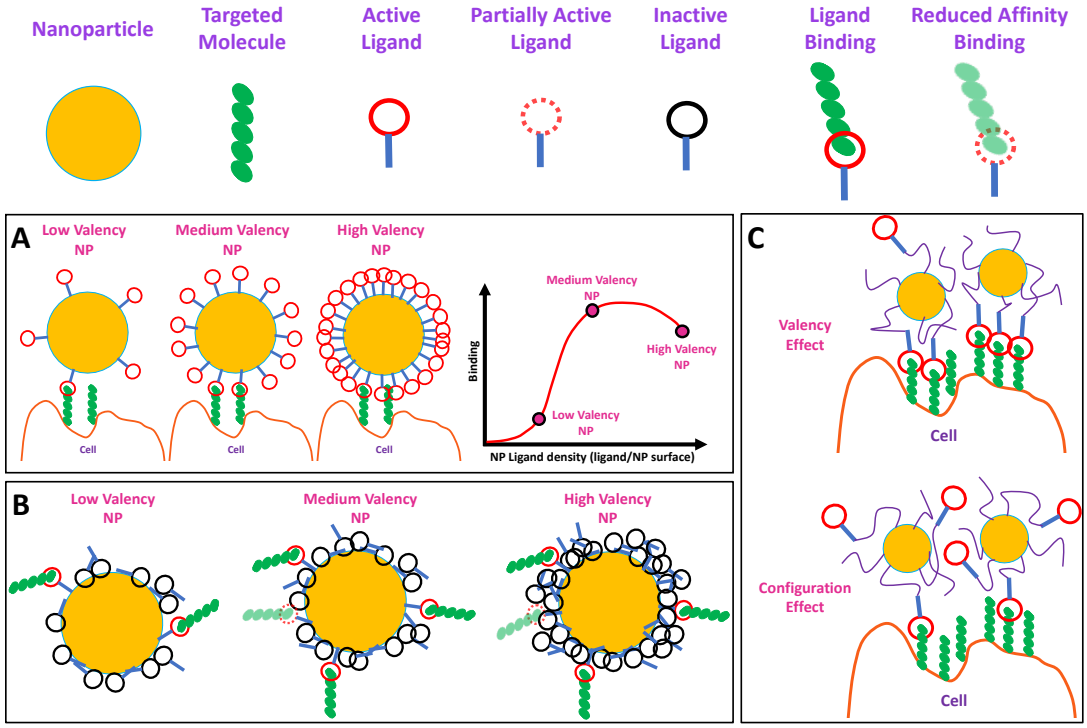

Figure 4. Ligand density functionalization effects related to overcrowding, the activity and orientation of ligands, and mechanisms of binding.

(A) Shown is a potential "classical" steric hindrance effect and the influence of valency on binding, when the NPs are perfectly functionalized.[107] (B) Shown (from left to right) is the influence of Ab surface density on the extent of Ab inactivation due to the adsorption process between the Abs and NPs, reduced percentage of inactivated Abs with an increase in Ab density, but reduced availability for binding due to the steric hindrance effect (i.e., "orientation effect"), and further worsening of Ab availability for binding due to the steric hindrance (i.e., "overlay effect").[166] Note that panels A and B would show similar binding response curves, but the proposed mechanisms take different phenomena into account, including three kinds of steric hindrances. (A) vs. (B) shows the difference between steric hindrance induced by theoretical maximum ligand density as compared to steric hindrance induced by NP design limitation. (C) Higher numbers or density of targeting ligands enhances NP ability to bind to target cells.[169] However, this effect can be contributed to the increased number of binding events per NP resulting in direct multivalent binding (valency effect, shown on the top) or the increased number of possible binding configurations with a single binding event per NP resulting in initial monovalent binding (configuration effect, shown on the bottom).[169] The mechanism of binding for a particular NP design is an important consideration to optimize ligand density.[169]

Interestingly, computational analysis showed that only as little as five Abs were required to be simultaneously engaged in binding in order to overcome counteracting forces and anchor a 1-μm-particle (or three Abs for a 100-nm-particle) at 1 Pa shear stress.[167,170] In contrast, the empirical results from the same study indicated that a much higher binding NP valency was required; at the theoretical maximum of 10 bonds that could be achieved by a 1-μm-particle with 1160 Abs/NP (370 Abs/μm^2), NPs could not achieve specific binding under 1 Pa shear stress and had high detachment rates at low shear stress (i.e. >35% detachment at 0.5 Pa).[170] One of the reasons for this disparity could be that the functionalization techniques may deactivate the binding functions of the ligands (e.g., conformational changes, etc.) as mentioned (**Figure 4B**).[166] Another important consideration for understanding valency density is the degree of freedom for surface ligands as this can influence the perceived or "true" ligand density and change the steric hindrance parameters. For example, ligands presented by flexible tether arms as compared to ligands directly attached to the NP may have better availability for binding, both in terms of the taping space and the binding equilibrium.[127,171]

Another example of why it is difficult to correlate the targeting directly to the valency density parameters alone is because changing the valency density parameter will change at least one other property, despite keeping all the other conditions constant. Namely, valency density on the NP can be modulated while keeping the dose of NP component of the ligand/NP formulation constant, but this will also by default change the total amount of the ligand component of the ligand/NP formulation

administered. From a biological standpoint, this may require the utilization of a higher number of targeted molecules on the endothelium, potentially exceeding their availability and causing a reduction in targeting.[67] Alternatively, if the dose is adjusted to match the total ligand administered, the detected effects of targeting may be due to the modulation of the NP dose. So far, no studies have looked into this *in vivo*.

In addition, and very relevant for understanding the work in this dissertation, the relation between the number of available targets and targeting ligands presented by NPs and the potential saturation condition, may be more prominent for the flexible NPs with ligands attached to theater arms. The flexibility and tether arms can allow for the NP shape to conform the ligand presentation.[169] This can allow the engagement of additional ligands for binding as compared to sturdy NPs that lack the tether arms and whose geometry can prevent the access to additional ligands. In theory, the infinitely flexible NP would allow unlimited accessibility of ligands within the NP volume space (i.e., a very dynamic "surface"), where ligands can be modeled as free ligands restricted within this NP volume. Hence, for flexible systems, an additional way to think about the valency density is valency concentration (i.e., the concentration of ligands within the dynamic NP volume space). This is the key difference between the targeting valency for sturdy NP systems that have well defined surface. The branched DNA construct studied in this dissertation may be unique in this aspect based on its architecture, allowing some level of flexibility. In a flexible system, the "surface" is the function of flexibility, or in the case of the branched DNA construct, function of its

diameter and persistence length of DNA branches, assuming the constant temperature. How much the valency effect vs. the freedom of ligand movement would contribute to targeting would depend on the properties of the NP system and the target marker density. Indeed, for representative flexible NP systems, the analysis of the experimental data indicated that the increase in targeting was due to the increased configurations for the single binding event of multivalent NP as opposed to being due to the multivalent interactions (**Figure 4C**).[169] For additional understanding of multivalent NP binding, please refer to the references used in this section.

Furthermore, while increasing the ligand density may generally improve targeting, it may reduce the selectivity of binding between the healthy and diseased organ phenotypes.[172] Namely, despite the high ligand binding specificity for a particular cell phenotype, expression will also be present in "off-target" healthy cells.[10,59] Lowering NP avidity (i.e. total combined effect of all binding ligands) may circumvent the targeting of "off target" cells and improve the selectivity, while still providing enough strength to bind highly expressing cells. Hence, finding the optimal ligand presentation parameters is necessary for each targeted application. This may not only depend on the state of the target (e.g., healthy vs. pathological expression levels) but may in addition highly depend on its biological nature. From this aspect, some receptors naturally participate in low valency binding of molecules such as growth factors binding to growth factor receptors (e.g., epidermal growth factor) and some cell

receptors participate in high valency binding (e.g., CD11a/CD18 integrins on leukocytes) to the ICAM-1.[2,102,113,132,141,173–176]

2.1.4. Size of Ligand-targeted Nanoparticles

The size of NPs is not only important for organ targeting from the nano-bio interface point of view, but also the anatomical, hydrodynamic and diffusion aspects.[60,125161] The size of a NP determines the curvature of ligand presentation and other surface molecules, as well as many other binding factors related to thermodynamics which consequently affect binding interactions of NPs (both, ligand specific and non-specific) in the blood and organs.[17126,33,123,132]The effects of the curvature are not well understood; nevertheless, most reports show that the interactions get stronger as the curvature decreases.[115,116]

Hydrodynamically, NPs that are larger (also less dense, stiffer etc.) tend to marginate towards the blood vessel walls, while smaller NPs (also denser, softer etc.) tend to distribute randomly and circulate while being trapped in-between red blood cells, which move towards the middle of the blood vessel as they experience lift forces in proximity of the blood vessel walls.[177–179] This aspect determines the probability of NP interactions with the blood vessel walls and binding, in addition to the other aforementioned binding processes.[132,177,179] NPs also experience other size-related hydrodynamic forces (e.g., drag, rotational, etc.) which ultimately affect the stability of organ-bound NPs.

Anatomically, NPs and their degraded fractions that are less than ~10-20 nm in size can clear through the fenestrated endothelium in the kidneys (**Figure 5A**). Similarly, NPs of this size can also be captured by the liver, bone marrow, endocrine and lymphoid organs such as spleen because of their discontinued sinusoid endothelium, which is characterized by open pores and large intercellular clefts (**Figure 5B**).[33,150,160,180] On the other hand, NPs greater than ~100-200 nm have the tendency to be cleared in the liver and spleen. This clearance is assumed to be due to both the organ specific anatomy and the aforementioned size-related surface curvature properties.[117,181]

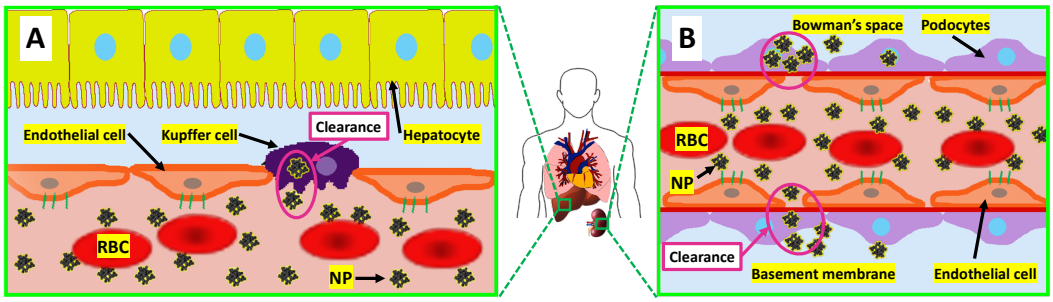

Figure 5. The effect of size on ligand-based NP clearance.
(A) An example of NP clearance from bloodstream by liver macrophages (Kupffer cells).[182] (B) Smaller NPs (< 5 to 10 nm) can clear from the bloodstream via the kidneys and accumulate in the bladder.[183] Lymphatic circulation in the lymph nodes, spleen, skin, and other organs is another major mechanism of clearance. Note: RBC in the schematic refers to red blood cell.

2.1.5. Dose of Ligand-targeted Nanoparticles

The dose of targeted NPs is one of the most studied properties as it modulates the drug concentration in the body and organs and hence can modulate the balance between therapeutic efficacy and safety.[1,14] Drug delivery via NPs have been shown to be particularly advantageous compared to its free drug counterparts due to the reduced side effects and lower dose needed to achieve the same therapeutic responses.[1,30,61,83,184] The dose of NPs can be expressed in relation to the total NP: number, mass, volume, surface, units of therapeutic activity, etc. all in relation to the mass of a treated subject.

Moreover, the dose of NPs has been shown to also modulate the circulation in the bloodstream and biodistribution to target vs. clearance organs.[95] This is because the concentration modulates the rate of NPs binding in the blood and organs, where various binding interactions (e.g., in the blood, target, and clearance organs) may be affected differently.[141,169] In addition, the NP concentration modulates the total surface interacting with the biological environment in the body as well as the number of targeting ligands available for binding,[185] which may saturate the endothelial surface and targeted molecules at certain NP concentration.

2.2. Bio-Physicochemical Properties and Drug Delivery Functions of Targeted DNA-based Nanoparticles

2.2.1. Properties of DNA That Enable Its Use in Drug Delivery

Nucleic acids possess many of the inherent and built-in bio-physicochemical properties highly sought after in nanomedicine, giving rise to various new classes of DNA-based NPs (DNA-NPs) for enhanced drug delivery.[19,20,186,187] The most unique properties of DNA arise from its precise self-assembly, based on DNA sequence complementarity and the resulting DNA helical twist.[188] These two phenomena allow for the uniform and reproducible manufacturing of DNA-NPs of nearly any geometry, architecture, and size down to a single atom definition (**Figure 6**). This in turn translates into precise control over some of their bio-physicochemical properties, including a very precise spatial organization and orchestrated composition of many other materials of interest, including targeting ligands, drugs, imaging agents, cells, ions, etc., giving rise to formulations with unique, precise, and versatile functional combinations (**Figure 6**).[19] As such, nucleic acids hold promise as a material for precision engineering at the nanoscale, thereby showing control and precision over the presentation of their targeting ligands, which may lead to improved targeting.

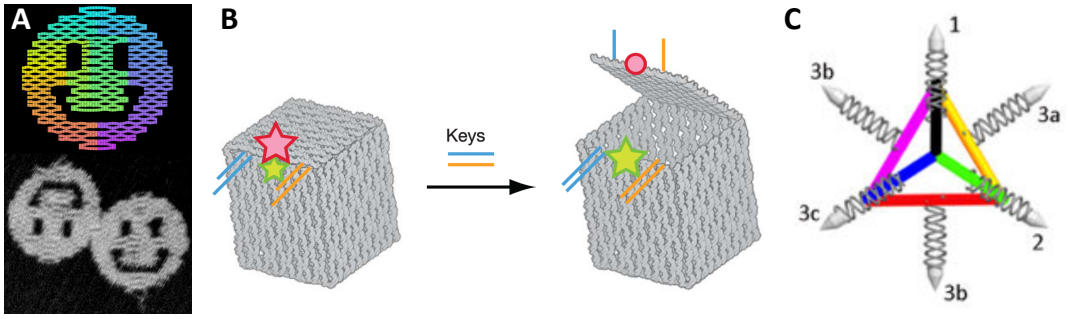

Figure 6. The precise, programable and versatile drug delivery functions of DNA-based NPs.

(A-C) Examples of the precise, versatile, and programable architecture of DNA-NPs.[74,75,189] (A) 100 nm DNA origami disk with three holes and a resolution of 6 nm.[74] (B) Controlled opening of a nanocontainer that is of 42 × 36 × 36 nm^3 dimensions for programmed cargo release.[189] (C) Specific combination and positioning of targeting ligands that are siRNA conjugated to allow for ligand hybridization with DNA-NPs and precise targeted delivery functions.[75] Folic acid (FA) is represented as bullet shapes and organized in set A: FA on positions 1, 2, and 3a; set B: FA on positions 1, 2, and 3b; set C: FA on positions 1, 2, and 3c).[75] Adapted with permission.[f]

---

[f] Panel (A) is adapted by permission from Springer Nature: Springer Nature, Nature, Rothemund PW, Folding DNA to create nanoscale shapes and patterns, 440(7082): 297-302; © 2006. Panel (B) is adapted by permission from Springer Nature: Springer Nature, Nature, Andersen ES, Dong M, Nielsen MM, Jahn K, Subramani R, Mamdouh W, Golas MM, Sander B, Stark H, Oliveira CL, Pedersen JS. Self-assembly of a nanoscale DNA box with a controllable lid, 459(7243):73-76; © 2009. Panel (C) is adapted by permission from Springer Nature: Springer Nature, Nature Nanotechnology, Lee H, Lytton-Jean AK, Chen Y, Love KT, Park AI, Karagiannis ED, Sehgal A, Querbes W, Zurenko CS, Jayaraman M, Peng CG. Molecularly self-assembled nucleic acid nanoparticles for targeted in vivo siRNA delivery, 7(6):389-393; © 2012.

Both, biological (recombinant) and synthetic techniques, as well as their combinations can be employed for robust, cheap, and scalable DNA-NP manufacturing. Nevertheless, each technique has distinct advantages and disadvantages, pertaining to the purity, size, and sequence of DNA strands, the complexity of the design, the yield and purity of the final product, etc. Furthermore, DNA can be efficiently functionalized with molecules of interest via various mechanisms.[19] Hybridization with oligonucleotide conjugated molecules (e.g., Ab-oligos) and intercalation with anthracyclines (e.g., doxorubicin) and similar molecules are unique to DNA and RNA (i.e. nucleic acids), while direct chemical conjugation, entrapment, etc. can readily be employed like for many other materials that are used to build NPs.[19,61,69,81,84,91,142,190–193]

In addition to their high precision and versatility over their geometry and functionalization, many other DNA-NP properties are highly tunable through various bio-physicochemical means (e.g., sequence, architecture, size, chemistry), including their flexibility, biocompatibility, and bioactivity. Precise control over their bio-physicochemical properties is particularly useful for tuning their degradation rate against DNA degrading enzymes (i.e., DNases) present in the body, therefore permitting suitable timeframes for therapeutic interventions.[47,83,194,195]

Furthermore, DNA-NPs can be designed to respond to various environmental cues (e.g., temperature, pH, ionic strength, etc.).[19,73,81,87,139,196–201] For example, DNA cages can open and close in response to changes in physiological stimuli, to allow for

the controlled release of therapeutics,[57,202–204] while hedgehog-like and branched DNA-NPs such as "spherical nucleic acids" and Ab-targeted 3DNA® can mediate cytosolic drug delivery without the help of additional agents.[58,190] In contrast, some DNA-made tetrahedrons and rods have not been shown to mediate such delivery, and instead primarily localize to the endolysosomal system.[58,190,205] However, the exact reasons for the differences in their behavior are still unknown. Some DNA-based designs are even capable of pore formation and insertion in cell membranes.[206] Hence, DNA constructs, once delivered to the organs and cells of interest, may be useful for the delivery of drugs to various organelles[205] as well as the cytosol.[58,92]

2.2.2. Ligand-based Targeting of DNA Nanoparticles

Ligand-targeted DNA-NPs hold great potential for drug delivery due to the precise control over their targeting properties, namely their targeting ligand presentation and geometry. The compatibility of DNA-NPs with ligand specific targeting mechanisms and exploration of their design parameters may help localize DNA-NPs to specific markers found at the sites of disease and/or at other sites of interest within the body. This can enhance the drug delivery functionality of DNA-NPs in a site-specific manner, resulting in improved therapeutic outcomes. Various other DNA-NP functionalities may be enhanced in this manner, spanning cell transport, sensing, imaging, physiologically responsive functions, and many other nanotools associated with DNA-NP targeting.

Early work indicated that nucleic acids can achieve drug delivery via receptor targeting when reformulated into aptamers, which are DNA- and RNA- made targeting ligands.[81] The development of more amenable and complex DNA-NPs followed, with functional parameters mostly focusing on tumor targeting applications where the primary mechanism of targeting is size-based (i.e. enhanced permeability and retention, EPR in the tumor), not ligand-based.[18,75,81,90,134,207–210] Furthermore, most of the DNA-NP designs tested so far do not utilize ligand-based targeting, as this is still an emerging concept in DNA nanotechnology; *de facto*, many DNA-NP designs simply rely on targeting scavenger and/or TLR9 receptors (mostly located intracellularly) to allow for cell binding and uptake, while lacking the ability for site-specific accumulation.

Despite the novelty, specific targeting properties of ligand-based DNA-NPs *in vitro,* using affinity ligands such as Abs, aptamers, vitamins, etc., has been shown to enable preferential interaction with cells that express the selected receptors or disease markers. For instance, HER2, nucleolin, biotin receptor, folic acid receptor, transferrin receptor, mucin 1, and several endothelial cell adhesion molecules are examples of markers to which DNA-NPs have been targeted.[27,58,82,83,90,209,211–213] As for the other properties, various DNA-NP configurations (spherical, dendrimeric, triangles, tubes, etc.) and sizes (commonly ~2-60 nm) have been explored.[19,58,71,75,82,83,90,196,209,211,214] Furthermore, DNA-NPs have shown to have good potential for therapeutic interventions such as the delivery of intercalating drugs, nucleic acid- and protein-based therapeutics.[19,58,75,190,215] As seen from these examples, the majority of DNA-NP

designs have been investigated for applications in cancer, but inflammation, immunomodulation, and vaccination are gaining more interest with the advancement of the DNA nanotechnology field.[58,61,87,216]

Nevertheless, biodistribution and interactions associated with specific targeting, particularly *in vivo*, and which design properties can be tuned to modulate said interactions, still remains fairly uncharacterized for DNA-NPs. Moreover, the specificity of their ligand-based targeting has not yet been carefully explored *in vivo* and quantitative biodistribution measurements are still scarce.[19,72] In addition, targeting functionalities designed *in vitro* most often do not translate *in vivo* for clinically relevant formulations. This is mostly due to the limited knowledge associated with the complex and unpredictable performance of the NPs *in vivo* and further due to the novelty and early stages of the field. Hence, determining the biodistribution for each targeted NP is of paramount importance.

As explained in earlier Background sections, many other design properties of NPs, in addition to selecting the biological targets, are well known to modulate their interactions with the biological environment and particularly their targeting. These properties, namely the size,[31,68] concentration,[82,95,210] and surface topography relating to the valency and density of surface targeting ligands,[75,217,218] may also similarly affect the targeting of DNA-NPs.

Although very few studies have systematically examined the influence of these factors for DNA-NPs, the published results illustrate their relevance. The concentration

dependence of targeting and/or cargo activity has been shown for tetrahedral and nanotube DNA-NPs targeted via folate, where the former case was tested *in vivo* in a mouse model and the latter case was tested in cancer cells *in vitro*.[75,82,217] Furthermore, the role of the targeting valency of DNA-NPs has been examined using similar formulations targeted via the folate or nucleolin.[75,217,218] The positioning of targeting moieties on DNA-NPs further impacted cell uptake[218] and intracellular activity of the cargo (siRNA).[75] However, most of the studies that measured the influence of these properties on the targeted delivery of either the NP or cargo, were conducted in cellular models and the data on biodistribution *in vivo* is very scarce. Namely, most *in vivo* studies measured the therapeutic activity of the cargo (siRNA) which not only depends on the organ delivery *per se*, but rather depends on additional functions (e.g., protection from degradation, transport to cytosol, release, etc.).

Overall, being able to deliver NPs (e.g., ligand-based DNA-NPs), which have been shown to be promising for intracellular drug delivery, in an organ- and tissue-specific way, holds great significance. Moreover, this can improve the efficacy and safety profile of drugs, especially the ones that are hard to introduce into organs and tissues specifically (e.g., biotherapeutics) or that are highly toxic (e.g., chemotherapy drugs).

2.2.3. Potential Challenges for Ligand-based Targeting of DNA Nanoparticles

As with most other NPs, DNA-NPs may be eliminated rapidly from the body. This can hinder targeted drug delivery, particularly for the designs that require prolonged circulation in order to reach their targets. Being a material of biological origin, the body has natural clearance mechanisms in place for DNA structures; including enzymatic degradation in the blood and organs; immunorecognition, mostly in the blood, liver, spleen, and lymphatic system; and kidney filtration, and excretion. Fast excretion to the bladder has been shown for many early DNA-NP designs, most likely due to the premature degradation and immunorecognition via scavenger receptors which are involved in the clearance of foreign materials and waste products.

As mentioned, like many other NPs,[157,219] DNA-NPs can be actively taken up by scavenger receptors either directly or through opsonization.[220] However, much is still unknown about this controversial topic due to the versatility of DNA sequences and DNA forms that are found in nature or synthetically designed for research and therapeutic applications. For example, while some *in vitro* experiments demonstrated the association between increased serum protein adsorption on DNA-NPs and increased cell uptake in cell culture,[28] it was later found out that serum proteins can also reduce DNA-NP uptake.[220] Hence, the results depend on the given conditions of both the DNA-NP design and the biological environment, favoring uptake either through opsonic or non-opsonic clearance receptors.[221]

In addition to the direct binding to non-opsonic scavenger receptors (SR), specifically MARCO SR from class A, which is expressed on macrophages (e.g., Kupffer cells in the liver) and high endothelial venules,[222] DNA clearance can be associated with specific DNA forms; e.g., unmethylated CpG DNA motifs that bind to TLR9 receptors, mostly intracellularly.[223] Nevertheless, this latter process is predominantly present and used for the recognition of pathogenic DNA or endogenous DNA originating from the mitochondria, but not the nucleus. Hence, CpG functionalities can be either eliminated or exploited, depending on the requirements and intended application of DNA-NP design.[224,225] Altogether, these are some of the clearance receptors and interactions that need to be overcome in order to achieve targeting to specific molecules of interest.

While some natural DNA forms clear the blood within minutes, other DNA forms have been found to circulate for hours, delaying the scavenger clearance or degradation. This is the case with fetal DNA clearance from maternal blood which has a biphasic clearance profile (half-lives of ~10-60 min and ~13 h).[226] This example represents the case where bio-physicochemical properties of DNA-NPs could be potentially selected to avoid uptake by scavenger receptors. Indeed, much progress and improvement has been made in understanding how the DNA-NP sequence, chemistry, architecture, and combination with other materials modulate their degradation and immunorecognition. These advancements can provide conditions for more optimal

targeting of ligand-based DNA-NPs *in vivo*, allowing for the exploration of various targets and DNA-NP properties.

2.2.4. Properties of 3DNA® Nanocarriers

As mentioned in the Motivation and Goals section, 3DNA® (3DNA), designed by Genisphere® LLC is a highly branched DNA-made NC of dendrimeric architecture.[89] It represents a good model to study ligand-based targeting of DNA-NPs due to its precise and modular parameters of many bio-physicochemical properties, particularly pertaining to the topography and density of ligand functionalization, as well as size. Moreover, 3DNA holds considerable practical promise.[58,89–93]

3DNA manufacturing via synthetic hybridization technology is robust and allows for the easy implementation of non-immunological nucleotide sequences.[89,227,228] It allows for scalability and reproducibility, as well as stable and uniform NCs which are some of the key requirements for successful clinical applications in nanomedicine.[89,229–231] Briefly, 3DNA is assembled from seven unique single-stranded DNA sequences that can hybridize to form a double stranded complementary waist in the middle region, while leaving the terminal ends, the arms, unhybridized (i.e. single stranded) due to the lack of complementarity.[90–92,232] The resulting structure, referred to as a DNA monomer, is then photo-crosslinked using psoralen.[232,233] This monomer is further hybridized to one of the other four unique DNA monomers, utilizing their sequence-specific complementary free arms to create the first

layer (generation) of monomers around the core monomer (i.e. 1L 3DNA). The repetition of this hybridization process with interchangeable monomers and crosslinking leads to subsequent layers (**Figure 7**).[90–92,232] Crosslinking parameters, DNA modification with phosphorothioate[g], and functionalizing 3DNA with Abs and/or other materials can be used to control DNA resistance to enzymatic (DNase) degradation.[229]

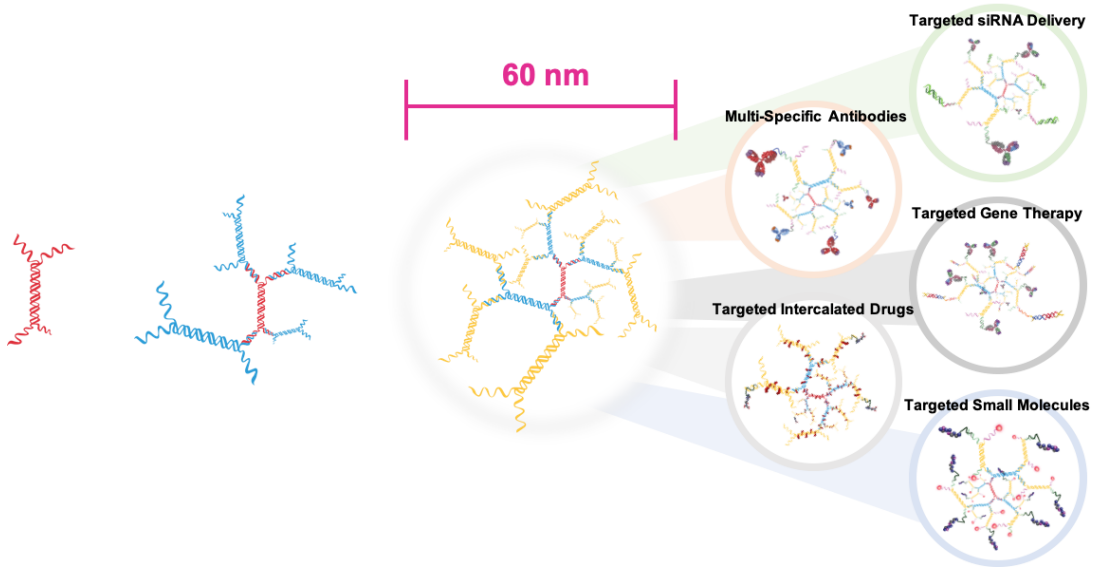

Figure 7. 3DNA assembly and functionalization.
DNA monomer shown on the left (red color) is hybridized to subsequent monomers to form 1L (red + blue color), and 2L (red + blue + yellow color) 3DNA.[89] Functionalization of 3DNA via hybridization and direct chemical conjugation on the right.[h]

---

[g] Modification with phosphorothioate involves replacing non-bridging phosphate oxygen with sulfur.

[h] Modified with permission from Genisphere® LLC.

The size of 3DNA, as well as the number and spatial distribution of functional arms located on the 3DNA periphery, can be controlled through the aforementioned step-wise, layer-by-layer self-assembly of smaller DNA monomer subunits (**Figure 7**).[90,91,232] As an example, 2-layer (2L) 3DNA has 36 arms and a diameter of ~60 nm (1242 kDa DNA mass), and 4-layer (4L) 3DNA has 324 arms and a diameter of ~170 nm (11228 kDa DNA mass). Additionally, both 2L and 4L 3DNA have a ζ-potential of around -30 mV. Single, various, or all 3DNA terminal arms can be functionalized with therapeutic, targeting, and/or imaging agents. These agents can be incorporated via chemical modification, nucleic acid hybridization, or intercalation.[233] For example, Abs can be hybridized to 3DNA arms after their conjugation to single-stranded complementary oligonucleotides; for this, NHS and maleimide chemistry can be used in order to achieve heterobifunctional crosslinking between oligonucleotide sulfhydryls with Ab amines.[229] The quantity and combination of hybridized agents can be controlled by using unique sequences of 3DNA terminal arms and the molar ratio of agents to 3DNA. Specific targeting parameters and combination therapies can be designed on the site in this manner, providing an opportunity to finely tune 3DNA for particular applications. As an example, this can allow for the precise control over their targeting valency, dual receptor targeting, tuning the ratio between surface moieties that provide targeting vs. stealth properties, or combining several drugs into one targeted 3DNA platform.[89–92,232]

2.2.5. Ligand-based Targeting of 3DNA Nanocarriers

3DNA was originally used as a biomolecular detection and signal amplification technology,[233] but the Muro lab established the utilization of 3DNA for ligand-based targeting and drug delivery applications using cell culture studies. [58,234,235] After establishing the use of 3DNA technology for specific targeting and intracellular functional delivery, several studies have validated ligand-based 3DNA formulations for targeted drug delivery applications.[58,89] So far, 3DNA has been tested for the delivery of toxins, proteins, and genetic material[58,90–92] in diverse cell types (endothelial, epithelial, mesothelial, fibroblasts, etc.)[58,90–92] and utilized several cell-surface receptors, such as ICAM-1, platelet-endothelial cell adhesion molecule 1 (PECAM-1), transferrin receptor, mannose-6-phosphate receptor, folate receptor, etc.[58,90–92]

Also, 3DNA has advanced from *in vitro* cell culture to *ex vivo* and *in vivo* studies with promising results.[19,90–92] Examples of 3DNA targeted drug delivery under investigation involves using a unique monoclonal Ab to specifically deliver doxorubicin and deplete problematic cells in an ophthalmic application *ex vivo,*[91] and the qualitative biodistribution study of folate targeting to an ovarian tumor model *in vivo,* using the I.V. administration route.[90] In the latter, fluorescently labeled 3DNA was visualized in histological tissue sections 24 h post-administration in several organs,

indicating tumor specific targeting.[90] This study also demonstrated the therapeutic effects of 3DNA-mediated anti-HuR siRNA targeted delivery via folic acid *in vitro* and after intraperitoneal administration *in vivo*.[90] Another study tested the functional effects of plasmid delivery via 3DNA targeting to the transferrin receptor, utilizing the I.V. route. The plasmid encoding diphtheria toxin was delivered to pancreatic cancer cells that overexpress the promoter necessary for the expression of the delivered gene.[92]

From these studies exploring the 3DNA platform, one can deduce that this design holds promise for targeted drug delivery, showing encouraging therapeutic effects. However, the full potential of 3DNA's ligand-based targeting ability and biodistribution to organs is still unknown due to the several reasons: 1) the lack of quantitative measurements[236] of 3DNA biodistribution *in vivo*; 2) the utilization of tumor models may confound the accurate assessment of 3DNA's ligand-based targeting to specific biological markers due to the concomitant primary targeting mechanism via EPR effect;[19,58,89–92] and 3) the lack of systematic knowledge on how bio-physicochemical properties such as 3DNA targeting valency, targeting density, size, and dose further affect targeting and biodistribution. Likewise, the gap in knowledge as depicted above exists for DNA NPs in general.

2.3. ICAM-1-targeted Nanoparticles to the Pulmonary Vasculature

Alongside the ability of DNA-NPs to precisely control targeting parameters and potentially contribute to improved drug targeting *in vivo*, the vascular endothelium represents an important targeting strategy, as well as the means to expand the targeting applications of DNA-NPs.[7,58,107] Not only does the vascular endothelium provide markers for enhanced site-specific drug delivery to the organs with high vascular density (e.g., lungs), but it is a major participant in inflammation and therefore the therapeutic target itself.[7]

Each of the several markers available for binding to the vascular endothelium imposes the amenable range and specific set of requirements for achieving the optimal targeted drug delivery, which is application specific.[7,107] Targeting ICAM-1 is a particularly attractive strategy for site-specific delivery of drug NPs and supports good flexibility for the modulation of targeting parameters.[7,107] As mentioned, this encompasses a selection of targeting ligands (peptides, Abs, etc.) and other NP materials (PLGA, polystyrene, etc.), the density and valency of targeting ligands, NP size, NP shape, etc. as shown by our group and others.[7,107] The specificity and flexibility of targeting draws from the nature of ICAM-1.[170]

ICAM-1 is a glycoprotein that is constitutively expressed on the surface of the endothelial cells and other cells in the body.[7,107] The ICAM-1 extracellular domain

extends into the lumen of the cardiovascular system, making it accessible for various-size NPs from the bloodstream.[7,44] The biodistribution of multivalent and high affinity NPs targeted to ICAM-1 is characterized by their preferential accumulation in the lungs. Pulmonary vasculature is the most specific target for this receptor due to: the high content of endothelial cells and hence high content of ICAM-1 in the lungs, being the first pass capillary network after I.V. administration, and receiving full blood input from the heart.[168,237] Blood from the lungs is further redistributed to other organs; hence, examples of other target organs are the brain and heart.[7] Upregulation of ICAM-1 expression during inflammation can further enhance delivery to the lungs and/or to inflammation-specific sites.

Indeed, endothelial markers such as ICAM-1 have been explored in the field of targeted therapeutics for the safe treatment of many inflammation-related diseases,[10,150,238–241] spanning autoimmune diseases, cardiovascular diseases, various cancers, genetic diseases, and neurological diseases related to inflammation, among others.[7,38,45,49,100,129,130,149,150,237,238,240–243] Consequently, ICAM-1 targeted NPs could be particularly useful for the specific treatment of chronic obstructive pulmonary diseases (COPD) caused by lung inflammation, lung fibrosis, Niemann-Pick Disease type B associated lung diseases, as well as lung cancers and many others.[2,43,99,237,244]

Selecting ICAM-1's bio-physicochemical properties, including the upregulation of ICAM-1 overexpression, are a good choice to enhance drug delivery in many applications. However, these properties are modulated by pathology over which

there is little, if any, control. In contrast, select natural and synthetic nano- and micro-scopic objects of various compositions and targeting valencies represent examples of some of the primary bio-physicochemical properties that can be controlled in order to modulate ICAM-1 targeting.[7,44] For example, ICAM-1 is utilized for endothelial binding and adhesion of rolling leukocytes that are micrometers in size and bind multivalently to ICAM-1, as well as some pathogens (bacteria and viruses) which can, on the other hand, be both micro- and nano-scopic in size. Similarly, ICAM-1 targeted NPs of different composition, size, and valency can be used to modulate the delivery of therapeutics.[38,95,130,237,242]

More specifically, ICAM-1 targeted NPs (of spherical shape) utilizing a valency of ~250 Abs per NP show higher targeting avidity compared to the free Ab counterparts (~100-fold), and this further increases with increasing both the Ab density and size of the NPs (the tested Ab density range was 0 to ~7000 Ab molecules/μm^2 and the size range was 200-1000 nm).[10,95,130] Binding is strong enough to overcome the physiological level of shear stress.[170] Increasing the dose results in faster binding kinetics up to the saturation level.[95] *In vivo*, this translates into increased lung accumulation with increasing valency, size, and dose, while reducing accumulation in the clearance organs (e.g., liver and spleen).[95,98] However, the results for these parameters are not always predictable *in vivo* due to the complexity of the biological environment, and the complex and unique properties of each NP, particularly pertaining to their efficiency of binding under physiological conditions. For example, some NPs

may have inherently stronger non-specific binding interactions and the affinity for scavenger receptors, requiring higher targeting valency to increase the targeting power.

Another valuable property of ICAM-1 targeted NPs is their efficient and modular uptake through vesicular cellular internalization, and further transport within or across the cells.[55,56,163,245,246] Accordingly, ICAM-1 targeting provides the opportunity for NPs to access various cellular compartments and underlying tissues. As such, targeting ICAM-1 can not only expand therapeutic applications for DNA-NPs, but also help demonstrate that NPs with cytosolic delivery potential, such as demonstrated for some DNA-NPs,[58,82,215] can indeed be I.V. delivered *in vivo* via specific receptors associated with NP internalization processes and in the absence of EPR effect.

The NP parameters can influence the rate of uptake, trafficking, and the trafficked location,[163] influencing the exposure time of NPs to the blood, cellular, and extracellular compartments. This can potentially affect metabolism, degradation, and organ biodistribution. To accommodate the uptake of larger NPs via ICAM-1, NP-bound ICAM-1 sites are acidified by the cell in an enzyme-dependent manner in order to modify the composition of the membrane by enrichment in ceramide.[154,247,248] This results in enhanced membrane deformability and cytoskeletal organization,[248] which may affect the subsequent binding and organ targeting of NPs. The rate of uptake is an important feature for biodistribution as it will also influence the receptor recycling time and their recovery on the surface for further NP binding to organs.[249]

All of the aforementioned attractive bio-physicochemical properties have made ICAM-1 targeting a major focus of research in our lab, i.e.: 1) amenable accessibility, 2) great lung targeting potential, 3) broad range of NP parameters that are supported, 4) relevance of ICAM-1 in inflammation as a fundamental process in many pathologies, and 5) the ability to intracellularly access various compartments and other cell types beyond the endothelium.[7,98,150,238,240,241,250] Overall, these properties allow for NP designs with fast targeting, which may in turn minimize the exposure of biotherapeutic NPs to components of the circulatory system often associated with premature drug degradation, release, and immunogenicity.[10,29,65,70,95] ICAM-1 targeted NPs have therefore been experimentally explored for effective and safe delivery of various therapeutic and diagnostic agents with precise intracellular delivery.[7,96,107,150]

2.4. ICAM-1-Targeted Prototype 3DNA

Early work in the Muro lab explored for the first-time various Abs-3DNA-made NCs for targeted drug delivery applications, with a primary focus on endothelial targeting.[58] These basic prototype designs consisted of 20 secondary Ab-oligonucleotide conjugates hybridized to a 4L 3DNA scaffold to allow for the immunoconjugation with anti-ICAM or other specific Abs, resulting in ~200 nm NCs (**Figure 8**).[58] A particularly promising Ab/3DNA formulation for endothelial targeting, a prototype anti-ICAM/3DNA, demonstrated one of the highest targeting and target specificities to endothelial cells *in vitro*, and about the highest specificity reported for

a DNA-based NP (~190-fold increased specificity over 3DNA coupled to non-specific Abs).[58]

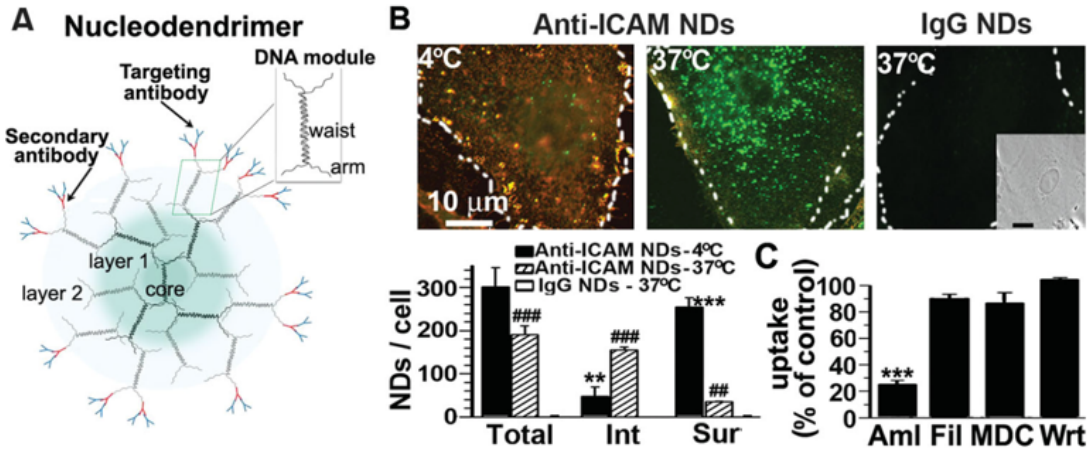

Figure 8. The prototype anti-ICAM/3DNA design and high efficiency of specific binding to cells.

(A) The prototype 3DNA (shown as nucleodendrimer, ND) containing secondary Ab is immuno-bound to targeting Ab.[58] (B) Specific binding and active cell uptake of anti-ICAM/3DNA compared to non-specific IgG/3DNA control in endothelial cells (upper panels, showing anti-ICAM staining for surface anti-ICAM/3DNA in orange and internalized anti-ICAM/3DNA in green color; bottom shows quantitative binding and uptake).[58] (C) uptake inhibition by endocytosis inhibitors.[58] Reprinted with permission.[i]

It was also shown that substituting the core material of previously tested anti-ICAM/NPs (i.e. made out of polystyrene and PLGA solid spherical core) with 3DNA-made core did not change the specificity or absolute delivery in endothelial cells.[58] This

[i] Reprinted from Advanced Functional Materials, 24, Muro S, A DNA device that mediates selective endosomal escape and intracellular delivery of drugs and biologicals, 2899-906, 2014, with permission from John Wiley and Sons.

was the first time that Abs linked to DNA-NPs larger than ~80 nm were shown capable of cell entry via the ICAM-1 specific endocytic pathway, and it was also the first formulation larger than ~30 nm to show receptor specific binding and uptake *in vitro*. Targeting of 3DNA-linked Abs was confirmed in various other cell types, specifically endothelial, epithelial, mesothelioma, and fibroblastic cells; as well as to various other receptors, specifically PECAM-1, transferrin receptor, or mannose-6-phosphate, to help demonstrate its potential for many applications.[58] In light of this, the prototype anti-ICAM/3DNA formulation showed promising targeting abilities *in vivo* upon I.V. injection in mice.[110] However, the targeting was modest compared to that of well-characterized model polystyrene NPs targeted to ICAM-1.[237,238,241]

At the subcellular level, Ab-targeted 3DNA not only demonstrated cell-specific endo-lysosomal and cytosolic delivery in a safe manner, but also expanded the potential of DNA-NP's cytosolic delivery of several representative types of therapeutic molecules. These include small toxins (phalloidin), polysaccharides (dextran), plasmid DNA (encoding EGFP-RhoA), catalytic enzymes (catalase), and proteins (albumin).[58] In this case, protein (albumin) with a nuclear localization signal was used to allow its translocation to the nucleus upon cytosolic delivery, thereby demonstrating the possibility of delivering cargo to other intracellular locations.[58] Lastly, *in vitro* studies indicated that 3DNA endosomal escape activity may only be activated under the pH condition as found in the endo-lysosomal system (pH of ~6.5 to 4.5).[58] However, whether ligand-specific targeting and consequent cell specific intracellular delivery can

be achieved *in vivo* was still unknown. As mentioned in the Motivation and Goals section, this dissertation explores the ligand-specific targeting of new anti-ICAM/3DNA formulations at the organ level *in vivo*.

Chapter 3: Significance and Innovation

3.1. Significance

This dissertation explores a method to improve quantitative radiotracing-based measurements and analysis of the *in vivo* biodistribution of anti-ICAM/3DNA. Importantly, it provides knowledge on pulmonary targetability and overall biodistribution of anti-ICAM/3DNA NCs, which are administered via the I.V. route *in vivo*. Moreover, it deciphers the role and parametric modulation of the design properties relevant to DNA-NP targeting, precisely: the role of ligand specificity, targeting ligand density and valency, size, and concentration. In addition, this dissertation reveals the predicted effect of design properties on cargo delivery via two distinct carriage modes, DNA base intercalation of the cargo and arm coupling of the cargo. The findings will help inform drug delivery design strategies utilizing ligand-based NPs, particularly in the DNA nanotechnology field and for applications relying on endothelial targeting, which includes the lungs and is relevant in many therapeutic interventions.

As explained in the Background section and demonstrated by several approved formulations in clinical use, NP-based drug delivery systems hold promise in improving patient treatment due to their unique bio-physicochemical properties. Nevertheless, site-specific delivery remains inefficient, hindering their full therapeutic potential and reducing safety.[26,46,58,143] Although ligand-based targeting functions of

NPs have been shown to enhance site-specific delivery via certain biological markers,[10,107] there are currently no approved ligand-based nanomedicines other than ADCs. Hence, the exploration of new targeting strategies, such as the utilization of anti-ICAM/3DNA, is significant as it will inform the design of more efficient and safer NP-based therapies, as well as help advance the field of targeted nanomedicines towards clinical translation.

As explained in the Background section, ligand-based DNA-NPs have many attractive and precise bio-physicochemical properties that are relevant in the targeted drug delivery field.[13–18,22–27] A good example is the 3DNA targeted drug delivery platform, which has shown to have particularly promising tools for enhanced therapeutic efficacy *in vivo* across many research labs.[19,58,89–92] Despite demonstrating therapeutic potential, the quantitative biodistribution and specific targeting of ligand-based 3DNA and other DNA-NPs *in vivo* remain poorly characterized.[19,58,89–92] By investigating the biodistribution and specific targeting of anti-ICAM/3DNA *in vivo*, this study provides knowledge on 3DNA's specific targeting utility and behavior *in vivo*, which may be applicable to a diverse group of Ab-based 3DNA NCs and other targeting strategies in DNA nanotechnology. Additionally, this research may help advance DNA-NP's versatile functionalities towards clinical applications in targeted drug delivery, and towards the development of *in vivo* research and diagnostic tools.

As explained in the Background section, the vascular endothelium, and particularly ICAM-1, represent a promising strategy for enhancing the site-specific

delivery of NPs, particularly to the pulmonary vasculature and disease sites.[10,150,238–241] Nevertheless, there are currently no clinically approved formulations utilizing ICAM-1 targeting. Following the demonstration of anti-ICAM/3DNA NCs specific targeting to ICAM-1 in endothelial cell culture and *in vivo*,[58,110] this work is designed to provide the first studies presenting efficiency and specificity of anti-ICAM/3DNA targeting *in vivo*. As such, by demonstrating the efficient targetability of anti-ICAM/3DNA design to lungs via ICAM-1 *in vivo*, we provide data to help advance this platform towards effective therapy for pulmonary diseases (e.g., COPD, asthma, lung cancer, etc.), and translatable to many other biological markers that are accessible from the bloodstream and through various vascular administration routes.

Furthermore, given the dependence of therapeutic efficacy and safety on site-specific targeting of ligand-based NPs *in vivo*,[10] and given the relevance of multivalent binding of cells, pathogens, and various therapeutic NPs to ICAM-1,[96,163,240] as well as their size and concentration,[14,95,130,163] it is necessary to better understand how NP design parameters modulate site-specific targeting and drug delivery. Nevertheless, this remains underexplored for DNA-NPs, such as anti-ICAM/3DNA. By investigating the effects of anti-ICAM/3DNA's bio-physicochemical properties (i.e., ligand valency, ligand density, size, and dose) on anti-ICAM/3DNA specific targeting and drug delivery potential to the lungs, this thesis will help optimize the therapeutic delivery of the anti-ICAM/3DNA platform for pulmonary diseases, which may be translatable to other targets and DNA-NPs. Moreover, the findings may help advance knowledge on

the modulation of NP behavior and endothelial targeting parameters *in vivo*, which may be translatable to understanding biological systems, cells, and pathogens.

Overall, advancing our understanding of DNA-NP targeting functionality to specific biological markers *in vivo* will help **guide many unique, versatile, and novel DNA-NP designs towards more efficient and safer therapies**.

3.2. Innovation

Most DNA-NP systems are designed without targeting ligands and necessitate prolonged circulation in the bloodstream, or utilize the ligands for improved cell uptake after their passive accumulation via the EPR at the target sites.[33,75] In contrast, the active targeting strategy based on the anti-ICAM/3DNA design used in this study provides direct and fast lung targeting from the bloodstream and does not require passive targeting mechanisms such as EPR. Hence, the expansion of ligand-based DNA-NP functionalities to specific and efficient targeting to ICAM-1 is novel in the field of targeted DNA nanotechnology and represents a new sub-field in drug delivery.

Moreover, knowledge on DNA-NP targetability and biodistribution *in vivo* is still in its infancy and requires comprehensive quantitative exploration.[19,71,214] Additionally, since DNA-NPs are challenging to characterize due to their biodegradability,[71,205,214,251] the novel application of the radiotracing method was developed to ameliorate the effects of free tracer present in the administered formulations or generated due to the anti-ICAM/3DNA degradation. Hence, the robust,

quantitative, and systematic characterization of DNA-NP biodistribution and targetability *in vivo* is accomplished for the first time.

Furthermore, the utilization of a novel anti-ICAM/3DNA design[j] allowed for the increased efficiency of *in vivo* targeting compared to the modest targeting levels obtained with the prototype anti-ICAM/3DNA design, which in turn allowed for the utilization of much lower Ab density compared to previous anti-ICAM/NP-based systems, while still achieving comparable targeting.[110] In addition, the anti-ICAM-oligos designed by Genisphere® LLC and tested for the first time in this work as targeting ligands, showed improved targetability compared to non-oligo anti-ICAM Ab counterparts, which may be exploited for novel therapeutic delivery strategies in the future.

As mentioned in the Background section, several NP-based systems have been designed for site-specific delivery to the endothelium, and particularly to the lungs via ICAM-1.[240] Nevertheless, the anti-ICAM/3DNA represents the first-ever site-specific delivery of a DNA-based NP to ICAM-1 and, thus, indicates a novel therapeutic for the treatment of pulmonary diseases.[110]

---

[j] The novel anti-ICAM/3DNA design utilizes proprietary DNA sequences designed by Genisphere® LLC to reduce immunogenicity, as well as modified antibody functionalization methodology via direct 3DNA hybridization with anti-ICAM Ab-oligo conjugates.

While many promising ligand-based NPs currently in development lack uniform and precise bio-physicochemical properties,[10,32,37,49] DNA-NPs, such as anti-ICAM/3DNA, may be designed with precise organization and integration of targeting ligands and other molecules on a single NP, and with uniform and precise size and shape.[29] Moreover, endothelial targeting via ICAM-1 offers flexibility in the design of NPs as shown before.[10,240] As such, the use of the precise, uniform, and tunable anti-ICAM/3DNA design represents a novel approach for the precise control over the systematic exploration of ICAM-1 targeting parameters *in vivo*.

Chapter 4: Materials and Methods

4.1. Reagents

Rat monoclonal immunoglobulin G Ab (IgG) against mouse ICAM-1 (anti-ICAM) was clone YN1, produced in a respective hybridoma from the American Type Culture Collection (Manassas, VA). Non-specific rat IgG Ab (called IgG hereafter) was from Jackson Immunoresearch (Pike West Grove, PA). Polyclonal anti-PECAM-1, FITC-labeled secondary Ab and Alexa Fluor 488-labeled secondary Abs were from Novus Biologicals (Centennial, CO), Jackson Immunoresearch (West Grove, PA) and Thermo fisher Scientific (Waltham, MA), respectively. DNA oligonucleotide (72-mer) modified with thiol at 5′ was from Oligo Factory (Holliston, MA). Pierce Bond-Breaker TCEP Solution, Pierce LC-SMCC Crosslinker, Pierce Zeba Spin Columns (7 k molecular weight cut-off, MWCO), Pierce Thiophilic Adsorption Resin, Amicon spin filters (10 k MWCO), Pierce BCA Protein Assay Kit and Heterobifunctional Pierce Crosslinking Kit, bovine serum albumin (BSA), and TCA were from Fisher Scientific (Kerrville, TX). Carboxylic acid-terminated PLGA (50:50 copolymer ratio; 32 kDa average molecular weight) was from Sigma-Aldrich (Saint Louis, MO). Iodogen iodination tubes were from Pierce (Rockford, IL) and BioSpin Tris Columns from BioRad (Hercules, CA). $Na^{125}I$ was from Perkin-Elmer (Waltham, MA). All other reagents were from Sigma Chemical (St. Louis, MO).

4.2. Preparation of Nanoparticles

4.2.1. Antibody-oligonucleotide Conjugates

Antibody-oligonucleotide (Ab-oligo) conjugations for anti-ICAM or non-specific control IgG Abs were performed by Dr. Lou Casta at Genisphere® LLC using N-hydroxysuccinimide (NHS)-maleimide chemistry and donated for their use in this project. In brief, 72-mer DNA oligo with a 5'thiol modification was first reduced by adding 50 mM tris(2-carboxyethyl)phosphine (TCEP) and incubating at 25 °C for 1 h. Excess TCEP was removed by ethanol precipitation and the oligo resuspended in phosphate buffer saline (PBS) + 5 mM (ethylenediaminetetraacetic acid) EDTA, pH 7.2.[110] In parallel, Ab was reacted with LC-SMCC crosslinker (succinimidyl 4-(N-maleimidomethyl)cyclohexane-1-carboxy-(6-amidocaproate)) in excess at 25 °C for 1 h. Zeba spin columns, equilibrated in PBS + 5 mM EDTA pH 7.2, were used to remove unreacted LC-SMCC crosslinker from the Ab-LC-SMCC reaction as per vendor's instructions.[110] Reduced oligo was then added to the Ab-LC-SMCC and the conjugation reaction was allowed to incubate at 25 °C for 12 h.[110] Thiophilic adsorption chromatography was utilized to remove excess unreacted thiol oligo from the Ab-oligo conjugate and fractions containing the conjugate were pooled and concentrated using Amicon 10 kDa MWCO spin filters.[110] The final protein concentration of the Ab-oligo conjugate was determined using a (bicinchoninic acid) BCA Protein Assay kit with bovine gamma globulin standards.[110]

4.2.2. 3DNA®

Genisphere® LLC synthesized the 3DNA structures (4L and 2L) by following published protocols, determined their concentration using a spectrophotometer, and donated the 3DNA to the laboratory for their use in this project (**Figure 9**).[91,232,233] Briefly, seven unique single-stranded DNA oligonucleotides were hybridized by complementarity into five different "monomer" structures, each with a central double-stranded region and four single-stranded ends.[110,232,233] These monomers were then hybridized to one another, layer-by-layer, with psoralen crosslinking at each step to make covalent bonds in specified nucleic acid regions.[110,232,233] The resulting tridimensional scaffold of double-stranded DNA contained peripheral single-stranded DNA "arms" for hybridization with other molecules (e.g., Ab) conjugated to short DNA oligonucleotides.[91,110] The final size and number of peripheral arms available for subsequent hybridization depends upon the number of layers assembled.[110,232,233] These studies utilized 4L 3DNA with 324 peripheral arms and 2L 3DNA with 36 peripheral arms with average MW of 10,000 kDa and 1,000 kDa respectively.

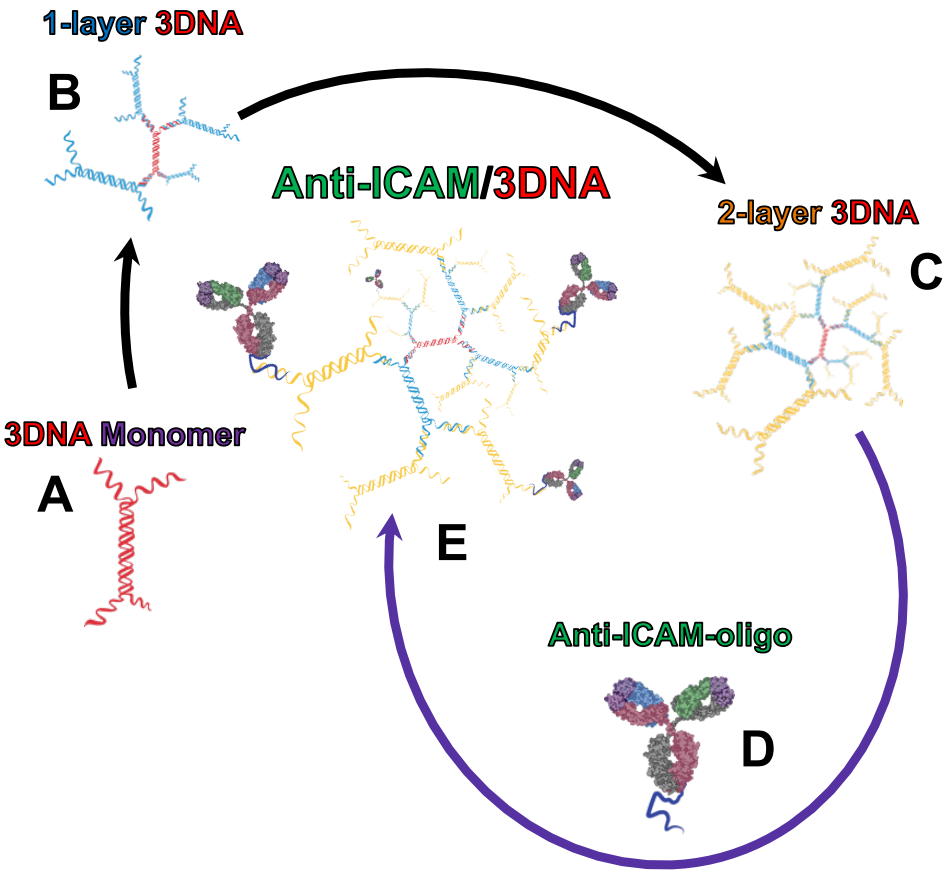

Figure 9. Size and targeting valency modulation of anti-ICAM/3DNA NCs through layer-by-layer assembly.

(A) DNA monomer is hybridized to subsequent monomers to form (B) 1L, (C) 2L, and up to 4L 3DNA (not shown). (D) Anti-ICAM Ab-oligo conjugate is hybridized in a specific molar ratio with 3DNA whose outer arms are complementary to an Ab-oligo sequence, (E) resulting in anti-ICAM/3DNA of a particular size and valency.

4.2.3. PLGA Nanoparticles

PLGA NPs of spherical shape (PLGA NPs) were prepared using a surfactant free nanoprecipitation/solvent evaporation method, as described.[110,238] Briefly, PLGA

was dissolved in acetone at 20 mg/mL and poured under moderate stirring into the nanopure water (dispersing phase) at the final volume of 90 mL and concentration of 2.22 mg/mL, and at room temperature (RT). The NPs formed instantaneously, and the dispersion was kept under mild stirring to allow acetone evaporation overnight. A rotary evaporator was used to concentrate the PLGA NPs for their further use in experiments. The NPs were then freeze-dried to determine the weight of the polymer. Subsequently, the NP concentration was estimated by dynamic light scattering (DLS; Malvern Zetasizer, Worcestershire, UK) in comparison to similar-size standards and from the weight of PLGA polymer of a given NP volume measured after freeze-drying.

4.2.4. Radiolabeling of Antibodies and Antibody-oligonucleotide Conjugates

Abs (non-oligo) or Ab-oligo conjugates were ^{125}I-radiolabeled using Na^{125}I and iodogen coated iodination tubes. 20 μCi of Na^{125}I was incubated at 4 °C for 5 min in iodination tubes containing 100 μL of 1 μg/μL Ab in PBS. Samples were then subjected to size exclusion chromatography in 6 kDa cutoff Tris columns and centrifuged at 1000 × g for 4 min to eliminate non-reacted free ^{125}I. The final concentrations of the resulting ^{125}I-Abs or ^{125}I-Ab-oligo conjugates were measured using Bradford protein assay and BSA standard curve. The radioactivity (counts of detected radioactive events per min, CPM) of the samples, expressed as CPM per μg protein, and the presence of free ^{125}I remnants were then measured in a γ-counter (2470 Wizard^{2TM}, Perkin Elmer, Waltham, MA). For this, 2 μL of ^{125}I-Ab or ^{125}I-Ab-oligo were diluted in 3% BSA in PBS,

resulting in 1 mL total volume and then measured in a γ-counter. Next, 200 µL TCA was added (final TCA concentration = 17%, v/v), the sample was vortexed and incubated for 15 min at room temperature. Then, the sample was centrifuged at 2418 × g for 5 min to precipitate ^{125}I-Ab-oligo and separate free ^{125}I in the supernatant. A 600 µL aliquot (half the total reaction volume) of the supernatant was then measured in a γ-counter, to estimate the presence of free ^{125}I in the samples to be injected in mice using the following equation:

$$Free\ Iodine\ CPM = Total\ CPM - (2 \times\ supernatant\ CPM).$$

4.2.5. Radiolabeling of 3DNA®

The radiolabeling procedure for 3DNA was similar to the radiolabeling of Abs explained above, with the exception that the removal of free ^{125}I via filtration was not performed here. The 3DNA concentration was assumed to stay the same before and after iodination.

4.2.6. Antibody Coupled 3DNA®

^{125}I-Ab-oligo or non-radiolabeled Ab-oligo, where indicated, were coupled to the outer layer of 3DNA. For this, the precise Ab surface densities were pursued by hybridizing 3DNA with Ab-oligo in the desired molar ratios (e.g., 16.9 µM conjugate, as oligo, to 89 µM 4L 3DNA), then incubated at 37 °C for 30 min to allow hybridization (Tm of ~72°C) of the DNA sequence of ^{125}I-Ab-oligo to complementary outer single-

stranded DNA sequences of 3DNA. Non-specific IgG/3DNA formulations were used as non-specific controls (targeting valency = 0). Additional formulations tested in this work include Ab coupled 3DNA where 3DNA had been similarly coupled to fluorescent Cy3[k] for visualization by fluorescence microscopy.

4.2.7. Antibody Coupled PLGA Nanoparticles

PLGA NPs were coupled with respective Abs via surface adsorption.[237] This was done at the molar ratios to achieve ~90 anti-ICAM Abs per PLGA NP to allow comparison with ~90 valency 3DNA counterparts. Non-specific IgG/PLGA formulations were used as non-specific controls (targeting valency = 0) and were fully coated with the IgG Ab as previously reported.[238] Briefly, ~$3x10^9$ NPs/μL of PLGA NPs were incubated with 0.9μM anti-ICAM (final volume ~200 μL) under vigorous shaking at room temperature for 12 h. Unbound Ab molecules were separated from Ab bound PLGA NPs upon washing in 1x PBS, centrifugation at 11,228 rpm for 3 min, and supernatant removal. The pellet containing the Ab coated PLGA NPs was then resuspended at a final concentration of ~$1.7x10^9$ NPs/μL in a solution of 1x PBS

[k] Genisphere® LLC conjugated Cy3 dye to oligo, which is complementary to 3DNA arms and allows 3DNA and Cy3 coupling.

supplemented with 0.3 % BSA and sonicated at low power to separate aggregates. A scheme of anti-ICAM/PLGA synthesis process and controls is shown in **Figure 10**.

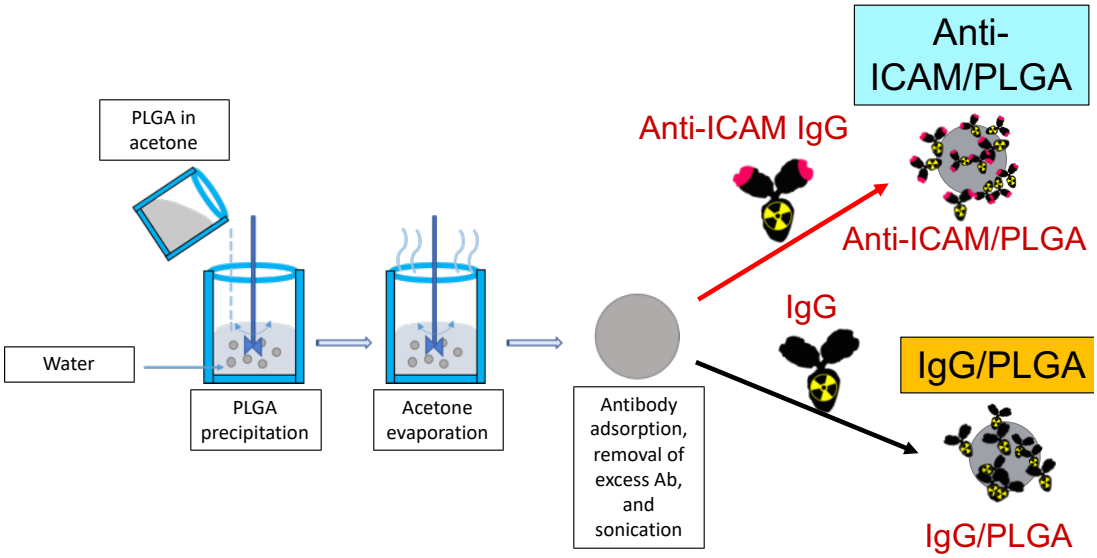

Figure 10. Anti-ICAM/PLGA and IgG/PLGA NP synthesis process.
PLGA is dissolved in acetone and poured into nanopure water under the stirring to allow for NP formation. After acetone evaporation, NPs are concentrated and coated with antibodies via surface adsorption.

4.3. In Vitro Characterization of Nanoparticles

4.3.1. Characterization of Antibody Coupling to PLGA or 3DNA Nanoparticles

The number of Ab molecules coated on the PLGA NPs was determined using the specific radioactivity of ^{125}I-Abs and quantification in a γ-counter as described.[238]

To determine the number of Ab molecules on 3DNA, the ^{125}I-Ab annealed to 3DNA vs. non-annealed ^{125}I-Ab were separated by size exclusion filtration and fractions quantified in a γ-counter to determine coupling efficiency and number of Abs per 3DNA NC as described.[110] In addition, gel electrophoresis was performed at Genisphere® LLC and showed close to 100% efficiency of Ab-oligo-to-3DNA hybridization at the used molar ratios (not shown).

4.3.2. Size and Surface Charge of Nanoparticles

The average diameter, polydispersity index (PDI), and ζ-potential of PLGA and 3DNA NPs were measured before and after Ab functionalization via DLS and electrophoretic mobility using the Malvern Zetasizer (Worcestershire, UK). For PLGA NPs, the measurements were done in nanopure water at $1x10^7$ NPs/μL. The DLS measurements for 3DNA formulations were done in 1x PBS at $3x10^9$ NPs/μL for the 4L and in 1x PBS at $3x10^{10}$ NPs/μL for the 2L. The 3DNA samples were then diluted 2-fold in 1x PBS for the electrophoretic mobility measurements. Alternatively, instead of using 1x PBS, 10 mM NaCl was used for the electrophoretic mobility measurements of the 3DNA formulations.

4.3.3. Stability of Antibody to 3DNA Coupling

Filtration through a 1000 kDa centrifugation filter was first used to study the stability of ^{125}I-labeled 3DNA (11,228 kDa) hybridized or not hybridized with ^{131}I-Ab-

oligo conjugate (174 kDa), before and after incubation with 50% bovine serum for 1 h at 37 °C. Radioisotope tracing in a γ-counter was utilized to quantify the retained and filtered fractions for both counterparts, and TCA precipitation was implemented to detect free iodine (^{125}I) and correct data to avoid artifacts. Free ^{125}I corrected CPM were then used to calculate the percentage of retained and filtered species.

To monitor degradation by gel electrophoresis, naked 3DNA or Ab/3DNA were incubated in 75% human serum or control PBS at 37 °C for 16 h. Densitometry was used to calculate the percentage of intact 3DNA over time.

4.3.4. Degradation of Antibody Coupled 3DNA® in Blood and Organ Homogenates

C57BL/6 mice were anesthetized in order to collect blood samples (≈500 µL from the retro-orbital sinus, heparinized) and then sacrificed. This was followed by the collection of organ samples (kidneys and liver) and their complete homogenization at 28,000 rpm in a homogenizer (Kinematica Polytron™ PT 3100D, Kinematica, Lucerne, Switzerland with Polytron® standard dispersing aggregate blade of 0.7 mm diameter). NP formulation was incubated with blood or organ samples, or 3% BSA in PBS control at 37 °C for selected time periods. Total radioactivity and the radioactivity corresponding to fraction of free ^{125}I for each sample were measured (reported as CPM) in a γ-counter to calculate the percentage of free ^{125}I for each sample. For this purpose, samples were first mixed with 3% BSA in PBS up to a total volume of 1 mL. Samples

were then precipitated with the addition of 200 µL TCA, for a final TCA concentration of 17% (v/v). Precipitation was carried out for 15 min at 4 °C, and then samples were centrifuged at 2687 × g for 10 min. Free ^{125}I CPM, determined from 600 µL of the sample supernatants and total CPM of the samples, measured prior to TCA precipitation, were then used to calculate the percent release of free ^{125}I by using the following equation:

$$\%\ free\ {}^{125}I = 100 \times \frac{2 \times CPM\ supernatant\ (600\ \mu L)}{CPM\ total\ (1200\ \mu L)}.$$

4.4. In Vivo Biodistribution

4.4.1. Mouse Model

Eight-week old C57BL/6 wild type male mice were obtained from Jackson Laboratory (Bar Harbor, ME). The mice were provided food and water *ad libitum* and used in experiments as received and at ~25 g body weight (BW). Mice were intraperitoneally anesthetized with a mixture of 100 mg/kg BW ketamine and 10 mg/kg BW xylazine for each *in vivo* experiment.

All animal experiments were performed in compliance with regulations and under approval of IACUC and the University of Maryland.

4.4.2. Biodistribution of Free ^{125}I and TCA Corrections

Anesthetized C57BL/6 mice were I.V. injected with either ^{125}I-Ab/3DNA (which contains a fraction of free ^{125}I to simulate a process of free ^{125}I generation in controlled manner) or free ^{125}I alone as a control. In both cases, ^{125}I doses were adjusted so that the radioactive signal was between 60 to 1.5×10^6 CPM as detected in a γ-counter with 82% efficiency of detection. This level of signal was selected because it allows measurements in the linear range of the instrument. ^{125}I-Ab/3DNA was injected at 2.15×10^{13} 3DNA particles per kg of BW and 249 μg Ab per kg of BW, carrying a content of ≈30 kCPM of free ^{125}I radiolabel. Hence, free ^{125}I control was injected at 1.3×10^6-1.4×10^6 CPM for a matching dose of free ^{125}I. Blood samples (≈100 μL per draw) were collected from the retro-orbital sinus at selected time points until sacrifice at 60 min, followed by organs collection, including the bladder, brain, heart, kidneys, liver, lungs, spleen, and thyroid gland. All samples were kept on ice, except during their weighing and radioactivity measurements in a γ-counter.

Total CPM data were used as obtained to calculate biodistribution parameters (see the equations below), hereafter referred to as "non-corrected" biodistribution. On the other side, the fraction of free ^{125}I was experimentally determined for the original dose pre-injection (described above) and for each of the blood and organ samples post-injection in order to calculate the "corrected" biodistribution parameters. For this purpose, TCA assay described above for the *in vitro* degradation study was used with minor modifications. Briefly, samples were first mixed with 3% BSA in PBS up to a

total volume of either 1 mL for blood samples or 1.7 mL for organ samples. Blood and homogenized organ samples (as described above) were then precipitated with the addition of 200 µL and 300 µL TCA respectively, for a final TCA concentration of 17% and 15% (v/v) respectively. Precipitation was carried out for 15 min at 4 °C, then samples were centrifuged at 2687 × g for either 10 min for blood samples or 30 min for organ samples. Free ^{125}I CPM were determined from 600 µL of the blood sample supernatants or 1 mL of the organ sample supernatants. Total CPM of the samples, measured prior to TCA precipitation, were then corrected for the presence of free ^{125}I radiolabel by subtracting the free ^{125}I measured after TCA precipitation. Either corrected or non-corrected CPM were used to calculate biodistribution parameters, including the percent of the injected dose (%ID) in blood and each organ, and the same parameter divided per gram of organ (%ID/g) which allows comparison between blood and organ samples of very different weight. Please note that the injected dose is the dose measured prior to injection minus the dose remnant in the syringe after the injection. The following equations were used to calculate the aforementioned parameters:

$$Non\ corrected\ CPM = Total\ CPM,$$

$$Corrected\ CPM = Total\ CPM - Free\ Iodine\ CPM,$$

$$\%\ ID = 100 \times \frac{CPM\ organ\ (corrected\ or\ non\ corrected\ CPM)}{CPM\ dose\ (corrected\ or\ non\ corrected\ CPM)},$$

$$\%\,ID/g = 100 \times \frac{CPM\ per\ gram\ organ\ (corrected\ or\ non\ corrected\ CPM)}{CPM\ dose\ (corrected\ or\ non\ corrected\ CPM)}.$$

4.4.3. Blood Kinetics of Free ^{125}I

In addition, parameters such as half-life ($t_{1/2}$), area under the curve (AUC), clearance, and mean residence time (MRT) were calculated using PKSolver in Microsoft Excel.[252] The $t_{1/2}$ represents the time needed for the clearance of 50% of the ID from the blood. The AUC reflects the total blood exposure to the ID through the time, while the MRT represents the average time that the ID stays in the blood.

4.4.4. Biodistribution of Targeted Formulations in Mice

Anesthetized C57BL/6 mice were injected with ^{125}I-labeled NPs. For comparisons between targeted vs. non-specific 3DNA, injections encompassed 2.15×10^{13} particles per kg BW. For comparisons between 3DNA and PLGA counterparts, injections included 1.29×10^{13} particles per kg BW, with matching number of ^{125}I- Abs per NP (≈ 90 antibody molecules per NP; 249 μg Ab per kg BW). Various other anti-ICAM/3DNA formulations of different targeting valencies, dose concentrations, and sizes were tested as indicated (Chapter 7, **Table 8**). Blood samples were collected at the indicated time points and at sacrifice 60 min after injection, as indicated, followed by collection and weighing of main organs (brain, heart, kidneys, liver, lungs, and

spleen), organ homogenization, and sample precipitation with TCA to eliminate any potential free ^{125}I in the samples, as described above in the section 4.5.1. Radioactivity measurements obtained using a γ-counter were then utilized to calculate the %ID, where the injected dose is the dose measured prior to injection minus the dose remnant in the syringe after the injection. We also calculated the %ID/g which compares relative accumulation in organs with different weight, the localization ratio (LR = %ID/g in an organ : %ID/ g in blood) to express the organ-to-blood distribution, and the specificity index (SI = LR of a targeted formulation : LR of the non-targeted counterpart) to estimate the targeting advantage.[238,241]

4.4.5. Microscopy Visualization of Targeted Formulations in the Lungs

Alternatively, similar *in vivo* experiments were conducted using Ab- and Cy3-coupled 3DNA to visualize these formulations in lung samples isolated from mice either 5 or 60 min after injection. Prior to collecting the lungs, animals were perfused with PBS and, then, fixative (4% paraformaldehyde in PBS). Fixed lung samples were sent to Histoserv for further processing; samples were formalin fixed, embedded in paraffin, sectioned at 15 μm thickness, and mounted onto slides. Samples were then used for hematoxylin and eosin (H&E) staining[1], or were immunostained for confocal

[1] Performed by Histoserv.

microscopy using either Alexa Fluor 488-labeled secondary Ab to examine the colocalization of Ab and 3DNA counterparts of the formulation, or that of 3DNA with polyclonal anti-PECAM-1 + FITC-labeled secondary Ab, to localize formulations with the vascular endothelium. Next, immunostained samples were stained with DAPI to label cell nuclei. Microscopy images were taken using a laser scanning confocal microscope (Zeiss LSM 710 Confocal Microscope) with a 10x or 20x Plan-APOCHROMAT objective, and 405 nm, 488 nm and 555 nm lasers (Zeiss; Oberkochen, Germany).[m]

4.5. Statistical Analysis

Data were calculated as mean ± standard error of the mean (SEM) or standard deviation (SD), where indicated. Animal experiments encompassed n≥5 mice for PLGA NPs or for anti-ICAM/3DNA, and n≥3 for 3DNA alone or non-specific IgG/3DNA. The degradation of the Ab/3DNA in tissue homogenates or BSA/PBS was n≥4. All the other experiments were n≥3. Significance was determined using the Student's unpaired t-test, assuming a p-value of 0.05.

---

[m] Dr. Solomon has helped with fluorescence microscopy experiments. We worked together on the injections, animal perfusions, and imaging, and Dr. Solomon performed deparaffinization and staining of the slides, as well as image processing.

Chapter 5: *A Method to Improve Quantitative Radiotracing-Based Analysis of the In Vivo Biodistribution of Anti-ICAM/3DNA*

Statement: Selected paragraphs, results, and figures regarding Ab/3DNA coupling experiments are from the published manuscript and reproduced with permission: Roki, Nikša, Zois Tsinas, Melani Solomon, Jessica Bowers, Robert C. Getts, and Silvia Muro. "Unprecedently high targeting specificity toward lung ICAM-1 using 3DNA nanocarriers." Journal of Controlled Release 305 (2019): 41-49. These materials have been modified to some extent or not, for incorporation into this thesis.

5.1. Introduction

Targeted NPs, such as anti-ICAM/3DNA, hold great potential to improve drug delivery. Towards this goal, the biodistribution of NP components in an organism provides valuable information that can help in understanding the delivery of NPs, as well as to inform on the possible therapeutic efficacy and side effects of the drug cargo.[253] As such, biodistribution studies are essential in guiding the design of NPs and constitute one of the critical preclinical tests.[253,254]

Among many methods,[253,254] radiotracing method using radioisotopes (e.g., γ emitters such as ^{125}I) is considered the gold standard for biodistribution measurements.

It provides unparalleled quantitation accuracy, very high sensitivity, and relatively good throughput abilities.[236,254] However, the inherent risks of using γ emitters must be balanced against the convenience of analysis and advantages of the method. The radiotracing method consists of the following steps: radiolabeling NP components (e.g., proteins and/or nucleic acids in this case) with radioisotopes of appropriate half-life, *in vivo* administration of NPs with known specific activity to allow their biodistribution, followed by the collection of blood and organs for their *ex vivo* radioactivity quantification.[254]

However, radiotracing may often suffer from uncertainty of whether the label incorporated on the NPs or the free label is being traced. The free label may arise in the samples due to shelf-life degradation of NP formulation pre-administration (e.g., if a sample is labile) or metabolic degradation of NPs in the body (e.g., in blood and organs). Regardless of the origin, the free label can confound biodistribution results since, in most cases, the free label is expected to be handled by the body differently than NP preparation, particularly pertaining to their transport, metabolism, and clearance. Since this cannot be predicted *a priori*, organ-specific measurements of the radiolabeled NPs vs. the free radiolabel are necessary for the accurate and precise corrections of the biodistribution.

In this chapter, we investigated whether precipitation with TCA, an established method used for *in vitro* experiments to separate the free radiolabel from radiolabeled NP components,[255,256] could be applied to more properly define the *in vivo*

biodistribution of anti-ICAM/3DNA. As mentioned, NPs such as anti-ICAM/3DNA are biodegradable and may generate trace amounts of the free label before or after administration.

5.2. Results and Discussion

5.2.1. *In vitro* Characterization of 3DNA Coupling to Primary Antibodies

As explained, the presence of the free label can confound the interpretation of biodistribution results for anti-ICAM/3DNA studied in the subsequent aims. As a first step in improving and testing the biodistribution method, we characterized the ^{125}I-Ab/3DNA formulations, which we used in this study to mimic NPs used in targeting strategies. In particular, 4L 3DNA was used in this study. Prior to Ab coupling, the 3DNA NC had average hydrodynamic diameter of 170 ±7 nm, ζ-potential of -19 ±0.6 mV, and PDI of 0.22 ±0.003, as measured by DLS. The 3DNA NCs were then coupled to an Ab-oligo conjugate by complementarity with 3DNA outer arms.[58,91,110] Either the Ab-oligo or the 3DNA had been labeled with ^{125}I to allow tracing of each counterpart in parallel experiments. Next, we confirmed that Ab-oligo conjugates hybridized on 3DNA, using anti-ICAM-oligo and 4L 3DNA as an example. **Table 1** demonstrates this hybridization-driven coupling as measured by size exclusion filtration. Complexation of Ab-oligo to 3DNA was observed regardless whether Ab-oligo (87%

retention) or 3DNA (91% retention) were traced with a radioisotope, while only minimal retention was found for the control Ab-oligo alone (7%).

Table 1. Coupling of Ab/3DNA.

Condition	Retained (%)	Filtered (%)
Ab/3DNA (track Ab)	87.4	12.6
Ab/3DNA (track 3DNA)	91.4	8.6
Ab	6.9	93.1
3DNA	71.8	28.2

Therefore, direct Ab incorporation by annealing on 3DNA was an efficient process and resulted in an increase in the average hydrodynamic size of 3DNA formulations (Table 2), i.e. from 170 nm prior to Ab coupling to ≈180 nm after the coupling of Ab. Ab/3DNA also showed more negative ζ-potential vs. 3DNA alone (−43 for IgG/3DNA and −37 mV for anti-ICAM/3DNA vs −19 mV for 3DNA alone), while all formulations had similar PDI ≈ 0.2.

5.2.2. Verification of Free ^{125}I Radiolabel Generation from ^{125}I-Ab/3DNA Incubated in Blood and Organ Homogenates

Next, we tested the release of free ^{125}I from the ^{125}I-Ab/3DNA at 37 °C in simulated organ conditions and BSA/PBS. Notably, the PBS buffer was used for Ab to 3DNA coupling, and for the I.V. administration of ^{125}I-Ab/3DNA formulations. Nevertheless, BSA/PBS could be used for the storage of some NP formulations and

was therefore used here to demonstrate the possibility of NP degradation before administration, while incubation in organ homogenates was used to demonstrate the degradation of NPs after their administration. In light of this, free ^{125}I release was evident in the BSA/PBS condition, as well as in all the tested organ samples, namely the blood, kidneys, and liver (ranging from 2 % to 17 %; **Figure 11**). It appeared that under most incubation conditions (except in the kidney homogenate), the majority of the release happened within the first 5 min: 2, 4, 10 and 5 % increase by 5 min; there was no significant change with further incubation: 0.8-, 1.1-, 1.2- and 1.7- fold difference between 5 and 60 min for the BSA/PBS, blood, kidneys and liver respectively (**Figure 11**). Although the release of ^{125}I was modest for our model, indicating the stability of the Ab, it demonstrates the possibility that a small release could happen immediately after injection and confound the *in vivo* biodistribution results. In particular, the release of ^{125}I in the blood compartment could distribute to organs, while ^{125}I released in the organs could be transported to the blood and then reach other organs.

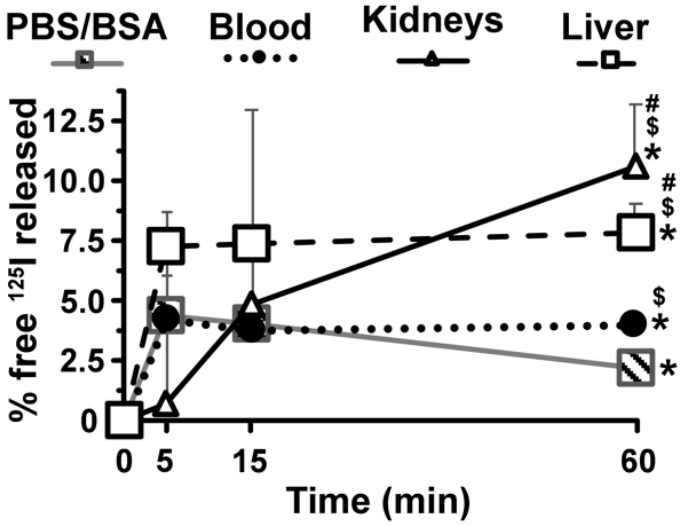

Figure 11. Free ^{125}I generation from ^{125}I-Ab/3DNA incubated in tissue samples.
^{125}I-Ab/3DNA was incubated at 37 °C with either tissue samples (blood and homogenized kidneys and liver) that were collected from euthanized C57BL/6 mice, or in a control buffer (3% BSA in PBS). Free ^{125}I percentage was calculated from the CPM corresponding to the total ^{125}I vs. free ^{125}I in each sample as determined from radioactivity measurements in γ-counter prior and after TCA precipitation respectively. Data are mean ± S.E.M. (n≥4). * Compares 60-min time point vs. the initial time point (i.e. 0 min) for each condition, $ compares blood, kidneys, and liver conditions vs. PBS/BSA condition, # compares kidneys and liver conditions vs. blood condition; ($p < 0.05$ by Student's t-test).

5.2.3. Introduction of Free ^{125}I Radiolabel to ^{125}I-Ab/3DNA in a Controlled Manner

After demonstrating the potential of free ^{125}I generation before and after administration *in vivo*, we decided to test the model formulation, which contains radiolabeled NPs along with the free ^{125}I radiolabel, in order to examine in a controlled manner if the presence of free ^{125}I radiolabel can confound the biodistribution data. **Figure 12** shows the strategy of this study: I.V. injections in mice of either ^{125}I-labeled

NP formulations accompanied with free ^{125}I to better mimic generation of free ^{125}I, or control free ^{125}I alone. The blood circulation kinetics and the biodistribution to blood and organs was traced, as measured prior to and after TCA precipitation.

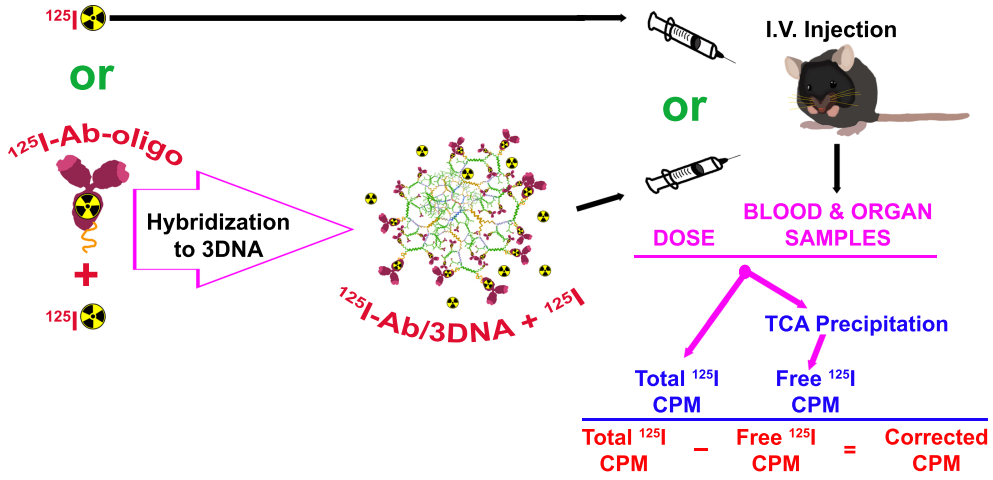

Figure 12. Study strategy.
The goal was to validate a method capable of separating free radiotracer (^{125}I) which may arise from instability of a radiolabeled NP, in order to correct and obtain more accurate *in vivo* biodistribution data. For this purpose, C57BL/6 mice were I.V. injected with control free ^{125}I alone or with 3DNA, coupled to ^{125}I-labeled Ab-oligo which contained a known fraction of free ^{125}I radiolabel. Blood and organs were extracted 1 h after injection, homogenized, and precipitated with TCA to extract and determine total and free ^{125}I CPM, which provided correction for more accurate *in vivo* biodistribution data.

5.2.4. Biodistribution of I.V. Administered Free ^{125}I Radiolabel

Next, to verify the accumulation of the free ^{125}I in blood and organs used for biodistribution studies of NPs, we first determined the biodistribution of free ^{125}I control injection. Briefly, the free ^{125}I was I.V. injected in anesthetized mice, followed by blood collection at indicated time points until sacrifice at 1 h, organ collection and

weighing, and measurements in the γ-counter. As expected for such a small molecule, we observed fast clearance of free ^{125}I from the circulation (**Figure 13A**); only 46% and 24% of the originally injected dose (%ID) remained in blood at 1 min and 5 min after injection. This was followed by a slow clearance phase until 1 h, which was the maximal time period tested; i.e. 16 %ID and 13 %ID were found at 30 min and 60 min after injection (**Figure 13A**). The half-life ($t_{1/2}$), area under the curve (AUC), clearance, and mean residence time (MRT) were 1.3 min, 178.3 %ID×min, 0.6 %ID/min, and 1.9 min, respectively (**Table 2**).

In addition, free ^{125}I accumulated only in small quantities in organs 1 h post injection (**Figure 13B**). For instance, the sum of all radioactivity measured in the bladder, brain, heart, kidneys, liver, lungs, spleen, and thyroid gland amounted to only 11 %ID, suggesting that free ^{125}I may be quickly excreted from the body. Indeed, free ^{125}I was predominantly found in the bladder, kidneys and liver (2, 1, and 2 %ID, respectively; **Figure 13B**), as well as the thyroid gland (4 %ID; **Figure 13B**). The thyroid gland accumulated the highest %ID of free ^{125}I, which can be due to the presence of the sodium-iodide symporter (NIS) involved in active transport of this ion.[257,258] Although kidneys also express the NIS,[258] we did not see similarly high cumulative delivery here, possibly due to ^{125}I incorporation into the urine collected in and likely excreted from the bladder.

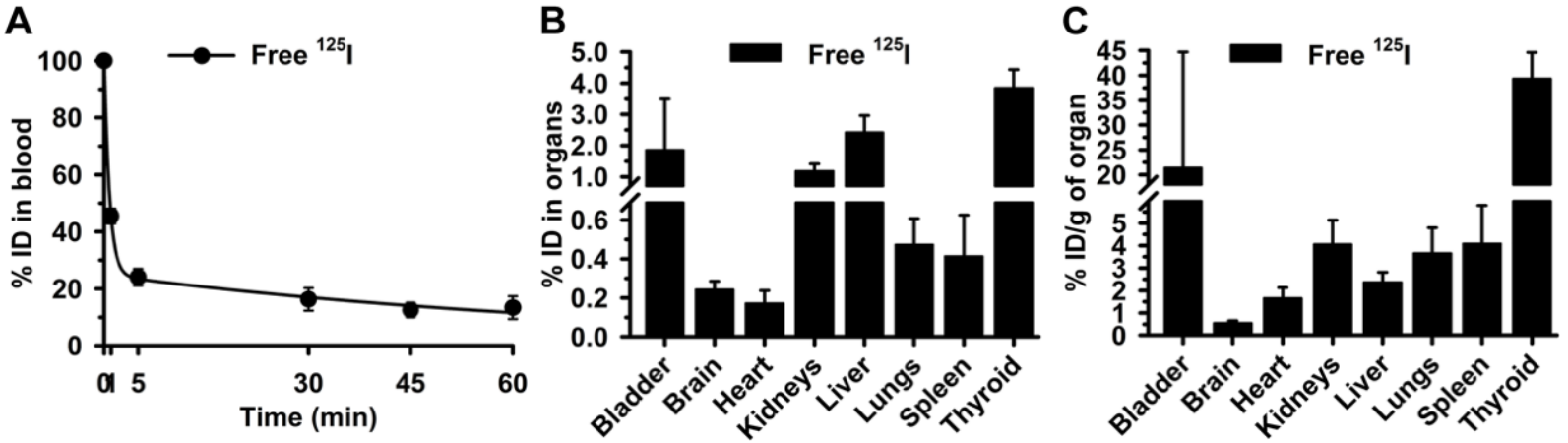

Figure 13. Biodistribution of free ^{125}I.

Free ^{125}I control was I.V. injected in C57BL/6 mice. (A) Blood samples were collected at the indicated post-injection times and (B, C) organs were obtained at sacrifice at 60 min, weighed and measured in γ-counter to calculate the percentage of the injected dose (%ID) found in (A) blood and (B) organs. (C) %ID per gram organ (%ID/g) was calculated to compare the relative "concentrations" of free ^{125}I in organs, given their very different weight. Data are mean ± S.D. (n≥5 mice).

Table 2. Blood kinetic parameters.

Condition	$t_{1/2}$ (min)	CL (%ID/min)	AUC (%ID×min)	MRT (min)
Figure 13A – Control free ^{125}I	1.30	0.56	178.29	1.87
Figure 15A – ^{125}I-Ab/3DNA – Non-corrected	20.32	0.05	1613.40	29.31
Figure 15A – ^{125}I-Ab/3DNA – Corrected using control free ^{125}I from Figure 13A	48.12	0.03	2215.94	69.42
Figure 16A – Free ^{125}I contained in ^{125}I-Ab/3DNA	1.51	0.49	203.57	2.17
Figure 18A – ^{125}I-Ab/3DNA - Corrected using free ^{125}I in the formulation, from Figure 16A	39.56	0.03	2293.74	57.07

AUC = area under the curve; CL = clearance; MRT = mean residence time; $t_{1/2}$ = half-life. (n≥5 mice).

In fact, looking at the free ^{125}I biodistribution relative to the organ weight, i.e. to allow concentration-like comparison among the organs that have very different weights, high %ID of free ^{125}I per gram of organ was found in the thyroid gland and the bladder (39 and 21 % ID/g; **Figure 13C**). All other organs showed relatively low free ^{125}I relative to their weights (**Figure 13C**). The liver free ^{125}I was only 2 %ID/g, although the organ level delivery (%ID) was more prominent for this organ (**Figure 13B**), indicating that radiolabel accumulation in this organ is mostly due to liver's large size and open vasculature due to fenestrated endothelium rather than due to specificity of accumulation. The brain, heart, kidneys, lungs and spleen also had low free ^{125}I amounts, both per organ and per gram of organ (**Figure 13B-C**).

In conclusion, this control experiment indicated that the level of free ^{125}I widely varies among the different compartments in the body, in agreement with the literature,[257] justifying the need to correct ^{125}I data for free label in each compartment (i.e. blood and organs) individually in order to obtain accurate biodistribution results. Namely, if a formulation contains free ^{125}I arising from degradation of NPs, data could not be corrected simply by the amount of free ^{125}I in the injected preparation. Instead, to avoid artifacts in the biodistribution results, the biodistribution in each blood and organ sample would need to be corrected for their free ^{125}I biodistribution.

5.2.5. Identification of Free ^{125}I in Mouse Organs after I.V. Administration of Free ^{125}I Radiolabel

After examining the biodistribution of ^{125}I, we aimed to evaluate the possibility to verify whether this label can indeed be detected as free ^{125}I in blood and organ samples. For this purpose, we adapted an established method which employs TCA, an agent commonly used to precipitate biological polymers (proteins, nucleic acids, and polysaccharides to some extent[255,256]) to separate free radiolabel that may arise due to the instability of NPs before or after administration *in vivo*. In order to implement this method, the organs obtained from the experiment described above, which had been measured for their total radioactive content (**Figure 13**), were homogenized and then mixed with TCA, while blood samples were directly mixed with this reagent. After precipitation and centrifugation, an aliquot of the supernatant was assessed for the content of free ^{125}I. This method demonstrated that most of the free ^{125}I present in the body could indeed be detected as a free species; from the ^{125}I detected in the blood, 93 to 110% was detected as free ^{125}I radiolabel (**Figure 14A**) and from the ^{125}I detected in the organs, 84 to 95% was detected as free ^{125}I radiolabel (**Figure 14B**) was detected as free, respectively, with almost no animal-to-animal variability. This was anticipated since 100% free ^{125}I was injected as a control. Note that this classification of ^{125}I as free species portion in the samples is expressed as % ^{125}I, and is independent from the quantification of ^{125}I found in samples which is expressed as %ID or %ID/g ^{125}I (compare **Figure 13** and **Figure 14**); i.e. 100% of all ^{125}I detected in blood was in free

form although at early and late time points the presence of radiolabel was quite different (46 %ID at 1 min vs. 13 %ID at 60 min). Similarly, organs with higher or lower ^{125}I concentrations (e.g., 39 %ID/g in the thyroid gland vs. 0.6 % ID/g in the brain) contained ~90% free ^{125}I. Hence, these results demonstrated that implementation of organ homogenization, and blood and organ TCA precipitation assay in biodistribution studies enables accurate and precise detection of any free radiolabel present in the samples of interest. Furthermore, this indicates that ^{125}I was not incorporated into body molecules (which would be precipitated by TCA), or at least not in relevant amounts, under the conditions examined. Thus, this method may be reliably used to correct total CPM data for the free radiolabel fraction found in blood and each organ.

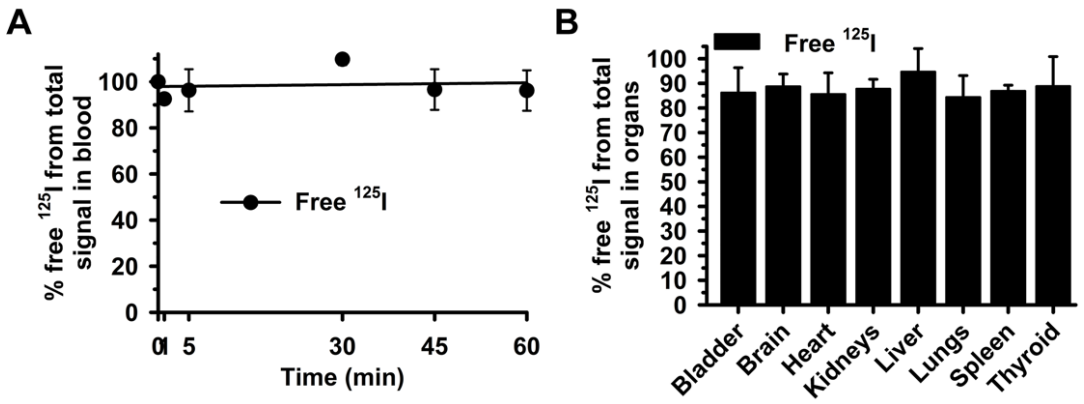

Figure 14. Verification of free ^{125}I signal in blood and organs after TCA precipitation. ^{125}I was I.V. injected in C57BL/6 mice. (A) Blood samples were collected at the indicated times post injection and (B) organs at sacrifice at 60 min for CPM measurements in γ-counter. Data represent the percentage of the total CPM detected in each blood or tissue sample which were identified as free ^{125}I after TCA precipitation. Data are mean ± S.D. (n≥5 mice).

5.2.6. Implementation of Control-free ^{125}I Corrections on the Biodistribution of ^{125}I-Ab/3DNA

After we verified the desired performance of the TCA method using free ^{125}I control and demonstrated that the biodistribution of free ^{125}I *in vivo* ranged broadly among different organs, we wanted to test whether we could use free ^{125}I data obtained from the control experiment (the %ID observed in each organ already obtained as in **Figure 13**) to correct the biodistribution of ^{125}I-radiolabeled NPs (i.e. ^{125}I-Ab/3DNA) for the presence of the free ^{125}I in the blood and organs, assuming the same biodistribution for the free ^{125}I control injection as for the free ^{125}I injected along with the ^{125}I-radiolabeled NPs (**Figure 15**). Using the thyroid gland as an example, TCA can be used to measure the pre-injection CPM corresponding to the free ^{125}I radiolabel (referred to as free CPM), which is present together with the ^{125}I-radiolabeled NPs in the formulation. Moreover, after injection in mice, the biodistribution percentage of the free CPM in the thyroid would be assumed to be the same as the empirically measured biodistribution percentage for the thyroid after the free ^{125}I control injection (e.g., 4%; **Figure 13B**). The assumed free ^{125}I CPM in the thyroid must be then subtracted from the empirically measured total CPM in this organ. The result would correspond to the amount of the NP found in the organ without any free ^{125}I radiolabel, assuming no metabolic degradation of the NP *in vivo* and no influence of NP on free radiolabel biodistribution as measured at 1 h post injection.

To test this correction, we injected mice with ^{125}I-Ab/3DNA as a model NP containing a known and significant amount of free ^{125}I radiolabel (**Figure 12**).[58,91,110] We used a non-specific Ab-oligo (i.e. IgG-oligo) to test the method at hand in this study in order to avoid biodistribution changes and cellular uptake driven by the targeting of specific cell receptors, which may only apply to particular targeting cases and may complicate result interpretation. The size, PDI, and ζ-potential for this formulation was already described at the beginning of the Results and Discussion section.

The biodistribution of 3DNA coupled to control ^{125}I-Ab-oligo (^{125}I-Ab/3DNA) was first assessed without free ^{125}I corrections. For this, the circulation of 3DNA coupled to control ^{125}I-Ab-oligo (^{125}I-Ab/3DNA) was measured at various times after its administration and the organ biodistribution at 60 min (**Figure 15**). ^{125}I-Ab/3DNA disappeared quickly from the circulation (i.e. 45 and 25 %ID at 1 min and 5 min; **Figure 15A** white symbols), which was expected for a non-PEGylated NC.[10,238] The $t_{1/2}$, AUC, clearance, and MRT were 20.3 min, 1613.4 %ID×min, 0.1 %ID/min, and 29.3 min, respectively (**Table 2**). Yet, contrary to free ^{125}I control, ^{125}I-Ab/3DNA did not accumulate preferentially in the thyroid gland (2 %ID and 13 %ID/g; **Figure 15B-C** white bars) but in the liver (28 %ID and 25 %ID/g; **Figure 15B-C** white bars), which was expected for a NP with an Ab coat.[10,110]

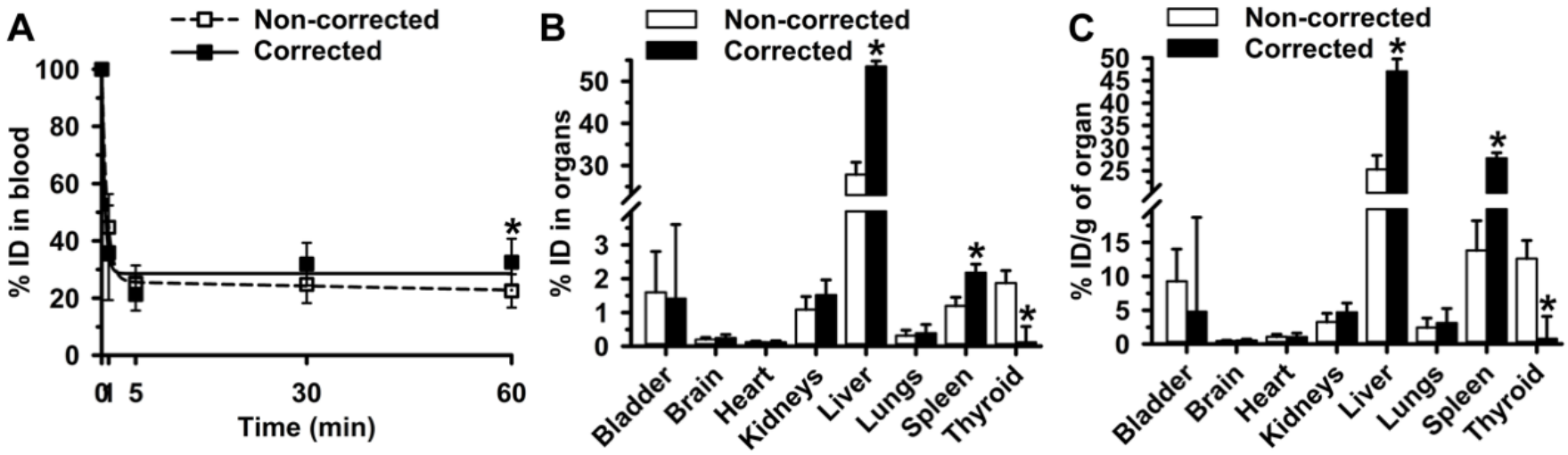

Figure 15. Control free ^{125}I corrections of the ^{125}I-Ab/3DNA biodistribution.

^{125}I-Ab/3DNA with a known amount of free ^{125}I radiolabel CPM was I.V. injected in C57BL/6 mice. Blood and organs were collected and weighed at the indicated times and measured in a γ-counter. Results were calculated from the total CPM measured and referred to the total CPM of the injected dose (including ^{125}I-Ab/3DNA + free ^{125}I radiolabel for non-corrected data), or they were corrected to subtract in each tissue the expected biodistribution of free ^{125}I obtained in Figure 13A-B. (A) Circulation and (B) biodistribution are expressed as percentage of the injected dose (% ID). (C) %ID per gram organ (%ID/g) shows organ concentration. Data are mean ± S.D. (n≥5 mice). *p < 0.05 by Student's t-test.

The results described correspond to non-corrected data. Yet, noticeably, the TCA measurement revealed that the ^{125}I-Ab/3DNA formulation contained 40-50% free ^{125}I radiolabel, therefore making this formulation suitable for testing the correction method. This can be used to study the influence of free label in biodistribution. Therefore, we implemented the correction described above (**Figure 15**, black symbols and bars). Data corrections, based on the biodistribution of free ^{125}I control injection that was already tested, showed some changes regarding the circulation of ^{125}I-Ab/3DNA (44% increase at 60 min; 1.4-fold increase in AUC, **Table 2**), but mainly, it lowered accumulation in the thyroid gland (by 94% for both the %ID and %ID/g of organ) and increased accumulation in the liver and the spleen (e.g., by 92% and 82%, respectively, looking at the %ID parameter), which are expected changes for a NP vs. free ^{125}I.

To validate this correction method, we performed TCA precipitation on the blood and organ samples isolated from these animals, so that the empirical level of free ^{125}I could be obtained within the same experiment. As seen in **Figure 16A**, the level of free ^{125}I measured in blood 60 min after injection was ≈15 %ID, similar to that of free ^{125}I injected alone (compare to **Figure 13A**). The $t_{1/2}$, AUC, and MRT were 1.5 min, 203.6 ID%×min, and 2.2 min, respectively (**Table 2**), also similar to the free ^{125}I injection. Furthermore, the biodistribution of free ^{125}I, varied broadly among organs (e.g., 0.1 %ID in the heart and 3 %ID in the thyroid gland; **Figure 16C**), similar to the variability observed for free ^{125}I injected alone (compare to **Figure 13C**). However, the

biodistribution of free ^{125}I contained within the ^{125}I-Ab/3DNA formulation differed from that of free ^{125}I control: e.g., %ID/g in kidneys lowered by 10%, both %ID and %ID/g in the lung lowered by 32% and 31%, %ID/g was reduced by 18% in the bladder and 42% in the thyroid gland (**Figure 16B, C**). Conversely, the %ID/g increased 17% for the spleen and both the %ID and %ID/g increased by 386% and 335% for the liver. Therefore, the assumption used in this correction method (i.e. a similar free ^{125}I radiolabel biodistribution for the injection of ^{125}I-Ab/3DNA + free ^{125}I radiolabel compared to free ^{125}I alone) is not correct. Speculatively, ^{125}I-Ab/3DNA may compete for the access of free ^{125}I to certain organs, or free ^{125}I may arise from metabolic degradation of ^{125}I-Ab/3DNA after injection. For instance, since the liver is known to play a role in the degradation and disposal of many compounds and carriers, the increase in the distribution of free ^{125}I measured in this organ in animals injected with ^{125}I-Ab/3DNA + free ^{125}I radiolabel may be due to some degradation of the ^{125}I-Ab/3DNA fraction that arrives in this organ. Indeed, degradation of ^{125}I-Ab/3DNA in organ homogenates *in vitro*, particularly liver, demonstrated this to likely be true (**Figure 11**). Such phenomenon would be much less significant in organs which are not involved in clearance and degradation, such as the heart for instance. In addition, ^{125}I-Ab/3DNA may form a protein corona containing albumin from the circulation, a phenomenon observed for many NPs.[30] Albumin has been shown to act as a carrier of ^{125}I.[259] Therefore, if a protein corona forms on ^{125}I-Ab/3DNA, some free ^{125}I radiolabel may associate and travel in the body in this manner. In the case of the liver, since ^{125}I-

Ab/3DNA accumulates significantly in this organ, it may then carry more of the free ^{125}I via protein corona to this organ vs. other organs. Altogether, these and other processes may account for the different biodistribution of free ^{125}I co-injected with ^{125}I-Ab/3DNA. Regardless of the reason, the results indicated that the biodistribution profile of ^{125}I-Ab/3DNA cannot be corrected using the biodistribution of free ^{125}I injected alone. Instead, free ^{125}I must be empirically measured in each body sample to correct biodistribution results within the same experiment.

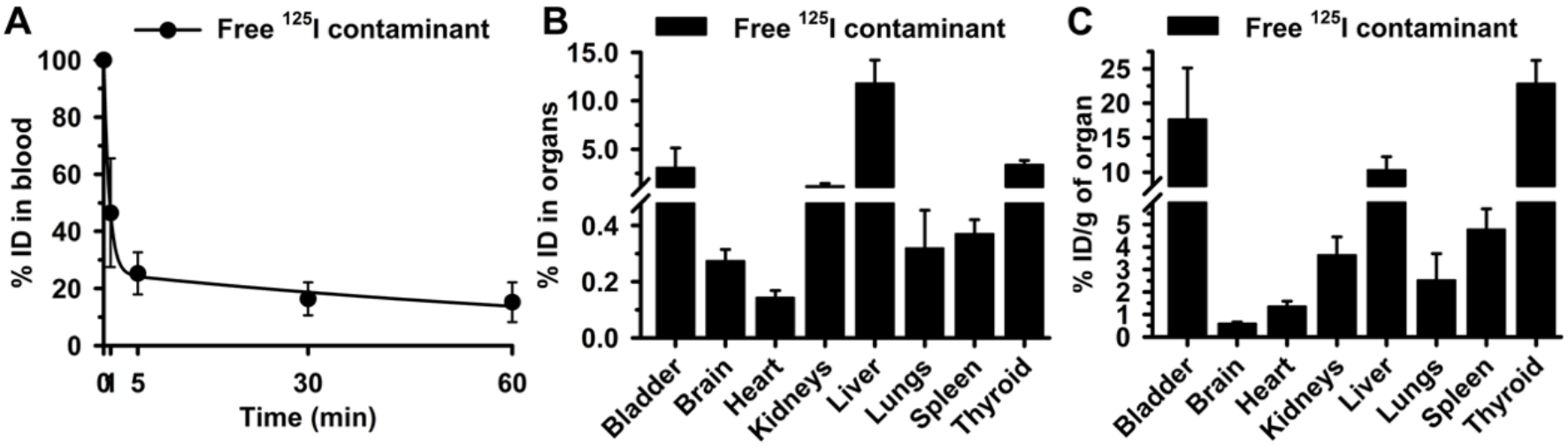

Figure 16. Biodistribution of free ^{125}I radiolabel in ^{125}I-Ab/3DNA.

^{125}I-Ab/3DNA containing a known amount of free ^{125}I radiolabel was injected I.V. in C57BL/6 mice. (A) Blood samples were collected at the indicated post-injection times and (B, C) organs were obtained at sacrifice at 60 min. TCA precipitation rendered CPM of free ^{125}I in each blood and organ sample, from which the percentage of the injected dose (%ID) was calculated by comparison to the total free ^{125}I injected. Data are mean ± S.D. (n≥5 mice).

Additional controls were performed to demonstrate that the TCA precipitation method supports accurate extraction of free ^{125}I from complex samples, e.g., if free ^{125}I would interact with hemoglobin or albumin, as reported.[259,260] For this, we incubated ^{125}I-Ab-oligo (the counterpart labeled in ^{125}I-Ab/3DNA) containing 11.4±0.25% free ^{125}I radiolabel with mouse whole blood (containing heparin to avoid coagulation) or plasma. After 30 min incubation, we performed TCA precipitation and found, respectively, 11.8±0.7% and 12.2±0.75% free ^{125}I in these mixtures. Independently, free ^{125}I alone (100%) was similarly incubated with whole blood or plasma, after which TCA precipitation rendered detection of 102.7±2.0% and 110.8±0.5% free ^{125}I. As additional controls, mixing of non-labeled (cold) Ab/3DNA with free ^{125}I, followed by TCA precipitation rendered 105.1±0.4% free ^{125}I detection, demonstrating that all the free label is detected despite the presence of the carrier. Mixing of cold Ab/3DNA with ^{125}I-Ab-oligo containing 11.4±0.25% free ^{125}I radiolabel lead to detection of 11.0±0.4% free ^{125}I, demonstrating that even if some ^{125}I-Ab-oligo counterpart were to detach from the 3DNA, still this would not interfere with the ability to detect free ^{125}I radiolabel. Hence, the method accurately separates and detects free ^{125}I despite any possible interactions, just as deduced from the *in vivo* data in **Figure 14**.

5.2.7. Implementation of Empirical free ^{125}I Corrections on the Biodistribution of ^{125}I-Ab/3DNA

The results obtained above indicate that the amount of free ^{125}I in each blood and organ sample must be empirically measured within each one experiment to subtract this value from the total CPM encountered in said samples. To prove that this is important, we calculated out of the total CPM found in each blood and organ sample, which percentage corresponded to free ^{125}I, not ^{125}I-Ab/3DNA (**Figure 17**). Results show that much of the label found in blood corresponded to the ^{125}I (e.g., 29% of all CPM in this organ, at 60 min; **Figure 17A**), while in organs this fraction varied broadly from 13% of all free CPM in the spleen to 54% all free CPM in the brain or 95% of all CPM in the bladder (**Figure 17B**).

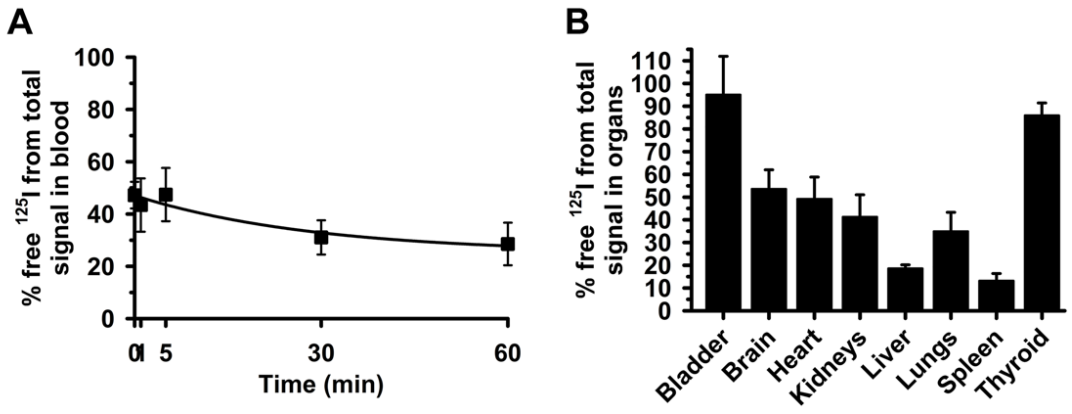

Figure 17. Contribution of free ^{125}I to the total ^{125}I signal found in blood and organs after ^{125}I-Ab/3DNA injection.

C57BL/6 mice were injected with ^{125}I-Ab/3DNA containing a known amount of CPM of free ^{125}I radiolabel. (A) Blood samples were collected at the indicated times post injection and (B) organs at sacrifice at 60 min for CPM measurements in γ-counter. (A-B) Total CPM and free ^{125}I CPM were measured prior and after TCA precipitation, so that the fraction of free ^{125}I over the total CPM in each body compartment was calculated. Data are mean ± S.D. (n≥5 mice).

As seen, the contribution of free ^{125}I radiolabel to the total CPM of each organ sample was highly variable, validating that the best possible correction to obtain "non-free ^{125}I" NP biodistribution data is to subtract free ^{125}I counts in each organ from the total counts in said organ (**Figure 18**). Implementing this correction showed that the blood clearance profile remained similar, although a bit enhanced for the 60 min point (**Figure 18A**). This was expected since both free ^{125}I and ^{125}I-Ab/3DNA were rapidly cleared (**Figure 13A** and **Figure 18A**). The $t_{1/2}$ and MRT were 39.6 min and 57.1 min, respectively (**Table 2**). However, organ accumulation greatly changed after correction for free ^{125}I radiolabel. For instance, accumulation in the bladder and the thyroid gland decreased by 3-fold (**Figure 18B**) since these are the organs which predominantly take

free radiolabel and are not expected to accumulate ^{125}I-Ab/3DNA. On the other hand, accumulation of ^{125}I-Ab/3DNA in the liver and spleen significantly increased upon correction (1.5-fold increase; **Figure 18B**) up to values which agree with previous reports on Ab/NPs of similar size and ζ-potential (e.g., ~30-50% ID/g; [95]). Hence, this correction method was able to accurately remove the free ^{125}I confounding signal. Logically, in organs where free ^{125}I did not substantially accumulate, (e.g., brain, heart, lungs **Figure 13B, C** and **Figure 16B, C**), data corrected had less impact on the biodistribution results (**Figure 18B, C**).

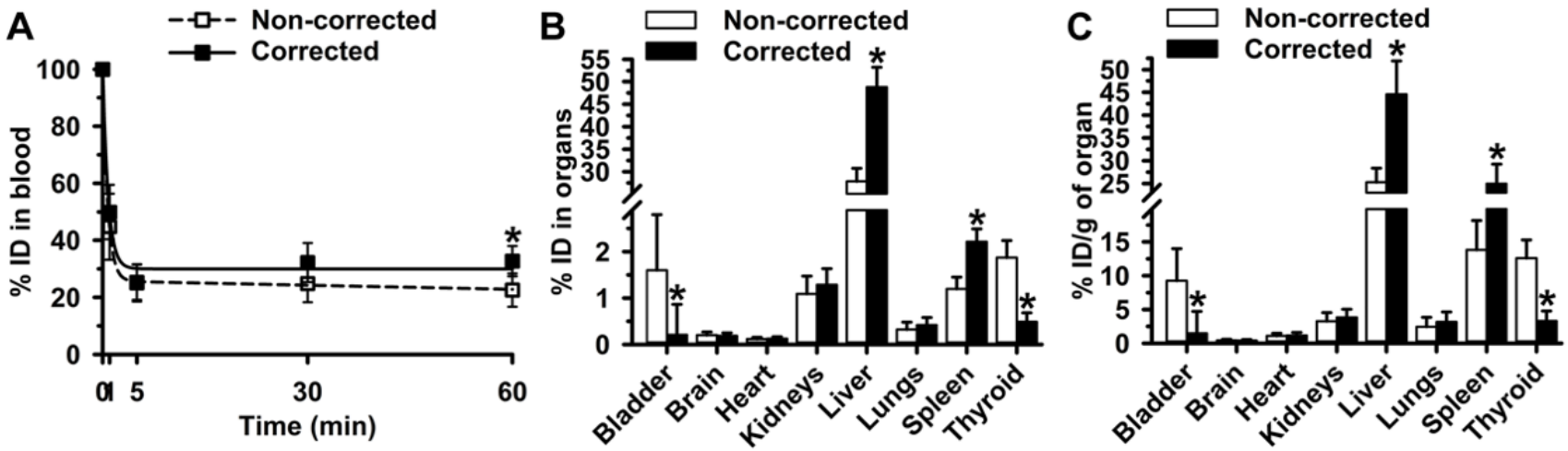

Figure 18. Correction of ^{125}I-Ab/3DNA biodistribution based on empirical free ^{125}I measured within the experiment.

^{125}I-Ab/3DNA with a known amount of free ^{125}I radiolabel, was I.V. injected in C57BL/6 mice. Blood and organs were collected and weighed at the indicated times and measured in a γ-counter. Results were calculated from the total CPM measured and referred to the total CPM of the injected dose, or they were corrected to subtract in each tissue the free ^{125}I CPM empirically measured after TCA precipitation of the same samples. (A) Circulation and (B) biodistribution are expressed as percentage of the injected dose (% ID). (C) %ID per gram organ (%ID/g) shows organ concentration. Data are mean ± S.D. (n≥5 mice). *$p < 0.05$ by Student's t-test.

Finally, to validate this correction method, we injected mice with ^{125}I-Ab/3DNA containing low free ^{125}I radiolabel (10% of the injected dose) as a control. As shown in **Figure 19A**, the contribution of free ^{125}I CPM to the total CPM found in each organ was relatively low, as expected, even very significantly reduced for the bladder and thyroid gland which accumulate the free label. This was in contrast with the high contribution of free ^{125}I CPM of the free ^{125}I control injection (compare to **Figure 17B**). In addition, the biodistribution of ^{125}I-Ab/3DNA formulation containing low radiolabel level was determined and compared to that of ^{125}I-Ab/3DNA with high ^{125}I radiolabel (40-50%, used in the previous experiments). In both cases, corrected and non-corrected data were calculated and the corrected to non-corrected ratio (fold difference between these values) was compared. As shown in **Figure 19B**, there was little difference between the corrected and non-corrected biodistribution of the formulation carrying low free ^{125}I radiolabel ($y \cong 1$ in **Figure 19**; black symbols and bars), unlike the formulation with high level of said radiolabel ($y \neq 1$ in **Figure 19**; white symbols and bars). Therefore, this correction method is valid to obtain accurate biodistribution of radiolabel attached to a NP even in the presence of free radiolabel which may otherwise significantly contribute to the total signal and therefore confound the biodistribution results.

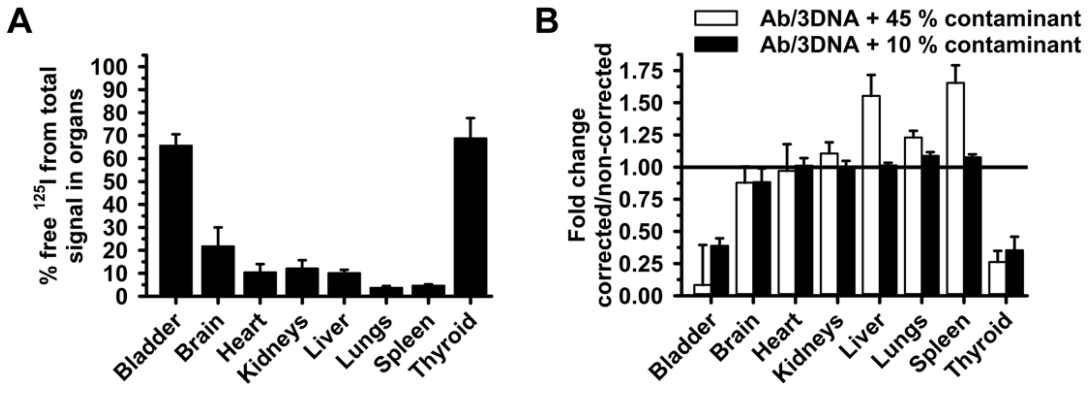

Figure 19. Free ^{125}I content and corrected to non-corrected ratio of the biodistribution of ^{125}I-Ab/3DNA containing no free ^{125}I radiolabel.

Free ^{125}I content and corrected to non-corrected ratio of the biodistribution of ^{125}I-Ab/3DNA containing no free ^{125}I radiolabel. (A) ^{125}I-Ab/3DNA minimal (10%) free ^{125}I radiolabel were I.V. injected in C57BL/6 mice. Total CPM and free ^{125}I CPM were measured prior and after TCA precipitation, so that the fraction of free ^{125}I over the total CPM in each body compartment was calculated. (B) ^{125}I-Ab/3DNA with 10% vs. 45% free ^{125}I radiolabel were injected, and organs were collected and weighed at the indicated times and measured in a γ-counter prior and after TCA precipitation to calculate the biodistribution as the percentage of the injected dose (%ID). This was done from non-corrected data (total CPM in tissue / total CPM in the injected dose) or corrected values ([total – free ^{125}I CPM in tissue] / [total – free ^{125}I CPM in the injected dose]), from where the corrected to non-corrected ratio was calculated. Data are mean ± S.D. (n≥5 mice).

5.3. Conclusion

Our results indicate that the presence of any free radiolabel in biodistribution samples, which could be generated due to NP degradation or a remnant from the NP labeling process, needs to be accounted specifically within the same experiment, for each organ or blood sample, in order to obtain accurate biodistribution results. This precision can be achieved by implementing TCA precipitation of animal samples,

which permits the accurate classification of signals originating from free radiolabel vs. radiolabeled NP.

The accurate biodistribution characterization achieved with this method may provide a vital step in designing and optimizing NP delivery, thereby improving their chances for translation to the clinics; in contrast, confounding biodistribution results may mislead the research and cause suboptimal performance. It can also help with variability in the levels of a free label in formulations to be injected from different synthesis batches or labeled with different radiolabeling species. Moreover, it is technically possible that the TCA method could be used to detect free label generation due to the degradation of NP components. Tracing degradation would be important as different organs have different capacities to metabolize the labeled NP components, and the sites where degradation occurs also vary.

Chapter 6: Unprecedently High and Specific Lung Targeting by 3DNA Functionalized with Anti-ICAM-1 Antibody

Statement: Selected paragraphs, results, figures, and other components in this chapter are from the published manuscript and reproduced with permission: Roki, Nikša, Zois Tsinas, Melani Solomon, Jessica Bowers, Robert C. Getts, and Silvia Muro. "Unprecedently high targeting specificity toward lung ICAM-1 using 3DNA nanocarriers." Journal of Controlled Release 305 (2019): 41-49. These materials have been modified to some extent or not, for incorporation into this thesis.

6.1. Introduction

As described in the background section, ligand-targeted DNA-NPs hold great potential for I.V. drug delivery applications.[58,82,83,90,209,211,216] Nevertheless, their ligand-specific targeting and quantitative biodistribution measurements have not been carefully explored *in vivo*.[19,72] Also, targeting of DNA-NPs to specific sites within the body may be hindered due to the several aspects as explained in the Background, including clearance via scavenger receptors, degradation and metabolic clearance, immunogenicity, etc., all depending on the design of DNA sequence and form.[28,82,139,220,261]

Considering this, our laboratory started exploring Ab/3DNA NCs directed toward specific endothelial markers as a strategy to improve targeted drug delivery. This strategy can potentially ameliorate some of the aforementioned challenges. As explained in the background, targeting ICAM-1 is particularly attractive strategy for enhancing site-specific delivery, as shown by many groups, including ours.[150,262] Due to the high ICAM-1 content and extensive endothelial surface, the full cardiac input, and being a first-pass capillary network, the lungs are preferential and practically direct target for NPs addressed to ICAM-1.[168,237] On the other hand, 3DNA is a particularly attractive candidate for this strategy due to its precise multivalent binding abilities.[89] Specifically, multivalent binding has been shown to be very relevant in targeting ICAM-1 due to its biological role.[152,263,264]

In light of this, a prototype anti-ICAM/3DNA demonstrated highly specific targeting *in vitro*.[58] Nevertheless, the targeting *in vivo* was modest compared to that of well characterized model anti-ICAM/NPs.[110,237,238,241] Hence, in this chapter, we investigated the *in vivo* biodistribution of a new anti-ICAM/3DNA design I.V. injected in mice; this NP design is described in the Innovation section. As explained in the Background, similar Ab/3DNA technology has been incorporated in various other targeting systems showing encouraging functional results.[90–92] Therefore, the biodistribution, as well as the targeting potential of ligand-targeted 3DNA *in vivo* was not established for the new design, and was never explored for the delivery via ICAM-1. Consequently, testing the targetability of anti-ICAM/3DNA *in vivo* will result in new

knowledge that may be applicable to a diverse group of Ab/3DNA and ligand-targeted DNA-NPs, and may help advance targeted drug delivery for lung applications.

6.2. Results and Discussion

6.2.1. *In Vivo* Biodistribution of Anti-ICAM Antibody and Anti-ICAM Antibody-oligonucleotide

3DNA functionalization technology requires the conjugation of anti-ICAM Abs (anti-ICAM) with oligonucleotides (referred to as anti-ICAM-oligo), to allow for their hybridization to 3DNA. Hence, we first verified that the *in vivo* biodistribution and specific targeting of anti-ICAM-oligo was as expected, particularly to the lungs. Briefly, either the ^{125}I-radiolabeled anti-ICAM-oligo or ^{125}I-radiolabeled anti-ICAM were I.V. injected in anesthetized mice, followed by the collection of blood at indicated time points until sacrifice at 1 h, and organ collection. These samples were then weighted, and their radioactivity was measured to determine blood and organ biodistribution using corrections of the free radiolabel as explained in Chapter 5. The blood kinetics showed fast initial removal from the blood for both anti-ICAM-oligo and anti-ICAM: < 59% of the injected dose (% ID) remained in the blood 1 min following administration (**Figure 20A**). Noteworthy, the anti-ICAM-oligo was removed from the blood faster than the anti-ICAM: 4.1% and 49.5% ID by 5 min, respectively. The fast removal of the anti-ICAM-oligo from the bloodstream was

unexpected considering anti-ICAM's long circulation in the bloodstream. This fast removal of anti-ICAM-oligo may be associated either with anti-ICAM-oligo manufacturing steps or the presence of oligonucleotides and linkers, either of which could alter the physical, chemical, and biological properties of anti-ICAM.

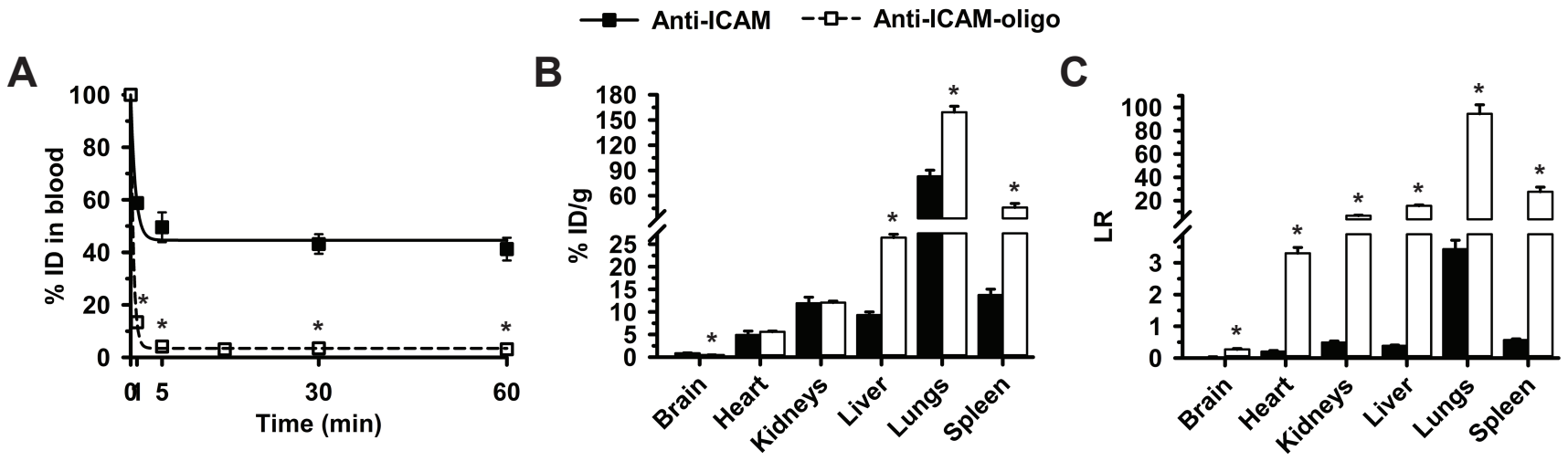

Figure 20. Circulation and biodistribution of anti-ICAM-oligo Ab.

^{125}I-anti-ICAM or ^{125}I-anti-ICAM-oligo were I.V. injected in C5BL/6 mice. (A) Circulation was calculated at the indicated times between injection and at sacrifice at 60 min, as the percentage of the injected dose (% ID). (B) Organ biodistribution at sacrifice was calculated as % ID per gram (%ID/g) to compare organs of different weight. (C) Organ-to-blood distribution expressed as the localization ratio (LR), was calculated as % ID/g in an organ divided by % ID/g in blood. Data are mean ± S.E.M. *Compares anti-ICAM vs. anti-ICAM-oligo ($p < 0.05$ by Student's t-test).

Importantly, biodistribution to the organs showed that the lungs remained the primary target for anti-ICAM-oligo as expected, and the targeting was, in fact, improved compared to anti-ICAM (**Figure 20B and Figure 21A**). Specifically, the %ID/g for lung delivery was 1.9-fold higher for the anti-ICAM-oligo compared to anti-ICAM (**Figure 20B**). Delivery to the clearance organs, such as liver and spleen, also increased for the anti-ICAM-oligo compared to the anti-ICAM: e.g., 2.8 and 3.3-fold for %ID/g, respectively (**Figure 20B and Figure 21A**).

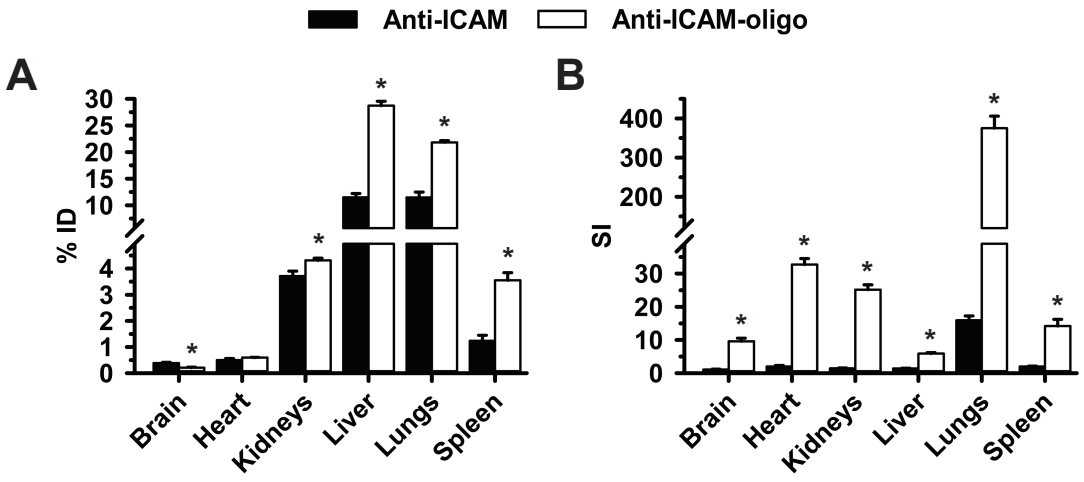

Figure 21. Specific targeting of anti-ICAM-oligo Ab.
^{125}I-anti-ICAM or ^{125}I-anti-ICAM-oligo were I.V. injected in C5BL/6 mice. (A) Organ distribution at sacrifice (60 min) was expressed as the percentage of the injected dose (% ID). (B) Specificity index (SI) represents the tissue-over-blood accumulation for the targeted vs. the non-targeted formulation (see Materials and Methods). Data are mean ± S.E.M. *Compares anti-ICAM vs. anti-ICAM-oligo ($p < 0.05$ by Student's t-test).

Moreover, the localization ratio (LR), which is a measure of the tissue-to-blood distribution (i.e., LR is the ratio of the %ID/g in an organ over the %ID/g in the blood), showed improved organ retention for the anti-ICAM-oligo compared to the anti-ICAM

(**Figure 20B**). Targeting specificity (SI), which is used to estimate the targeting advantage (SI is the LR of a targeted formulation over LR of the non-targeted counterpart), showed 375-fold enhancement in lung targeting for the anti-ICAM-oligo compared to the non-specific IgG control counterpart (**Figure 21B**). This level of specific lung targeting was drastically improved for the anti-ICAM-oligo by a 23.5-fold increase compared to the anti-ICAM. In addition, the anti-ICAM-oligo targeting was specific for the rest of the organs shown: 9.6-, 32.7-, 25.2-, 5.9-, and 14.2-fold over non-specific control for the brain, heart, kidneys, liver, and spleen, respectively (**Figure 21B**). Specific targeting to organs other than the lungs was expected since ICAM-1 is expressed by the endothelial and other cells found in these organs.[7] These results are in agreement with other ICAM-1-targeted formulations reported in literature.[7,152,241,262] The increase in lung targeting of anti-ICAM-oligo compared to anti-ICAM may be due to the anti-ICAM-oligo manufacturing steps or the presence of oligonucleotides and linkers, as mentioned in regards to differences in their circulation profile. Nevertheless, the anti-ICAM-oligo is a suitable ligand to test 3DNA targetability to ICAM-1.

6.2.2. Characterization of Antibody/3DNA

In order to investigate the biodistribution and targeting specificity of anti-ICAM/3DNA, we utilized 3DNA and IgG/3DNA formulations as non-specific controls. These controls were also used to distinguish the role of the surface properties pertaining to the pristine 3DNA, presence of Abs, or presence of targeting moiety. As

mentioned in the Background section, these surface properties not only influence specific interactions, but also non-specific interactions, degradation, and clearance.

In the previous chapter, we confirmed efficient Ab-oligo hybridization with 3DNA as measured by size exclusion filtration (**Table 1**) using radiolabeled 3DNA and anti-ICAM counterparts, which has allowed us to determine the number of Ab-oligo molecules per each 3DNA NC (see Materials and Methods). This resulted in an increase in the average hydrodynamic size of 3DNA formulations (**Table 3**): from 170 nm prior to Ab coupling to ~180 nm after the coupling of oligo-IgG or oligo-anti-ICAM. Ab/3DNA also showed more negative ζ-potential vs. 3DNA alone (−43 for IgG/3DNA and −37 mV for anti-ICAM/3DNA vs −19 mV for 3DNA alone), while all formulations had similar PDI ≈ 0.2.

Table 3. Characterization of 3DNA and PLGA formulation size, surface charge, and polydispersity.

Formulation	Size (nm)		PDI		ζ-potential (mV)	
	Mean	SEM	Mean	SEM	Mean	SEM
3DNA						
Non-coated	170.4	7.5	0.220	0.033	-19.1	0.6
IgG-coated	181.2	5.1	0.231	0.019	-42.7	0.5
Anti-ICAM-coated	179.5	5.7	0.251	0.017	-37.5	0.6
PLGA NP						
Non-coated	154.4	1.4	0.071	0.007	-59.4	0.6
IgG-coated	196.0	6.6	0.224	0.012	-36.8	0.5
Anti-ICAM-coated	208.7	1.5	0.174	0.007	-32.3	0.2

In addition, we tested the stability of this coupling under physiological-like conditions. As explained in the Materials and Methods section, we utilized size exclusion filtration with MWCO such as that the free Abs and potentially the degraded fragments could pass through the filter, while Ab/3DNA or 3DNA would be retained by the filter, allowing us to determine the stability of the Ab/3DNA and 3DNA samples, as well as Ab to 3DNA hybridization stability (Chapter 5, **Table 1**). Incubation for 1 h in the presence of serum did not affect size-dependent retention of Ab/3DNA using the described filtration assay (**Table 4**), regardless whether Ab-oligo (86% retention) or 3DNA (100% retention) were traced. As control, no retention (0%) was detected for non-coupled Ab-oligo and, interestingly, retention of non- coupled 3DNA decayed from 72% to 33% after serum incubation. This suggests that 3DNA is sensitive to serum, likely due to the nuclease degradation. Namely, the nucleases present in the serum can cause fractionation of 3DNA into smaller units that can pass through the filter. However, when its outer layer displays Abs, the Ab coating seems to protect the 3DNA core, decreasing its degradation.

This notion was further validated by an independent assay performed by Genisphere® LLC, where the stability of 3DNA, with or without Ab coating, was compared in an electrophoretic setting (see Materials and Methods) upon incubation with control buffer or serum. Genisphere® LLC showed high stability by 3DNA in control buffer regardless of Ab coupling (close to 100% intact formulations even after 16 h incubation, **Figure 22**). As expected, they also observed that non-coupled 3DNA

decayed over time in serum, with only 11% intact 3DNA observed by 16 h, rendering a half-life of ~9.5 h. However, they found that Ab/3DNA appeared 60% intact by 16 h with a corresponding half-life of ~26 h, again suggesting a protective role of the Ab coat on 3DNA, rendering a ~2.7-fold longer half-life.

Table 4. Stability of Ab/3DNA in serum.

Condition	Retained (%)	Filtered (%)
Ab/3DNA (track Ab)	86.0	14.0
Ab/3DNA (track 3DNA)	100.0	0.0
Ab	0.0	100.0
3DNA	33.3	66.7

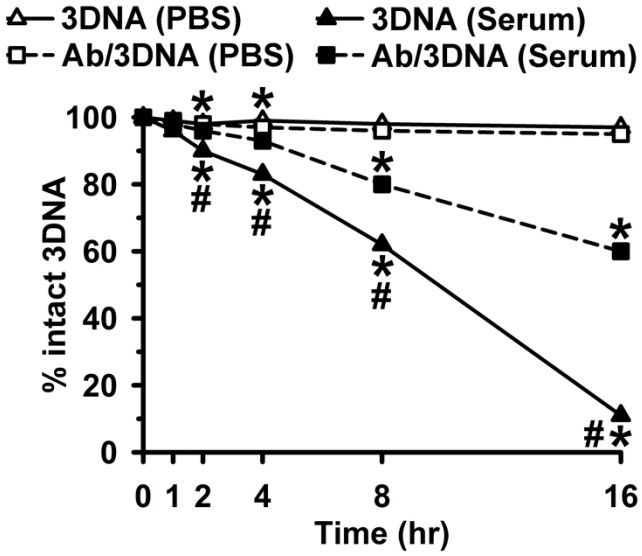

Figure 22. Stability of 3DNA with and without Ab coat.

Non-coupled 3DNA and 3DNA coated with control IgG-oligo conjugate (Ab/3DNA) were incubated in PBS vs. 75% serum up to 16 h. At the indicated times, 3DNA degradation was quantified using gel electrophoresis and imaging. Data are mean ± S.E.M. *Compares serum vs. PBS for each formulation; #compares Ab/3DNA vs. 3DNA ($p < 0.05$, Student's t-test).

These data are in agreement with literature showing that engineered DNA structures tend to be more stable than natural DNA conformations, and additional coatings further enhance stability.[142,187,191] For instance, a DNA-based delivery system consisting of DNA strands tightly packed on the surface of metal NPs was shown to have 4-fold increased resistance to DNase I *in vitro* vs. naked DNA matching controls (from 24 to 100 min half-life).[194] This was believed to be mediated by high local salt concentrations due to the negatively charged surface of the spherical DNA and the tight packing of DNA strands, which either posed steric hindrances for nucleases to reach this substrate, and/or high local salt concentration affected the enzyme function.[194] In addition, fluorescently-labeled DNA origami was also shown to be about 50% stable for 24 h upon uptake by cells in culture while regular DNA degraded much faster.[195] Furthermore, the complexation of DNA with other materials, whether intentionally for drug delivery application or naturally, further demonstrated protection from fast degradation.[226,251,265] Hence, it is likely that the 4L structural conformation of 3DNA makes it relatively stable and Ab coating further enhances its longevity (**Figure 22**).

6.2.3. *In Vivo* Biodistribution of Anti-ICAM/3DNA

After this characterization, we examined the biodistribution and specific targeting of anti-ICAM/3DNA and corresponding controls in mice. First, their circulation was monitored for 60 min (**Figure 23A**). Anti-ICAM/3DNA was redistributed faster from the bloodstream than controls IgG/3DNA and 3DNA alone,

e.g. 17.6%, 41.9%, and 53.3% ID in blood at 1 min, respectively (**Figure 23A**). At 60 min, however, both 3DNA alone and anti-ICAM/3DNA showed low blood levels, i.e. 7.3% vs. 3.0% ID respectively, while IgG/3DNA was 28.6% ID. The faster removal of 3DNA alone vs. IgG/3DNA is in agreement with the increased stability of Ab-coated 3DNA observed *in vitro*. On the other hand, the fact that anti-ICAM/3DNA shows shorter circulation time pairs well with a phenomenon previously observed for anti-ICAM NPs, including polystyrene or PLGA formulations, shown to be due to fast targeting of endothelial ICAM-1, which is readily accessible from the bloodstream.[7,152,241] Moreover, the removal of Ab/3DNA from the bloodstream was faster compared to prototype 3DNA formulations, also tested in this study by our lab, although not shown here.[110]

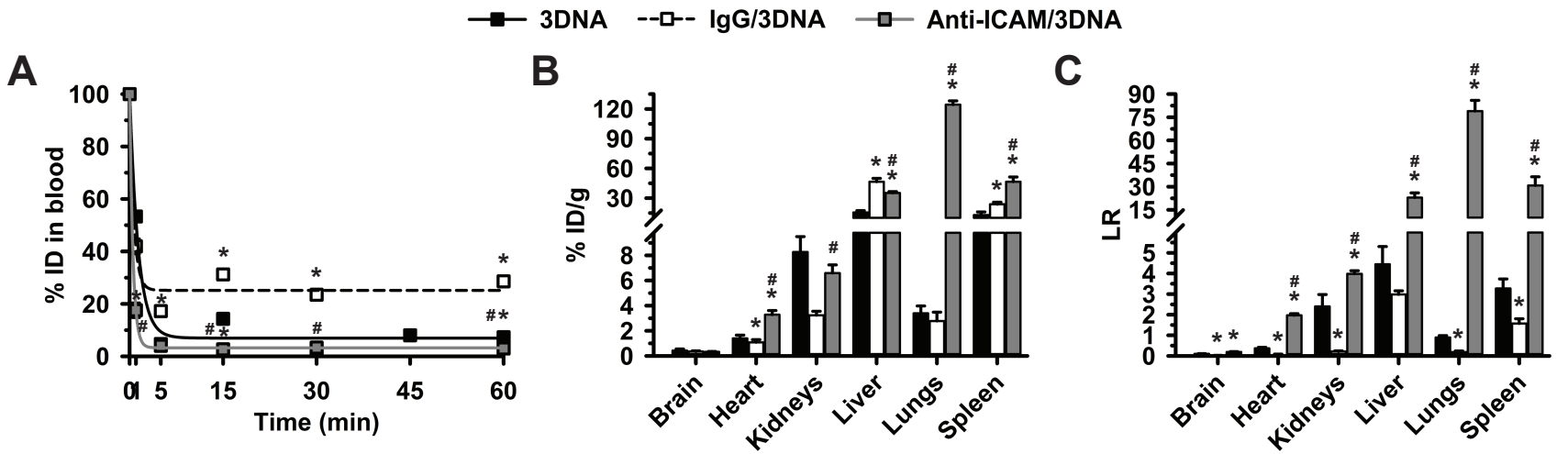

Figure 23. Biodistribution of anti-ICAM/3DNA.

^{125}I-IgG/3DNA, ^{125}I-anti-ICAM/3DNA, or control ^{125}I-3DNA were I.V. injected in C5BL/6 mice. (A) Circulation was calculated at the indicated times between injection and at sacrifice at 60 min, as the percentage of the injected dose (% ID). (B) Organ biodistribution at sacrifice was calculated as % ID per gram (%ID/g) to compare organs of different weight. (C) Organ-to-blood distribution expressed as the localization ratio (LR), was calculated as % ID/g in an organ divided by % ID/g in blood. Data are mean ± S.E.M. *Compares either Ab/3DNA vs. 3DNA alone; #compares anti-ICAM/3DNA vs. IgG/3DNA ($p < 0.05$ by Student's t-test).

In accord with the concept that fast bloodstream removal does not necessarily impair binding of readily accessible targets such as ICAM-1, anti-ICAM/3DNA remarkably accumulated in the lung, the main ICAM-1 target: 18.0% ID by 60 min (**Figure 24A**) and 124.3% ID/g (**Figure 23B**), well above lung accumulation of IgG/3DNA (0.4% ID and 2.8% ID/g) or prototype anti-ICAM/3DNA.[110] Accumulation of anti-ICAM/3DNA in the liver (40.2% ID and 35.2% ID/g) was lower than that of IgG/3DNA (50.2% ID and 46.5% ID/g). In addition, anti-ICAM/3DNA surpassed IgG/3DNA in other organs, including the heart, spleen, etc. (**Figure 23B**). 3DNA without Ab coating was least abundant in the liver (20.8% ID and 15.5% ID/g) and most abundant in the kidney (3.2% ID and 8.3% ID/g), which agrees with *in vitro* observations of its lower stability, and may result in faster liver degradation with kidney clearance of small degradation products. Ultimately, the localization ratio (LR), which is a measure of the tissue-to-blood distribution, showed good organ retention of anti-ICAM/ 3DNA over control formulations (**Figure 23C**). Moreover, the lung-to-liver LR (not shown) was 3.45 for anti-ICAM/3DNA vs. 0.06 for IgG/ 3DNA, representing a remarkable targeting specificity (SI), which is used to estimate the targeting advantage (SI is the LR of a targeted formulation over LR of the non-targeted counterpart); the SI showed 424- and 88-fold enhancement in lung targeting compared to IgG/ 3DNA and 3DNA, respectively (**Figure 24B**).

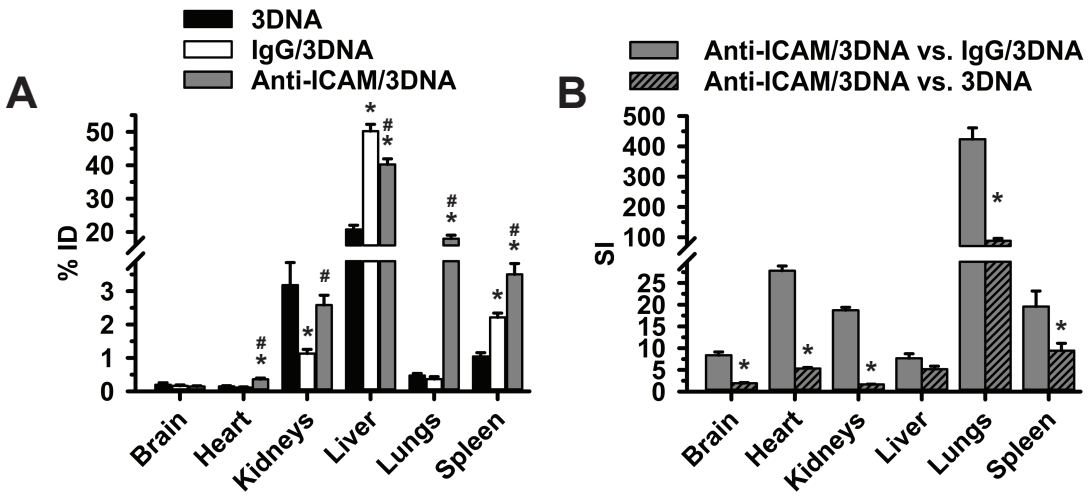

Figure 24. Biodistribution and specific targeting of anti-ICAM/3DNA.
^{125}I-IgG/3DNA, ^{125}I-anti-ICAM/3DNA, or control ^{125}I-3DNA were I.V. injected in C5Bl/6 mice. (A) Organ distribution at sacrifice (60 min) was expressed as the percentage of the injected dose (% ID). (B) Specificity index (SI) represents the tissue-over-blood accumulation for the targeted vs. the non-targeted formulation (see Materials and Methods). Data are mean ± S.E.M. *Compares either Ab/3DNA vs. 3DNA alone; #compares anti-ICAM/3DNA vs. IgG/3DNA ($p < 0.05$ by Student's t-test).

6.2.4. Comparison of Anti-ICAM Ab and Anti-ICAM/3DNA Regarding their *In Vivo* Biodistribution

We further compared the biodistribution and blood kinetics of anti-ICAM/3DNA and a control anti-ICAM Ab (anti-ICAM), upon their I.V. administration in mice. Although both formulations were rapidly removed from the bloodstream, anti-ICAM/3DNA was removed much faster than anti-ICAM Ab: 4.0% and 49.5% ID at 5 min, respectively (**Figure 25A**). The faster removal of NPs from the bloodstream compared to Abs is in agreement with the findings in the literature.[152]

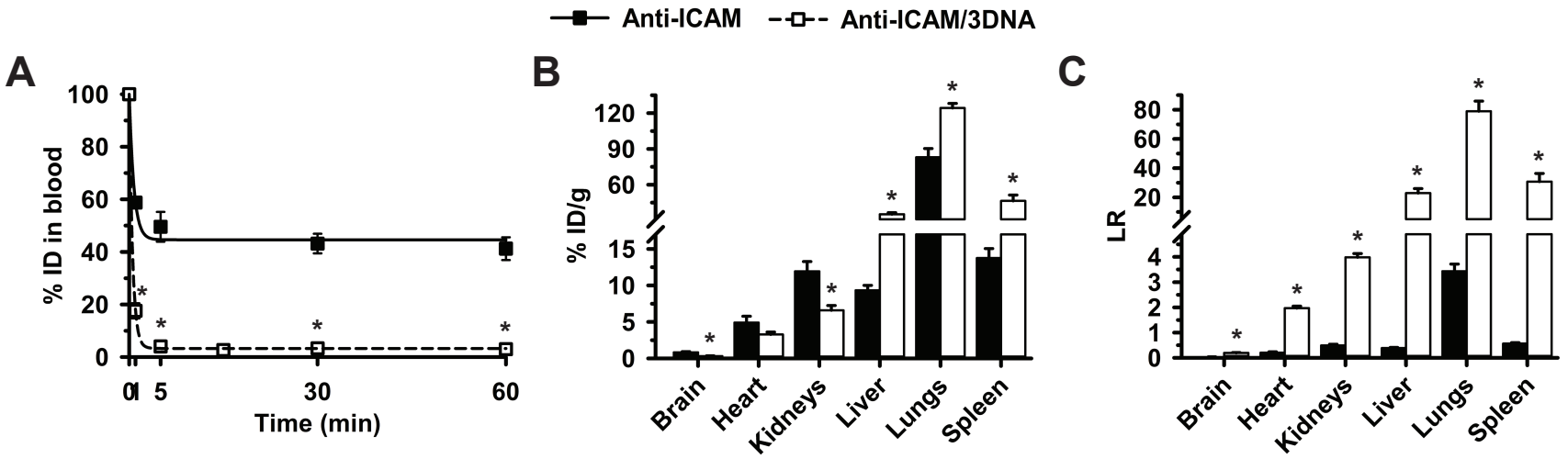

Figure 25. Comparative biodistribution of anti-ICAM/3DNA vs. anti-ICAM Ab.

^{125}I-anti-ICAM/3DNA, or ^{125}I-anti-ICAM Ab were I.V. injected in C5BL/6 mice. (A) Circulation was calculated at the indicated times between injection and at sacrifice at 60 min, as the percentage of the injected dose (% ID). (B) Organ biodistribution at sacrifice was calculated as % ID per gram (%ID/g) to compare organs of different weight. (C) Organ-to-blood distribution expressed as the localization ratio (LR), was calculated as % ID/g in an organ divided by % ID/g in blood. Data are mean ± S.E.M. *$p < 0.05$ by Student's t-test.

The faster removal of anti-ICAM/3DNA from the bloodstream compared to anti-ICAM, which was expected due to the larger size and multivalent presentation of targeting ligands by anti-ICAM/3DNA, occurred because of enhanced biodistribution to the lungs, liver, and spleen (**Figure 25B and Figure 26A**). In particular, compared to anti-ICAM, anti-ICAM/3DNA showed 1.6-, 3.5-, and 2.8-fold greater %ID for the lungs, liver, and spleen, respectively, which encompassed a total of 61.8% vs. 24.2%ID found in these organs for the anti-ICAM/3DNA vs. anti-ICAM, respectively. Also, the biodistribution of the anti-ICAM/3DNA to the kidneys and brain was lower compared to the anti-ICAM, with no significant change in the heart: e.g., 0.7-, 0.4-, and 0.7-fold difference in the %ID, respectively. Nevertheless, the organ to blood localization ratio was enhanced for anti-ICAM/3DNA in all the organs as compared to anti-ICAM (**Figure 25C**). Moreover, anti-ICAM/3DNA specifically targeted all the organs, and the specificity of targeting was enhanced compared to anti-ICAM: 26.6-, 5.5-, 9.8-, 13.0-, 7.8-, and 13.9-fold increase for the lungs, liver, spleen, kidneys, brain, and heart, respectively (**Figure 26B**).

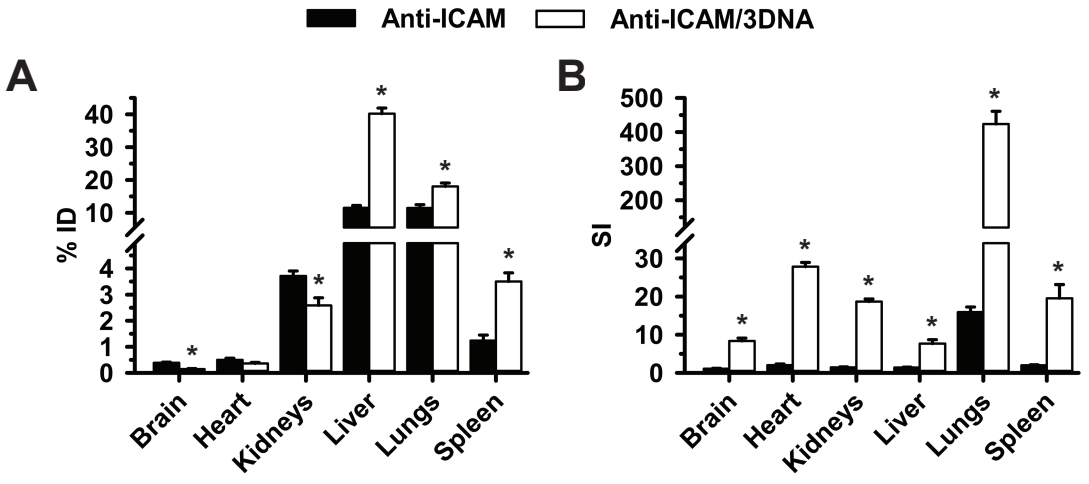

Figure 26. Comparative biodistribution and specific targeting of anti-ICAM/3DNA vs. anti-ICAM Ab.

^{125}I-anti-ICAM/3DNA, or ^{125}I-anti-ICAM Ab were I.V. injected in C5BL/6 mice. (A) Circulation was calculated at the indicated times between injection and at sacrifice at 60 min, as the percentage of the injected dose (% ID). (B) Organ biodistribution at sacrifice was calculated as % ID per gram (%ID/g) to compare organs of different weight. (C) Organ-to-blood distribution expressed as the localization ratio (LR), was calculated as % ID/g in an organ divided by % ID/g in blood. Data are mean ± S.E.M. *$p < 0.05$ by Student's t-test.

6.2.5. Visualization of Anti-ICAM/3DNA Targeting the Lungs *In Vivo*

Lung targeting was further verified using fluorescence microscopy to visualize anti-ICAM/3DNA in the lungs. For these experiments, 3DNA was labeled with Cy3 and Abs as indicated. Lung perfusion was performed to remove blood from the lungs, followed by organ fixation and processing by the Histoserv company. Dr. Solomon has helped with these experiments: we worked together on the injections, animal perfusions, and imaging, and Dr. Solomon performed deparaffinization and staining of the slides, as well as image processing. Fluorescence images showed profuse presence

of anti-ICAM/3DNA, but not IgG/3DNA in the lung tissue (**Figure 27A**). Moreover, anti-ICAM/3DNA formulation colocalized with PECAM-1-positive endothelium (**Figure 27B**), as expected. Anti-ICAM/3DNA seemed to locate on the endothelial surface and intracellularly (**Figure 27B**), although detailed studies to define mechanistic aspects will need to compare various time points in appropriate transgenic or knockout models. Importantly, dual-color tracing of 3DNA (red) vs. Ab (green) counterparts revealed that both components colocalized in the lung tissue (**Figure 27A**), further supporting anti-ICAM-mediated targeting of 3DNA. Histological examination showed no apparent differences between the lungs of mice injected with anti-ICAM/ 3DNA vs. IgG/3DNA. This is despite profuse pulmonary accumulation of the anti-ICAM/3DNA, suggesting relative safety which will be examined in detail in future studies.

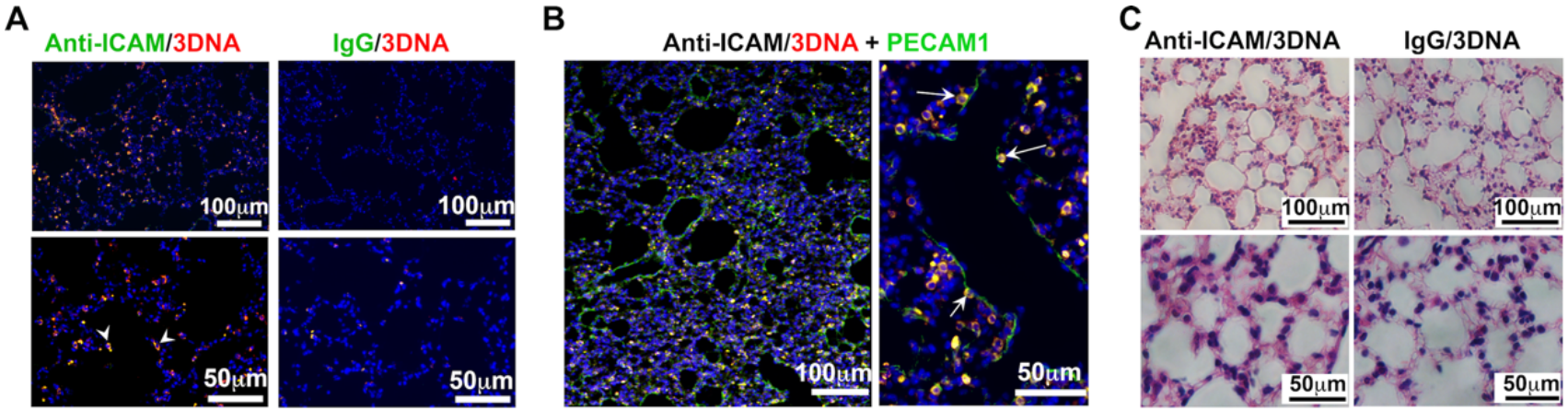

Figure 27. Visualization of anti-ICAM/3DNA in the lungs and histology.

Control IgG/Cy3-3DNA or anti-ICAM/Cy3-3DNA were I.V. injected in C57BL/6 mice and lungs were isolated and processed at sacrifice at 60 min. (A) Confocal microscopy showing Cy3-3DNA (red), while the Ab counterpart was visualized using a FITC- secondary Ab (green). Arrowheads show colocalization of the Ab with cy3-3DNA. Cell nuclei were stained blue with DAPI. (B) Confocal microscopy showing anti-ICAM/Cy3-3DNA (red) and endothelial cells visualized using polyclonal anti-PECAM-1 + FITC-secondary Ab (green). Arrows indicate colocalization of cy3-3DNA with PECAM-1. Cell nuclei were stained blue with DAPI. (C) H&E staining. Respective scale bars are shown. Dr. Solomon helped with this experiment as described in the text.

In addition, to better understand the fast blood clearance of anti-ICAM/3DNA as seen in **Figure 23A**, which may be caused by fast targeting to ICAM-1 on the surface of blood vessels, we decided to visualize anti-ICAM/3DNA at an earlier time point. Indeed, 5 min after injection, fluorescence microscopy showed abundant anti-ICAM/3DNA, but not IgG/3DNA colocalization with PECAM-1-positive endothelium throughout the lungs (**Figure 28**). Therefore, lung targeting was rapid and well-evidenced within 5 min of administration.

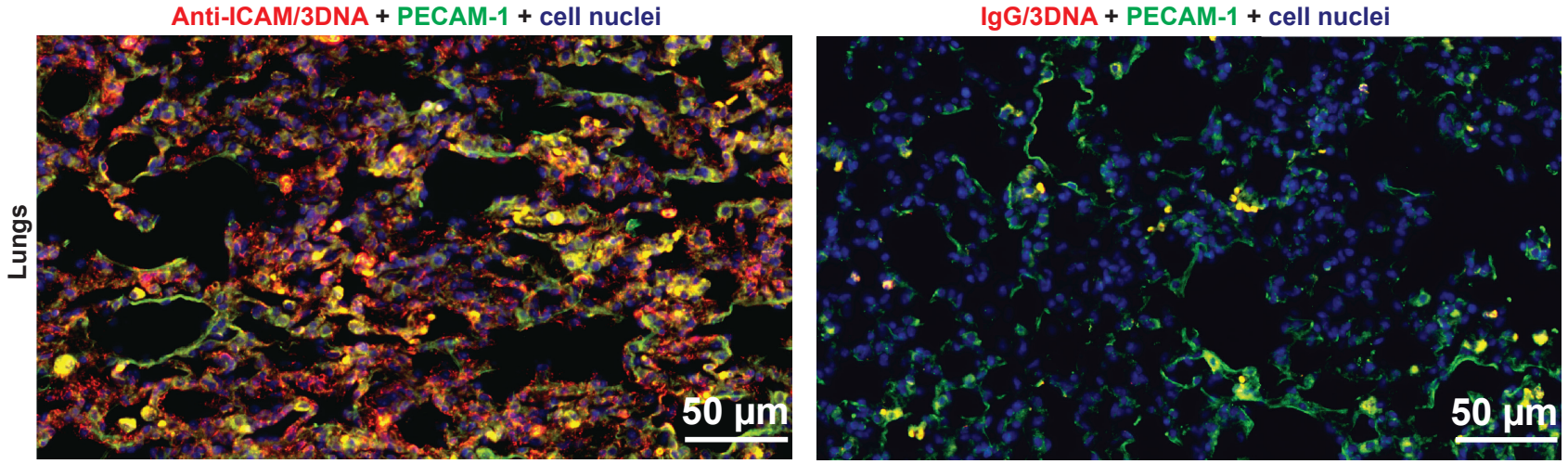

Figure 28 Visualization of anti-ICAM/3DNA in the lungs 5 min post administration.

Control IgG/Cy3-3DNA (right) or anti-ICAM/Cy3-3DNA (left) were I.V. injected in C57BL/6 mice and lungs were isolated and processed at sacrifice at 5 min. Fluorescence microscopy showing colocalization of Cy3-3DNA (red), and endothelial cells visualized using polyclonal anti-PECAM-1 + FITC-secondary Ab (green). Yellow color indicates colocalization of cy3-3DNA with PECAM-1. Cell nuclei were stained blue with DAPI. 50 µm scale bar is shown. Dr. Solomon helped with this experiment as described in the text.

6.2.6. Comparison of Anti-ICAM/3DNA and Anti-ICAM/PLGA Nanoparticles Regarding their *In Vivo* Biodistribution

In retrospect, comparing these results to those previously published for various other anti-ICAM NPs, it appears the anti-ICAM/3DNA formulation surpassed previous ones in terms of lung-to-blood distribution and specific targeting: e.g., lung LR for anti-ICAM polystyrene NPs reported by Papademetriou et al.[241] was 32 and SI against IgG/polystyrene NPs was 18, while here these values were much greater (as described above). Although Ab-NP formulations reported by Papademetriou et al.[241] are not built from Ab-DNA and had not been matched side-by-side with Ab/3DNA in terms of targeting valency (the number of Abs on the coat), the reported formulations had similar size, PDI, and ζ- potential as Ab/3DNA. Nevertheless, to verify the enhanced targeting of 3DNA designs more accurately, we prepared Ab/PLGA NPs and 3DNA counterparts with matching parameters. As expected (Section 6.2.2, **Table 3**), PLGA NPs had increased average diameter and PDI upon coating with Abs (from 155 nm to ≈200 nm, and from 0.07 to ≈0.2 PDI) and less negative ζ-potential (from −59 mV to ≈−35 mV). In addition, coating PLGA NPs with anti-ICAM or control IgG resulted in formulations with similar parameters: 208 vs. 196 nm, 0.17 vs. 0.22 PDI, and −32 vs. −37 mV. These values were similar to those observed for 3DNA counterparts; e.g., ≈180 nm, ≈0.2 PDI, and ≈−40 mV for Ab/3DNA. Importantly, both 3DNA and PLGA

displayed similar number of targeting Abs: 78.6 ± 5.6 and 88.6 ± 0.3 Ab molecules per particle, respectively.

Then, biodistribution of Ab/PLGA formulations was tested *in vivo*. Because the lungs, liver, and spleen represented the organs which received the highest %ID of anti-ICAM/3DNA (**Figure 24A**), we focused on these organs. Direct comparison of 3DNA and PLGA formulations (**Figure 29A**) showed anti-ICAM/PLGA disappeared from the circulation similarly as fast as anti-ICAM/3DNA (e.g., 3.9% and 2.6% ID by 60 min). Accumulation of anti-ICAM/PLGA in the intended target, the lungs, was 3.5% ID (**Figure 30A**) and 28.3% ID/g (**Figure 29B**), which was specific over control IgG/PLGA (e.g., SI was 4.6-fold; **Figure 30B**). While specific, the lung accumulation of anti-ICAM/PLGA was markedly lower than that of anti-ICAM/3DNA (6.0-fold and 5.6-fold lower comparing % ID and %ID/g, respectively). In addition, anti-ICAM/PLGA showed increased liver and spleen accumulation over anti-ICAM/3DNA: i.e., 2.1- and 2.5-fold increase in the %ID/g in the liver and spleen, respectively (**Figure 29B**). The tissue-to-blood LR was 9.7-fold greater for anti-ICAM/3DNA counterparts (**Figure 29C**), and the ratio of lung-to-liver LR (not shown) was 11.6-fold higher for anti-ICAM/3DNA, which was 144-fold more specific in targeting the lungs than anti-ICAM/PLGA (compare SI in **Figure 30B**).

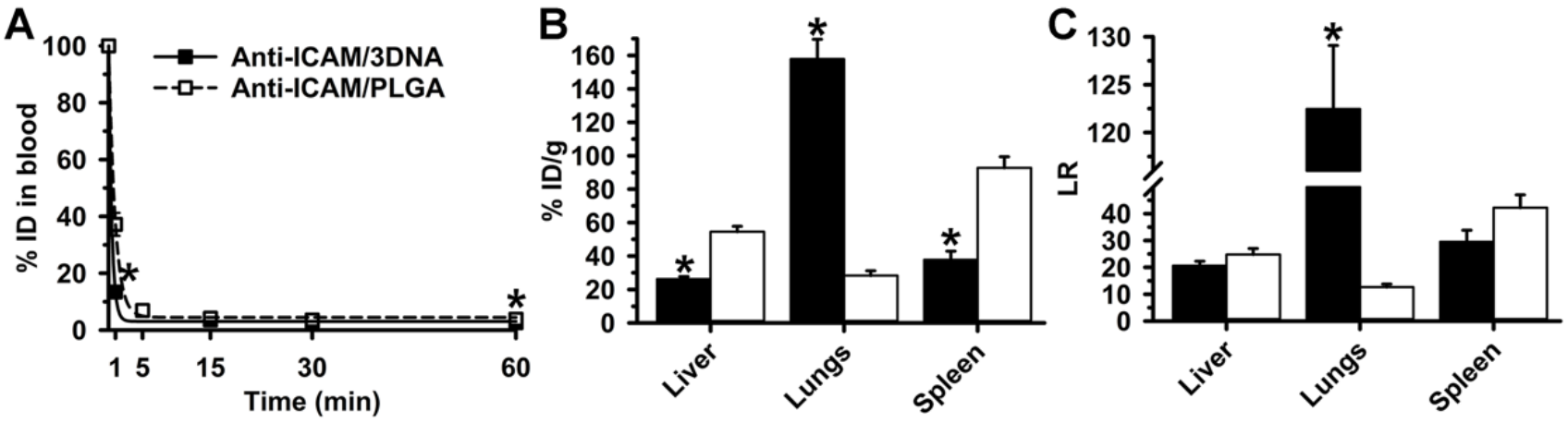

Figure 29. Comparative *in vivo* biodistribution of anti-ICAM/3DNA vs. anti-ICAM/PLGA formulations.

^{125}I-anti-ICAM/3DNA or ^{125}I-anti-ICAM/PLGA I.V. injected in C5BL/6 mice. (A) Circulation was calculated at the indicated times between injection and at sacrifice at 60 min, as the percentage of the injected dose (% ID). (B) Organ biodistribution at sacrifice was calculated as % ID per gram (%ID/g) to compare organs of different weight. (C) Organ-to-blood distribution expressed as the localization ratio (LR), was calculated as % ID/g in an organ divided by % ID/g in blood. Data are mean ± S.E.M. *$p < 0.05$ by Student's t-test.

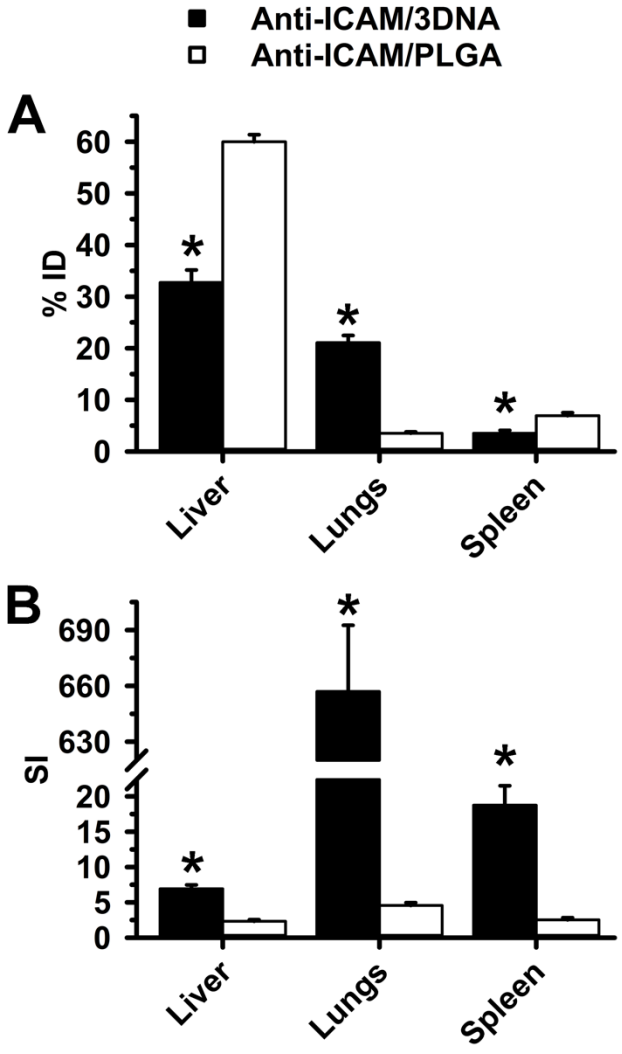

Figure 30. Comparative *in vivo* biodistribution of anti-ICAM/3DNA vs. anti-ICAM/PLGA formulations.

^{125}I-anti-ICAM/3DNA or ^{125}I-anti-ICAM/PLGA I.V. injected in C5Bl/6 mice. (A) Organ distribution at sacrifice (60 min) was expressed as the percentage of the injected dose (% ID). (B) Specificity index (SI) represents the tissue-over-blood accumulation for the targeted vs. the non-targeted formulation (see Materials and Methods). Data are mean ± S.E.M. * $p < 0.05$ by Student's t-test.

This difference in targeting capacity between Ab/3DNA NC and other polymeric NPs was unexpected *a priori* and could be due to several differences in the design. These differences stem from the: 1) difference in Ab modification and mechanisms of coupling to the NPs, 2) differences in the control and topography of the Ab presentation, 3) differences in the core of the NPs. The first two points may alter the binding ability of Abs on the NPs. Although this could be due to the detachment of Abs adsorbed on the PLGA surface upon injection, our previous work has shown surface adsorption on particles, just as in ELISA applications, is relatively stable: no > 10–15% of the Ab coat detaches upon incubation with serum.[100,266] Another possibility is that adsorption restricts movement of the Abs on the NP surface, but also induces conformational changes that could affect Ab binding.[166] On the other hand, conjugation of oligos and linkers onto the Abs could also change the Ab properties, but also modulate their availability for binding.[128] The difference could also come from the 3D topography and uniformity of the Ab presentation, as well as Ab presentation dynamics, whereby 3DNA is organized into the branches that may result in highly dynamic surface, while PLGA conforms into random coils that may result in the "solid" surface that is less dynamic. Aside from the possibility that the surface properties may influence targeting via Abs, they can also influence their interactions with scavenger receptors and the inherent immunogenicity. Lastly, these surface properties are propagated from the cores of these particles; the 3DNA configuration may be structurally more flexible than PLGA NPs. This can affect their transport in blood, but

also binding kinetics and the stability of Ab binding to the targeted marker (ICAM-1) on the endothelial surface, resulting in higher *in vivo* accumulation in target organs (e.g., the lungs). Future studies will examine whether conjugation of anti-ICAM on PLGA NPs with appropriate spacers, for a more accurate comparison, may render this formulation to be more specific and similar to the anti-ICAM/3DNA formulation.

6.3. Conclusion

DNA-built nanostructures are showing promise in the realm of targeted drug delivery, yet the behavior of these systems *in vivo* is still poorly characterized due to their relative novelty. In this study, we investigated an Ab-DNA-built and highly branched carrier, anti-ICAM/3DNA. We looked at the anti-ICAM/3DNA stability in serum, and the biodistribution in mice after an I.V. injection to learn about their relevant bio-physicochemical characteristics in a translationally relevant model of pulmonary ICAM-1 targeting. Our results demonstrate that, for the similar size, PDI, ζ-potential, and number of targeting Abs, anti-ICAM/3DNA largely outperformed anti-ICAM/PLGA NPs. This was demonstrated by superior anti-ICAM/3DNA accumulation in the targeted organ, the lungs, along with reduced accumulation in clearance organs: the liver, spleen, and kidneys. To the best of our knowledge, no other Ab- and DNA-built NP has demonstrated such a high targeting specificity *in vivo*; per SI, anti-ICAM/3DNA accumulated in the lungs 424-fold over the control IgG/3DNA, despite serum proteins, degrading enzymes, and the presence of scavenger receptors

throughout the body. This demonstrated that the targeting functionality can be designed for DNA NPs, in a similar or greater capacity than for most other targeted nanomedicines. Moreover, this confirmed that the level of targeting specificity for ICAM-1-targeted NPs is remarkable compared to most other targeted nanomedicines, which highlights the fact that active targeting by affinity ligands offers a great opportunity to enhance site-specific drug delivery. Nevertheless, as in the case of ICAM-1 targeting, the selected targets need to be expressed at specific sites and need to be accessible from the bloodstream in order to enhance targeting. Whether a similar degree of specificity will be achieved for DNA-NPs by targeting other markers will need to be investigated. Furthermore, the role of opsonization and the protein corona of the Ab/3DNA will require careful examination, yet it is expected that there would be no significant difference between the opsonization of anti-ICAM/3DNA vs. the IgG/3DNA due to the similarity between their surface characteristics. Namely, specific anti-ICAM and non-specific IgG are similar molecular species and were used at the same Ab valency. In this case, the preferential anti-ICAM/3DNA distribution to the lungs is due to anti-ICAM targeting, just as what was observed for the control anti-ICAM and other anti-ICAM-targeted NPs. In addition, while these efforts are highly supportive of advancing clinical applications, future work must carefully examine the potential side effects of anti-ICAM/3DNA technology, to rationally guide its development. Nevertheless, given the high degree of versatility, flexibility, and control for anti-ICAM/3DNA design, including the use of nonimmunological DNA sequences,

this platform technology is highly attractive and holds great potential to develop into valuable therapeutic applications.

Chapter 7: *Modulating Design Parameters of ICAM-1-Targeted 3DNA Nanocarriers to Tune Pulmonary Targeting for Drug Delivery*

7.1. Introduction

In Chapter 6, we demonstrated that anti-ICAM/3DNA could provide highly specific and efficient targeting to the lungs, which was similar or better compared to other ICAM-1-targeted NP systems. In Chapter 7, we explored the role of additional anti-ICAM/3DNA properties in targeting. Apart from the selection of the target, other NP properties, including NP size,[31,68] concentration,[82,95,210] and the number of targeting ligands,[75,217,218] may modulate the delivery of anti-ICAM/3DNA as demonstrated for other NP systems.[95,127,267] Moreover, DNA-NPs are highly programmable and hold promise as precision nanomedicines. This precision may translate into improved control over the modulation of their targeting functions. However, only a few studies have examined and shown the relevance of these parameters for DNA-NPs.[75,82,21775,217,218]

3DNA represents a good model to study this topic due to its precise and modular size, as well as the number and topography of outer arms that can carry various molecules.[90,91,232] These design parameters are expected to not only influence the targeting and biodistribution of anti-ICAM/3DNA, but also influence the delivery of

intercalating or arm-linked drugs it may carry. While increasing the number of Abs that occupy 3DNA terminal arms (i.e., surface loading) may favor specific targeting, it would also reduce the number of therapeutic molecules that can be linked to the remaining arms. On the other hand, tuning the targeting valency would not affect the inner loading of a drug, but may still influence biodistribution. Furthermore, varying the size of anti-ICAM/3DNA would impact the drug carrying capacity for both locations (i.e. arm and inner loading), and may impact targeting and biodistribution. Due to the simultaneous influence from modulating all of these anti-ICAM/3DNA properties, the resulting targeting and biodistribution are difficult to predict and must be empirically examined. Hence, we explored the anti-ICAM/3DNA formulations of different sizes, targeting valency, and dose concentration to examine the simultaneous and hierarchical influence of these parameters on their biodistribution. The biodistribution data were then used to predict the influence of these parameters in the delivery of inner- vs. surface-loaded drugs (e.g., intercalating vs. arm-linked), providing valuable guidance for the future modulation of anti-ICAM/3DNA-mediated drug delivery to the lungs, a relevant target for pulmonary conditions, but also delivery to other organs for systemic treatment.

7.2. Results and Discussion

7.2.1. Role of Targeting Valency and Dose Concentration on the Biodistribution of 4-Layer Anti-ICAM/3DNA

Moving forward with evaluating anti-ICAM/3DNA targeting properties, we first examined the effect of the targeting valency on the biodistribution of 4L anti-ICAM/3DNA administered via the I.V. route. To obtain specific anti-ICAM/3DNA targeting valencies, 3DNA was mixed at various molar ratios with the anti-ICAM-oligo (Ab-oligo) conjugate whose sequence is complementary to the 3DNA outer arms, as explained in Materials and Methods Section. The prepared anti-ICAM/3DNA formulations had 80, 46, 13, or 0 anti-ICAM molecules per NC; this amounted to targeting density of 879, 506, 143, or 0 anti-ICAM/μm^2 of 3DNA surface (**Table 5**). To clarify, non-specific IgG/3DNA control (505.5 IgG/μm^2 of 3DNA surface) was used as the anti-ICAM/3DNA targeting valency 0 (i.e., 0 anti-ICAM molecules per NC). These formulations showed similar mean hydrodynamic diameter (160-197 nm average diameter), polydispersity index (PDI 0.18-0.25), and ζ-potential (-39 to -45 mV). The change in the size and ζ-potential for the Ab/3DNA as compared to control 3DNA without Ab-oligo conjugates (170 nm and −19 mV, respectively), indicated successful modification of 3DNA surface with Ab-oligo.

Table 5. Characterization of anti-ICAM/3DNA and control formulations.

Formulation	Targeting Ab Valency (Ab/NC)	Targeting Ab Density (Ab/ μm^2)	Mean diameter (nm)	PDI	ζ-potential (mV)
4L 3DNA					
No Ab	N/A	N/A	170.4±7.5	0.22	-19.1±0.6
IgG control[(i)]	0	0	181.2±5.1	0.23	-42.7±0.5
Anti-$ICAM_1$	13	142.8	160.0±3.5	0.18	-39.1±0.8
Anti-$ICAM_2$	46	505.5	179.5±5.7	0.25	-43.6±0.1
Anti-$ICAM_3$	80	879.1	196.6±3.5	0.20	-45.0±0.1
2L 3DNA					
No Ab	N/A	N/A	84.5±12.1	0.25	-19.24±1.2
IgG control[(ii)]	0	0	114.4±3.1	0.34	-38.6±2.1
Anti-$ICAM_1$	6	545.5	113.0±4.4	0.35	-36.9±1.8
Anti-$ICAM_2$	14	1272.7	120.4±3.0	0.29	-35.3±0.3

Ab = antibody; NC = nanocarrier; PDI = polydispersity index. Data are mean ± S.E.M.

(i) 4L IgG/3DNA control contained 0 anti-ICAM molecules (targeting valency 0) and 46 IgG molecules/NC (505.5 Ab/μm^2).

(ii) 2L IgG/3DNA control contained 0 anti-ICAM molecules (targeting valency 0) and 6 IgG molecules/NC (545.5 Ab/μm^2).

As shown in **Table 6**, all the anti-ICAM/3DNA formulations redistributed rapidly from the bloodstream upon their I.V. administration in anesthetized mice. Nevertheless, anti-ICAM/3DNA formulations with higher valencies were removed faster from the bloodstream: e.g., formulations with valency 13, 46, and 80 Abs/NP had 22, 18, and 11 percent of the injected dose (%ID) remaining in the blood at 1 min after administration, respectively. Blood levels of anti-ICAM/3DNA were then lowered even further to 3.1-4.0 %ID for all targeted formulations by 5 min, after which no main changes occurred. In contrast to targeted formulations, the control IgG/3DNA (targeting valency 0) had a higher blood level (29 %ID vs. 2-3 %ID for any anti-ICAM/3DNA at 60 min; **Table 6**).

Table 6. Blood distribution for anti-ICAM/3DNA and control formulations.

Formulation	% ID in Blood				
	1 min	5 min	15 min	30 min	60 min
4L 3DNA					
No Ab	53.3±1.9	4.7±0.7	14.3±0.7	2.2±0.2	7.3±2.1
IgG control$_{(i)}^{21.5}$	41.9±2.9	17.2±0.4	31.2±1.4	23.5±1.0	28.6±2.2
Anti-ICAM$_{13}^{21.5}$	21.8±1.9	3.1±0.1	1.7±0.3	2.4±0.1	2.3±0.2
Anti-ICAM$_{46}^{21.5}$	17.6±2.9	4.0±0.3	2.7±0.6	3.3±0.4	3.0±0.2
Anti-ICAM$_{80}^{21.5}$	11.2±1.0	3.6±0.1	4.3±0.3	3.4±0.5	2.5±0.2
Anti-ICAM$_{80}^{12.9}$	13.4±1.5	ND	3.5±0.3	3.1±0.4	2.6±0.1
Anti-ICAM$_{80}^{2.2}$	20.7±4.3	5.3±0.8	3.3±0.6	2.6±0.5	2.7±0.3
2L 3DNA					
No Ab	57.8±7.0	28.5±2.6	12.4±1.3	ND	8.2±0.6
IgG control$_{(ii)}^{194}$	55.3±1.9	33.8±0.9	30.6±2.1	ND	34.2±1.4
Anti-ICAM$_{6}^{194}$	31.2±2.9	4.7±0.9	4.2±0.6	3.1±0.3	2.5±0.3
Anti-ICAM$_{14}^{194}$	18.1±2.5	6.1±0.3	4.5±0.2	4.0±0.3	3.8±0.1
Anti-ICAM$_{14}^{19.4}$	25.0±4.1	4.5±0.9	2.7±0.0	2.8±0.5	2.2±0.3

Ab = antibody; % ID = percentage of the injected dose; ND = not determined. Data are mean ± S.E.M.

*The subscript on the Ab name represent the targeting valency (Ab molecules per NC) shown in **Table 5**.*

The superscript is the dose concentration (number of NCs per kg of BW). All values must be multiplied by 10^{12}.

(i) 4L IgG/3DNA control contained 0 anti-ICAM molecules (targeting valency 0) and 46 IgG molecules/NC.

(ii) 2L IgG/3DNA control contained 0 anti-ICAM molecules (targeting valency 0) and 6 IgG molecules/NC.

The observed kinetic profile differences, which were caused by the increase in formulation valency, may be explained by faster targeting to ICAM-1 on the surface of

blood vessels. The similar concept was demonstrated in the Chapter 6, where fast removal from the bloodstream was due to the targeting to the lungs and other organs. Indeed, at 60 min post administration, we observed the trend that increasing the valency of anti-ICAM/3DNA led to the higher lung targeting (**Figure 31A**): 113, 124, 138 %ID per gram of tissue (%ID/g, a concentration-like parameter to compare among organs of very different mass within the same animal or animals with the same organ masses) for valency 13, 46, and 80 formulations. The lung targeting for all the anti-ICAM/3DNA formulations was specific compared to control IgG/3DNA (targeting valency 0), which only had 3 %ID/g in the lungs. In contrast, increasing the targeting valency of anti-ICAM/3DNA resulted in lower concentrations in the clearance organs, liver and spleen: from 39 to 29 %ID/g and from 65 to 39 %ID/g, respectively; (**Figure 31A**). This may be explained by the redistribution of anti-ICAM/3DNA targeting to the lungs. Interestingly, the comparison with IgG/3DNA formulation showed that spleen biodistribution of the anti-ICAM/3DNA formulations (all valencies) was contributed in part by ICAM-1 targeting (24 vs. 39-65 %ID/g for IgG/3DNA), though increasing valency lowered spleen levels most likely due to the increased lung uptake. The level of the accumulation of the control IgG/3DNA in the spleen (24 %ID/g) may indicate the approximate contribution of the anti-ICAM/3DNA accumulation in the spleen which is due to the clearance mechanisms, indicating a combination of targeting and clearance for the anti-ICAM/3DNA in this organ. Moreover, the reduction in spleen targeting with the increased anti-ICAM/3DNA valency indicates that spleen targeting

may be either a direct function of valency or may be a function of a first-pass lung targeting, and therefore, indirectly a function of valency. However, ICAM-1 targeting was not apparent in the liver (47 vs. 39 %ID/g for IgG/3DNA), despite this organ being reported to have a considerable ICAM-1 content.[99,268] Furthermore, the heart and kidneys received increasing levels of targeted formulations with increasing valencies. This was expected since ICAM-1 is expressed on the endothelium in these organs.[99] Notably, the kidneys are a filtration organ for smaller objects and degradation fragments, and may contain some degradation products that are being filtered to the bladder. Moreover, although anti-ICAM/3DNA levels in heart and kidneys were much lower than in the lungs, liver and spleen (4 and 9 %ID/g for the heart and kidneys at the highest targeting valency; **Figure 31A**), these organs had 117 and 155 % increase in the %ID/g delivery for the highest targeting valency compared to the lowest targeting valency, while the lungs had 22% increase in the %ID/g delivery for the same comparison. The %ID in organs[n] for all the tested formulations is shown in the **Table 7**.

---

[n] Note that the %ID in organs does not account for the different organ weights in each animal, and unlike the %ID/g, it can be used to compare the same organs of different sized animals, provided they have the same anatomy and physiology.

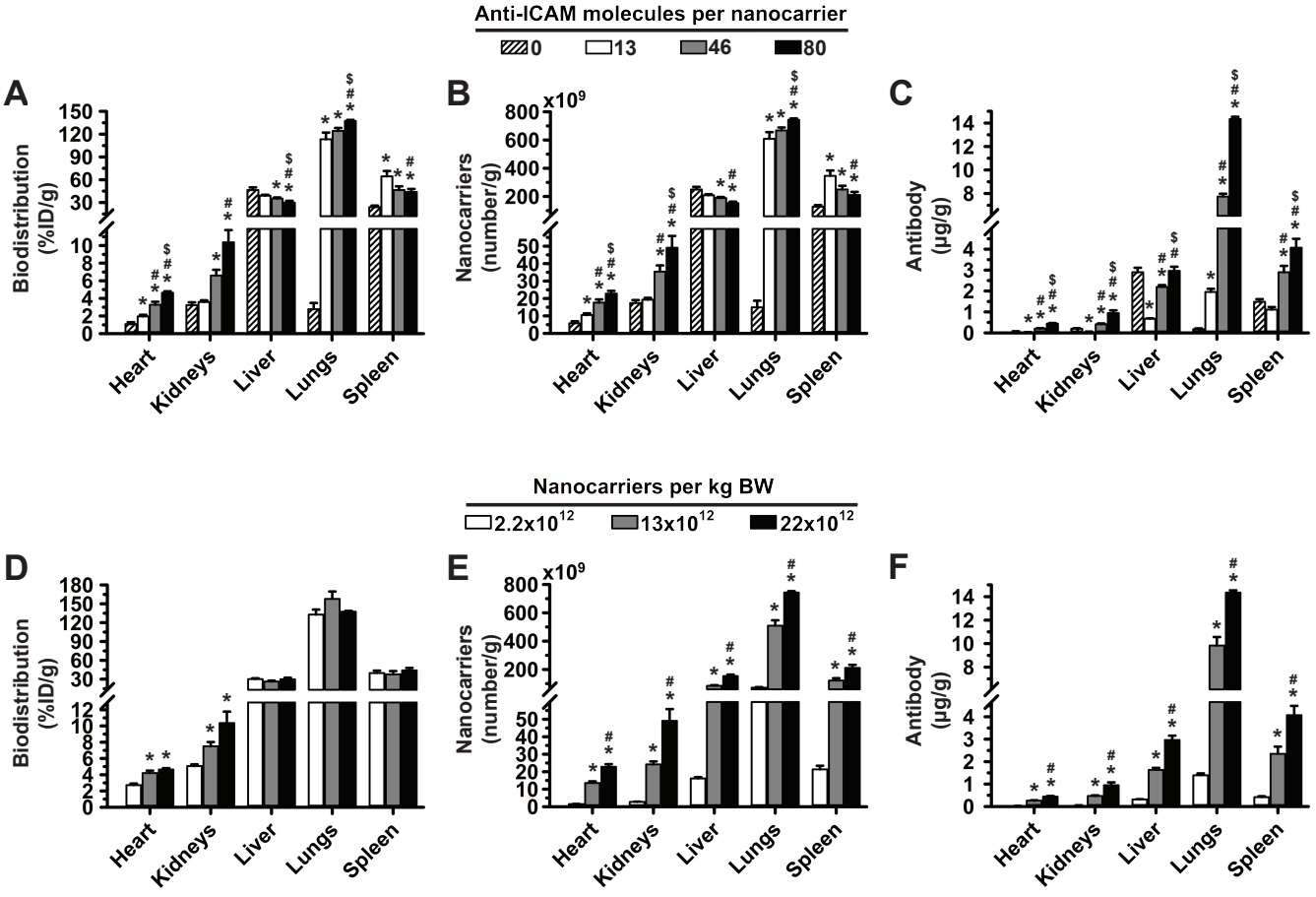

Figure 31. Role of targeting valency and dose concentration in the biodistribution of 4L anti-ICAM/3DNA.

(A, B, C) Mice were injected with 4L ^{125}I-anti-ICAM/3DNA bearing different targeting valencies (valency 0 = IgG/3DNA control), or (D, E, F) at different dose concentrations. Radioactive content and weight of the organs were determined at 60 min to calculate: (A, D) % injected dose per gram of organ (% ID/g); (B, E) the number of NCs per gram of organ; and (C, F) the Ab mass per gram of organ. Data are mean ± S.E.M. * Compares each condition with the condition of lowest parametric value, # compares remaining conditions with the condition of second lowest parametric value, $ compares remaining conditions with the condition of third lowest parametric value; ($n \geq 3$; $p < 0.05$ by Student's t-test).

Table 7. Organ distribution for anti-ICAM/3DNA and control formulations.

Formulation	% ID in Organ					
	Brain	Heart	Kidneys	Liver	Lungs	Spleen
4L 3DNA						
No Ab	0.2±0.1	0.2±0.0	3.2±0.7	20.8±1.3	0.5±0.1	1.0±0.1
IgG control$_{(i)}^{21.5}$	0.2±0.0	0.1±0.0	1.1±0.1	50.2±2.0	0.4±0.1	2.2±0.1
Anti-ICAM$_{13}^{21.5}$	0.1±0.0	0.2±0.0	1.3±0.1	45.8±1.3	14.5±1.1	4.7±0.4
Anti-ICAM$_{46}^{21.5}$	0.1±0.0	0.4±0.0	2.6±0.3	40.2±1.7	18±1.0	3.5±0.3
Anti-ICAM$_{80}^{21.5}$	0.2±0.0	0.5±0.0	3.2±0.3	35.5±0.8	18.6±0.5	3.0±0.2
Anti-ICAM$_{80}^{12.9}$	0.2±0.0	0.5±0.0	2.8±0.2	32.7±2.4	21.1±1.4	3.5±0.6
Anti-ICAM$_{80}^{2.2}$	0.1±0.0	0.3±0.0	1.9±0.0	39.2±1.1	18.4±0.8	3.6±0.3
2L 3DNA						
No Ab	0.1±0.0	0.2±0.0	2.4±0.2	20.6±1.1	0.5±0.1	1.3±0.1
IgG control$_{(ii)}^{194}$	0.3±0.0	0.2±0.1	1.6±0.2	46.2±1.2	0.6±0.0	1.8±0.2
Anti-ICAM$_{6}^{194}$	0.1±0.0	0.4±0.0	2.2±0.1	37.5±1.1	18.4±0.7	4.6±0.2
Anti-ICAM$_{14}^{194}$	0.2±0.0	0.5±0.0	4.3±0.2	39.2±2.3	13±0.3	3.5±0.1
Anti-ICAM$_{14}^{19.4}$	0.1±0.0	0.3±0.0	1.9±0.1	34.3±2.3	19.6±1.3	3.3±0.6

Ab = antibody; % ID = percentage of the injected dose; ND = not determined. Data are mean ± S.E.M.

*The subscript on the Ab name represent the targeting valency (Ab molecules per NC) shown in **Table 5**.*

The superscript is the dose concentration (number of NCs per kg of BW). All values must be multiplied by 10^{12}.

(i) 4L IgG/3DNA control contained 0 anti-ICAM molecules (targeting valency 0) and 46 IgG molecules/NC.

(ii) 2L IgG/3DNA control contained 0 anti-ICAM molecules (targeting valency 0) and 6 IgG molecules/NC.

Next, we looked at the additional performance metrics for the valency and dose response: the concentration of anti-ICAM/3DNA (i.e., NC component) and the concentration of the Ab component of the anti-ICAM/3DNA, both shown per gram of

organ. As expected from the %ID/g analysis, increasing the targeting valency of anti-ICAM/3DNA increased the concentration of the NC component in the lungs, while decreasing it in the liver and spleen (**Figure 31B**). The change in the lung delivery was not large at the tested conditions ($6x10^{11}$-$7x10^{11}$ NCs/g), which amounted to 22% increase in lung delivery as already mentioned. Increasing the targeting valency more acutely affected the concentration of the Ab component in the lungs: from 2 to 14 μg of Ab/g, which amounted to 634% increase (**Figure 31C**). Unlike the NC concentration, which decreased in the liver and spleen with increasing valency, anti-ICAM concentration increased in these organs by 342% and 266%, respectively. This can be explained as increasing valency from 13 to 80 only modestly reduced the %ID/g in these clearance organs (**Figure 31A**), yet each NC carried a very different number of anti-ICAM molecules (from 13 to 80). In addition, the delivery of anti-ICAM was increased by 1207 and 1432% in the heart and kidneys, respectively.

Next, we explored the role of the concentration (referred to as dose concentration) of anti-ICAM/3DNA injected I.V. in mice. For these experiments, the concentration of the anti-ICAM/3DNA was varied, while keeping the injection volume constant. Increasing the dose concentration from $2.2x10^{12}$ to $1.3x10^{13}$ and to $2.2x10^{13}$ NCs/kg of BW affected the circulating levels, e.g., 20.7 vs. 11.2 %ID for the lowest and highest dose at 1 min after injection (**Table 6**). Yet, by 5 min no differences were observed (3.6-5.3 %ID), suggesting that targeting may have been achieved, as demonstrated in Chapter 6. We next looked at the organ biodistribution. Varying the

dose concentration did not impact the proportion of the injected dose reached per gram of lung (**Figure 31D**), neither did it impact the clearance organs, liver and spleen. Nevertheless, increasing the dose concentration enhanced the concentration of both NCs and Ab reaching the lungs by 941% (from $7x10^{10}$ to $7x10^{11}$ NCs/g and from 1 to 14 Ab/g; **Figure 31E and F**). This also enhanced the NC and Ab concentration in the liver and spleen (e.g., from 0.3 to 3 and 0.4 to 4 Ab/g, respectively). In addition, increasing the dose concentration enhanced the proportion of the injected dose reached per gram of the brain (not shown), heart, and kidneys by 33, 57, and 80%, respectively.

In summary, increasing the targeting valency of anti-ICAM/3DNA increased biodistribution to the lungs (target) and decreased biodistribution to the liver and spleen (off-target) based on the %ID/g (**Figure 31A**), while varying the dose concentration (**Figure 31D**) did not seem to change biodistribution in a similar manner under the tested conditions. Therefore, compared to dose concentration, changing targeting valency seemed advantageous for lung specificity and modulation of biodistribution. Nevertheless, NC concentration found in organs revealed that changing the dose concentration was advantageous for this measurement compared to targeting valency as it greatly impacted delivery to lungs, but also the other organs (**Figure 31B** vs. **E**). On the other hand, the Ab concentration (**Figure 31C** vs. **F**) revealed a similar trend of increased delivery to all the organs, regardless of whether targeting valency or dose concentration were increased. Hence, when increasing the targeting valency or dose concentration one must consider whether the increase in formulation uptake by the

target organ, the lungs, compensates for the higher liver-spleen uptake of the Ab component. Depending on the application intended, these adjustments may cause side effects in clearance organs (e.g., if anti-ICAM would prevent the positive influence of ICAM-1 in certain conditions) or beneficial effects (e.g., if anti-ICAM would block the negative influence of ICAM-1 in other conditions), as both are possible based on literature.[268,269]

7.2.2. Role of Targeting Valency and Dose Concentration of 4-Layer Anti-ICAM/3DNA for Intercalating vs. Arm-Linked Drugs

Next, we estimated how the biodistribution of anti-ICAM/3DNA would impact the biodistribution of drugs that 3DNA can potentially carry within the 3DNA construct or on the surface of 3DNA. We assumed the absence of degradation, the absence of premature release, and no effects on the biodistribution due to the presence of the drugs. As described in the Background section, loading of an intercalating drug in 3DNA (inner loading) depends on the DNA content. Genisphere® LLC estimates a loading capacity of 550 doxorubicin molecules per 2L 3DNA and 4950 doxorubicin molecules per 4L 3DNA (unpublished). Hence, we used this factor to plot the biodistribution of an intercalating drug, expressed as the number of effective intercalation sites per gram of tissue (**Figure 32A**). On the other hand, loading of an arm-linked drugs (surface loading) depends on the number of 3DNA arms available for coupling (not occupied with targeting Ab) with absolute efficiency of oligo annealing using substoichiometric

ratios. Thus, we used this factor to plot the biodistribution of an arm-linked drug (**Figure 32B**). As expected, increasing the targeting valency of anti-ICAM/3DNA enhanced lung concentration of drug-intercalating sites and decreased that in the liver and spleen (**Figure 32A**). However, increasing the targeting valency of anti-ICAM/3DNA resulted in a decrease in the concentration of free arms available for drug loading in the lungs, liver and spleen (**Figure 32B**), suggesting that the targeting/non-targeting gain obtained from increasing valency within this range may not compensate for the loss of NC arms available for drug coupling. In contrast, increasing the concentration of anti-ICAM/3DNA in the injected dose enhanced the concentration of both drug-intercalating sites and drug-coupling arms in the lungs, liver, and spleen (**Figure 32C-D**). Furthermore, increasing the dose concentration caused the 941% increase in lung delivery of both drug types, while modulation of the targeting valency resulted in 22% increase in lung delivery of drug-intercalating sites and 8% decrease of drug-coupling arms. Therefore, within the range tested, the advantage of increasing anti-ICAM/3DNA valency seems more valuable for lung delivery of intercalating compared to arm-linked drugs, while increasing the dose concentration impacts both drug types similarly and with greater impact on total drug delivery as compared to the valency response.

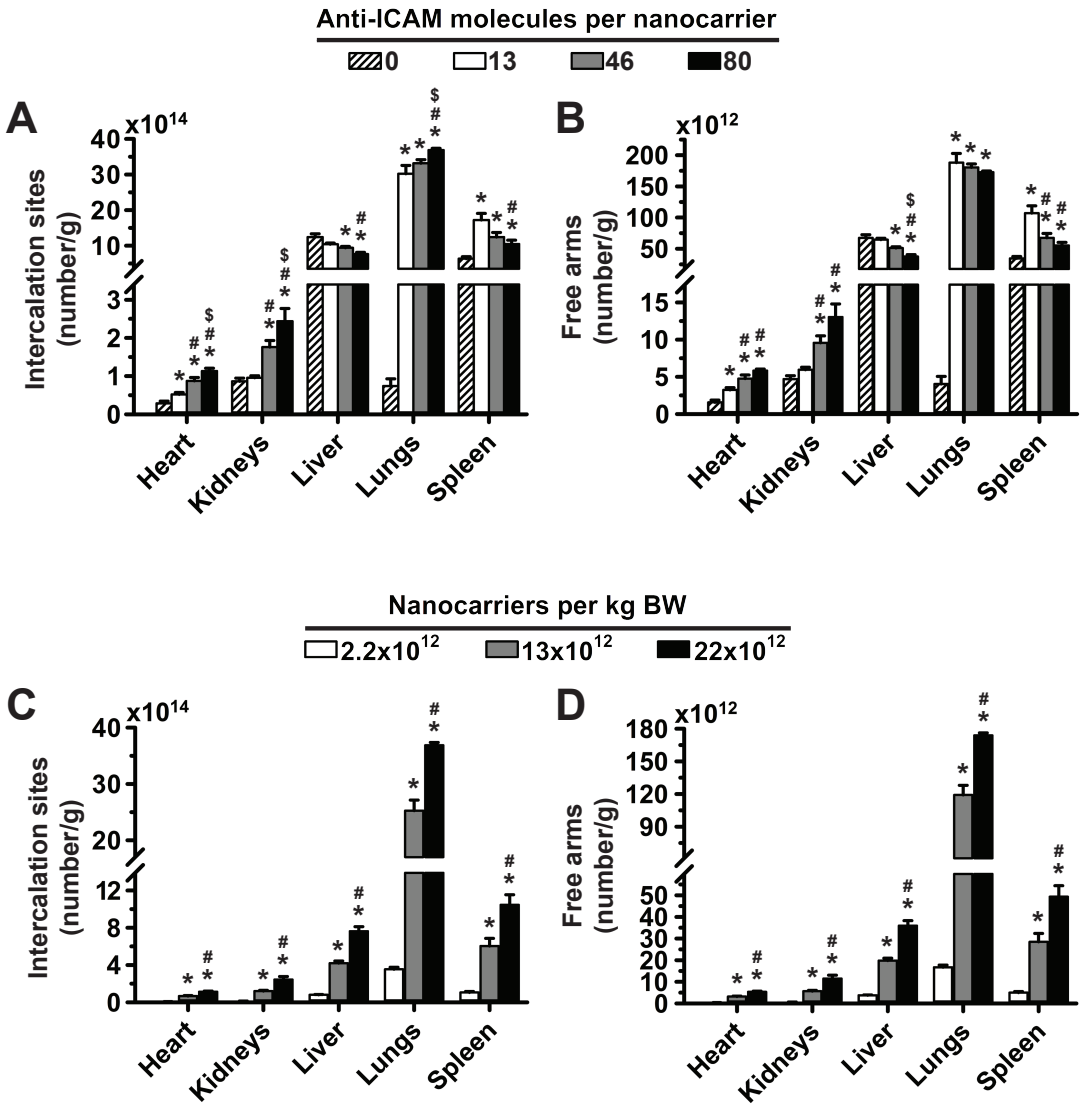

Figure 32. Effect of 4L anti-ICAM/3DNA targeting valency and dose concentration on the potential biodistribution of intercalating and arm-coupling drugs.

4L ^{125}I-anti-ICAM/3DNA were I.V. injected in C57BL/6 mice at (A, B) different targeting valencies, or (C, D) different dose concentrations. Organs radioactive content and weight were determined at 60 min to calculate: (A, C) the number of DNA drug-intercalating sites per gram of organ; and (B, D) the number of outer arms free for drug coupling per gram of organ. Data are mean ± S.E.M. * Compares each condition with the condition of lowest parametric value, # compares remaining conditions with the condition of second lowest parametric value, $ compares remaining conditions with the condition of third lowest parametric value; ($n \geq 3$; $p < 0.05$ by Student's t-test).

7.2.3. Role of Targeting Valency and Dose Concentration on the Biodistribution of 2-Layer Anti-ICAM/3DNA

In order to verify that the valency and dose findings are applicable across different formulation sizes, we focused on evaluating the valency and dose responses for the smaller 2L 3DNA formulations. First, as shown in (**Table 5**), we characterized the 2L formulations similarly as for the 4L. Coupling IgG or anti-ICAM to 2L 3DNA increased the mean hydrodynamic diameter from 85 nm (uncoated 3DNA) to 120 nm and changed the ζ-potential from -19 to -39, while the PDI stayed similar at ~0.3. Before testing the valency and dose responses of 2L anti-ICAM/3DNA, we first verified lung targeting as we did for the 4L counterparts in the Chapter 6. As for the 4L, the 2L anti-ICAM/3DNA was removed fast from the bloodstream (**Figure 33A**): only 31 %ID was found in blood by 1 min vs. 55.3 and 57.8 % ID observed for IgG/3DNA or 3DNA, and by 5 min the respective blood biodistributions were 5, 33.8, and 22.8 %ID. This slightly higher blood level for the 2L formulations as compared to 4L formulations (**Table 6**) seemed due to size-related properties, since it was observed for both anti-ICAM/3DNA and IgG/3DNA. Nevertheless, the lower blood level for targeted vs. untargeted counterparts followed the 4L trend, which is likely due to fast lung targeting as already seen for the 4L. Indeed, by 60 min, 2L anti-ICAM/3DNA rendered 147 %ID/g in the lungs, which was specific compared to the IgG/3DNA or 3DNA controls: 5 and 4 %ID/g, respectively (**Figure 33B**). The liver and spleen biodistribution of 2L anti-ICAM/3DNA were 34 and 70 %ID/g, respectively. The 2L

anti-ICAM/3DNA also had lower blood levels and higher lung distribution compared to its Ab alone (not shown), which is expected due to the role of size in clearance and increased avidity of multivalent NCs.[110] The specificity index of 2L anti-ICAM/3DNA, which takes into account the tissue-over-circulation levels for the targeted-over-untargeted formulations (see Materials and Methods Section) was 501 or 129 for anti-ICAM/3DNA over IgG/3DNA or 3DNA (**Figure 33C**), similar to values reported for 4L counterparts.[110] In addition, targeting in the lungs was verified by fluorescence microscopy, which indicated a high accumulation of 2L anti-ICAM/3DNA in the lungs, but not IgG/3DNA (**Figure 33D**). Furthermore, 2L anti-ICAM/3DNA colocalized with PECAM-1-positive endothelium. This result was similar to the 4L counterparts (Chapter 6).

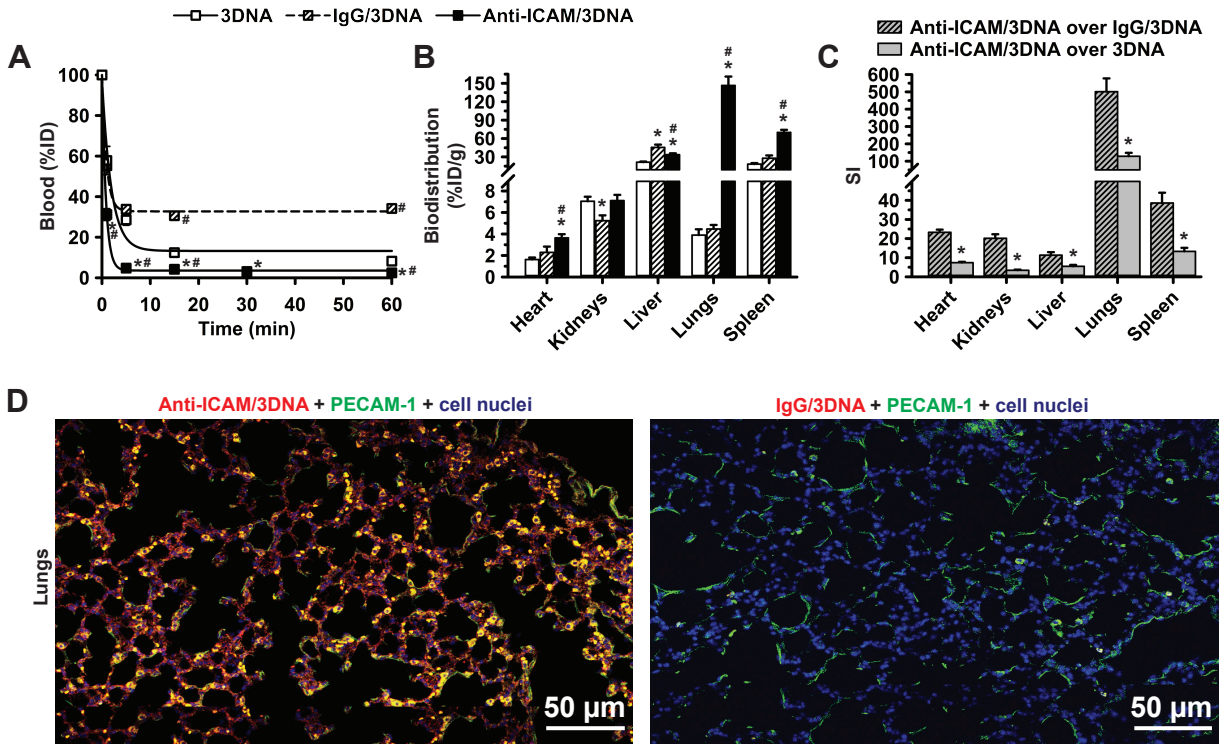

Figure 33. Biodistribution of 2L anti-ICAM/3DNA.

^{125}I-anti-ICAM/3DNA, control ^{125}I-IgG/3DNA, or control ^{125}I-3DNA were I.V. injected in C57BL/6 mice. (A) Circulation was calculated at the indicated times between injection and at sacrifice at 60 min, as the percentage of the injected dose (% ID). (B) Organ biodistribution at sacrifice was calculated as % ID per gram (%ID/g) to compare organs of different weight. (C) Specificity index (SI) represents the tissue-over-blood accumulation for the targeted vs. the non-targeted formulation (see Materials and Methods). (D) Control IgG/Cy3-3DNA (right) or anti-ICAM/Cy3-3DNA (left) were I.V. injected in C57BL/6 mice and lungs were isolated and processed at sacrifice at 60 min. Fluorescence microscopy showing colocalization of Cy3-3DNA (red), and endothelial cells visualized using polyclonal anti-PECAM-1 + FITC-secondary Ab (green). Yellow color indicates colocalization of cy3-3DNA with PECAM-1. Cell nuclei were stained blue with DAPI. 50 µm scale bar is shown. Data are mean ± S.E.M. * Compares either Ab/3DNA vs. 3DNA alone; # compares anti-ICAM/3DNA vs. IgG/3DNA; ($p < 0.05$ by Student's t-test). Dr. Solomon has helped with the fluorescence imaging experiments: we worked together on the injections, animal perfusions, and imaging, and Dr. Solomon performed deparaffinization and staining of the slides, as well as image processing.

After verifying the efficient and specific targeting for 2L anti-ICAM/3DNA, we tested the valency response for the 2L anti-ICAM/3DNA. Under the tested conditions for the 2L anti-ICAM/3DNA (targeting valencies of 6 vs. 14 Ab/NC corresponding to 545.5 vs. 1272.7 Ab/μm^2 of 3DNA surface; **Table 5**), we observed that increasing valency decreased lung and spleen %ID/g by 32 and 28% without statistically significant change in the liver: from 34 to 37 %ID/g (**Figure 34A**). Nevertheless, the %ID/g increased in the brain, heart, and kidneys by 23, 21, and 84%. These biodistribution shifts for the 2L anti-ICAM/3DNA valency response was different than the ones recorded for the 4L counterparts. For example, with the increased valency, the biodistribution to lungs increased for the 4L anti-ICAM/3DNA formulations, while it decreased for the 2L anti-ICAM/3DNA formulations (**Figure 34A**). Interestingly, although kidneys increased for both 2L and 4L anti-ICAM/3DNA formulations with increasing valency, the 2L formulation increased by 84%, while 4L increased by 39% when comparing medium valency with the highest valency (please note, the 2L was not tested at the lowest valency **Table 5).** In contrast, for the same comparison, the heart had greater increase for the 4L formulation compared to the 2L formulation (39 vs 21% increase). This dynamic interplay between organ distribution and the role of different parameters is further analyzed after the next section which evaluates the modulation of drug delivery by 2L anti-ICAM/3DNA valency and dose.

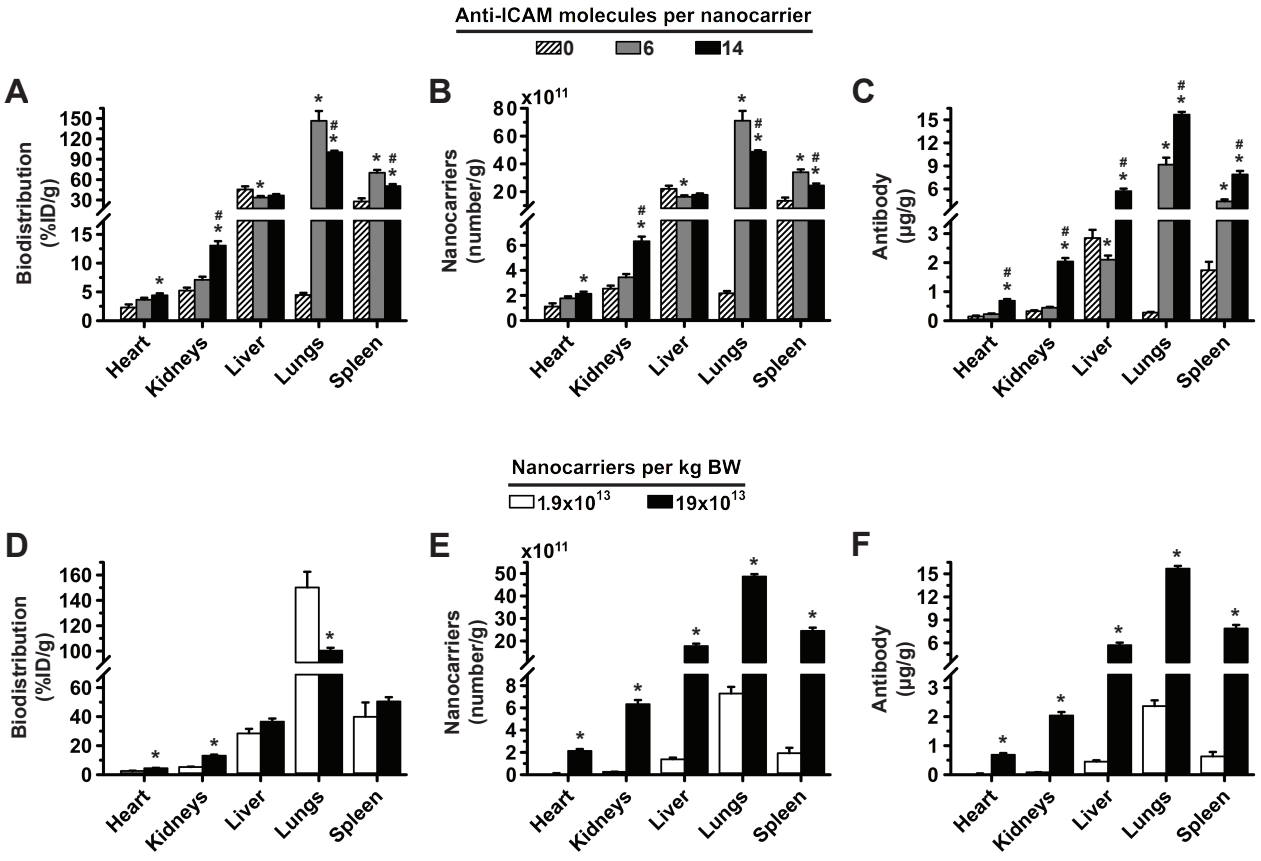

Figure 34. Role of targeting valency and dose concentration in the biodistribution of 2L anti-ICAM/3DNA.

C57BL/6 mice were I.V. injected with 2L ^{125}I-anti-ICAM/3DNA at (A, B, C) different valencies (valency 0 = IgG/3DNA control), or (D, E, F) different dose concentrations. Organs radioactive content and weight were determined at 60 min to calculate: (A, D) % injected dose per gram of organ (% ID/g); (B, E) the number of NCs per gram of organ; and (C, F) the Ab mass per gram of organ. Control ^{125}I-IgG/3DNA is represented as targeting valency 0. Data are mean ± S.E.M. * Compares each condition with the condition of lowest parametric value, # compares remaining conditions with the condition of second lowest parametric value; ($n \geq 3$; $p < 0.05$ by Student's t-test).

Next, we looked at how the valency modulated concentration of NCs in organs. As expected, the NC concentration in these organs correlated with the biodistribution results, and hence, showed similar behavior (**Figure 34B**). In contrast, the Ab concentration increased for increasing valencies in all organs (**Figure 34C**)**.** As explained for the 4L formulations, the Ab delivery results were possible since the effect of increased Ab valency and associated increased Ab delivery dominated over the effect of decreased biodistribution in all the organs (**Figure 31A-C**).

Next, we looked at the dose response of 2L anti-ICAM/3DNA biodistribution. Increasing the dose concentration of 2L anti-ICAM/3DNA from $1.9x10^{13}$ to $1.9x10^{14}$ NCs/kg BW (**Table 8**) decreased lung targeting by 33% (from 150 to 100 %ID/g), without statistically significant differences in liver and spleen distribution (**Figure 34D**). Nevertheless, the %ID/g increased in the brain, heart, and kidneys by 66, 75, and 147%. As seen with the valency response, these biodistribution shifts for the 2L anti-ICAM/3DNA dose concentration response was different than the ones recorded for the 4L counterparts. For example, with the increased dose, the biodistribution to lungs did not change for the 4L anti-ICAM/3DNA formulations, while it decreased for the 2L anti-ICAM/3DNA formulations (**Figure 34D**). This revealed that the dose concentration affected biodistribution to lungs with similar magnitude as the valency response (33% vs 32% difference, respectively for the 2L conditions, and 22% difference for the 4L valency response). Compared to valency response, the increased dose not only caused the greater increase for the 2L as compared to 4L anti-

ICAM/3DNA formulations in the kidneys: the 2L increased by 147%, while 4L increased by 80%, but also in the heart: the 2L increased by 75%, while 4L increased by 57%. As for the impact in the concentration of NCs (**Figure 34E**) and Ab (**Figure 34F**), increasing the dose concentration of 2L anti-ICAM/3DNA augmented these parameters for all organs.

Table 8. Parametric values of all anti-ICAM/3DNA injections.

Formulation	Properties & Parameters							
	Valency (Ab/NC)	Valency density (Ab/μm^2 NC)	Ab dose (μg/kg BW)	DNA dose (μg/kg BW)	Total 3DNA surface (μm^2/kg BW)	Number of NCs/kg BW	Intercalation Sites per kg BW	Free Arms per BW
4L 3DNA								
Anti-ICAM *(a)*	13	142.8	69	400	19E+11	21.5E+12	1.1E+17	6.6E+15
Anti-ICAM *(b)*	46	505.5	249	400	19E+11	21.5E+12	1.1E+17	5.8E+15
Anti-ICAM *(c)*	80	879.1	415	400	19E+11	21.5E+12	1.1E+17	5.0E+15
Anti-ICAM *(d)*	80	879.1	249	240	12E+11	12.9E+12	6.4E+16	3.0E+15
Anti-ICAM *(e)*	80	879.1	42	40	1.9E+11	2.2E+12	1.1E+16	5.0E+14
2L 3DNA								
Anti-ICAM *(a)*	6	545.5	250	400	22E+11	194E+12	1.1E+17	5.8E+15
Anti-ICAM *(b)*	14	1272.7	625	400	22E+11	194E+12	1.1E+17	4.1E+15
Anti-ICAM *(c)*	14	1272.7	63	40	2.2E+11	19.4E+12	1.1E+16	4.1E+14

Ab = antibody; BW = body weight, NC = nanocarrier.

Interestingly, we observed different behavior for 2L formulations as compared to 4L formulations regarding the impact of targeting valency and dose concentration. The trend was opposite for the lung biodistribution (compare **Figure 31A&D** to **Figure 34A&D**) and varied greatly in the direction and magnitude of the response for all the organs. This outcome may be due to NC size and its ability to access the target. Alternatively, perhaps the valency and dose operate within different parametric ranges and have different responsiveness for the anti-ICAM/3DNA of distinct sizes. To note is that under various experimental conditions that were tested, the range of lung responses was similar for both (14.5-21.1 %ID for 4L and 13.0-19.6 %ID for 2L; **Table 7**). Notably, organs which received a small fraction of the 2L formulations (i.e., organs with small blood supply and located behind the first pass capillary network of the lungs) experience enhanced accumulation with increasing valencies and dose concentrations. Nevertheless, as discussed, the magnitudes of the valency and the dose responses varied greatly for these organs for the 4L vs. 2L. Overall, this suggest that the role of valency and dose may be similar for 2L and 4L formulations, but the role may depend on complex interplay between the tested parameters and the interactions with biological environment, including the anatomical distribution of organs along the cardiovascular network in relation to administration route, expression profiles of target markers, blood flow, etc. For example, it is possible that a saturation point along the path of blood redistribution was exceeded for 2L anti-ICAM/3DNA in some organs that are preferentially supplied by the vascular system (at valency 14 and dose 1.9×10^{14} NCs/kg

BW), while the parametric ranges tested for the 4L may have been at sub-saturation levels, as suspected from the data. Saturating cell surface receptors in a concentration-dependent manner is a common finding for receptor targeted NPs, but saturation due to valency has been detected with more scarcity.[66,163] It is possible that this saturation was reached for the lungs but not the other ICAM-1-expressing organs such as the heart, due to lungs acting as a sink for targeted NPs. One reason for this is the high ICAM-1 content and/or extensive endothelial surface for binding in the lungs[99] as reflected by high lung capacity to uptake anti-ICAM/3DNA (≈20 %ID vs. 0.5 %ID for the heart; **Table 7**). Since there are other organs with high ICAM-1 content (e.g., liver), the second reason why lungs could act as a sink is that the lungs receive full cardiac output and are the first pass capillary network after I.V. injection, before any other organ can bind NPs regardless of the capacity of the organ to act as a sink. Hence, the lungs can saturate first, while further increase in targeting valency or dose concentration would be needed to saturate other organs. Since formulations have to be distributed somewhere in the body upon injection, saturation concept could be used to shift the parametric range to selectively modulate the efficiency of targeting to each organ or group of organs depending on the organ targeting selectivity in each range. Hence, the different behavior observed for 2L vs. 4L may not be due to size but rather due to different saturating capacities of the parametric values studied, further described in Section 7.2.5. Furthermore, these kinds of responses to valency, dose, and size were new, as they were never reported for other types of anti-ICAM/NPs.

7.2.4. Role of Targeting Valency and Dose Concentration of 2-Layer Anti-ICAM/3DNA for Intercalating vs. Arm-Linked Drugs

We then evaluated the modulation of drug biodistribution that 2L anti-ICAM/3DNA valency and dose variation could potentially provide. As for the 4L, we assumed the absence of degradation, premature release, and no effects on the biodistribution due to the presence of the drugs (**Figure 35**). Increasing the targeting valency resulted in decreased delivery of both intercalating sites and free arms to the lungs, liver and spleen, while increasing in the kidney. In addition, the heart delivery of intercalating sites increased. In contrast, increasing the dose concentration enhanced the delivery for both drug carrying modalities in all organs. Compared to 4L formulations, the main differences for the 2L were in the lung concentration response to valency modulation for intercalating sites, as well as the magnitude of the concentration responses among organs, most likely due to the different saturating levels among the organs in different conditions tested. For example, while the delivery to the heart was responsive for the 4L valency modulation among all the formulations, it only made the significant difference between the highest valency and the control valency 0 in the case of 2L, indicating that it is possible that even the heart was getting saturated (compare **Figure 32A** to **Figure 35A**). Hence, the decrease in NC free arm delivery was more acute for 2L formulations most likely due to the greater extent of saturation compared to 4L. Therefore, the overall role of targeting valency and dose concentration in terms of drug biodistribution by 2L and 4L anti-ICAM/3DNA may be similar in the

absence of oversaturation conditions, which will be explored in more detail in the future. Nevertheless, we made additional comparisons among 4L and 2L conditions, as described below, in order to better understand these unexpected differences in their behavior.

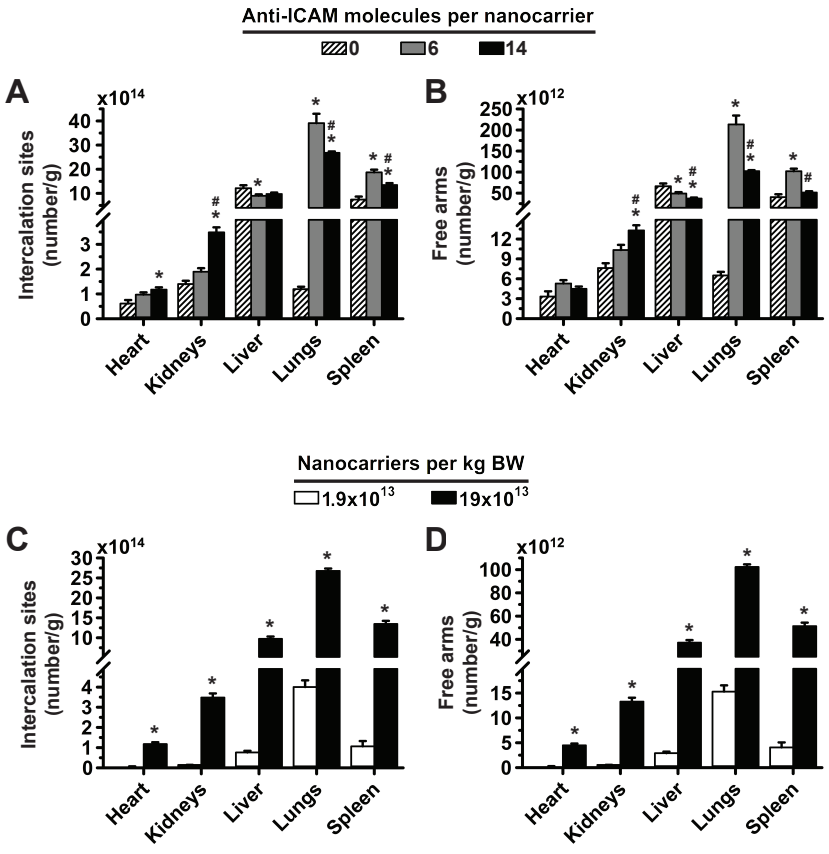

Figure 35. Effect of 2L anti-ICAM/3DNA targeting valency and dose concentration on the potential biodistribution of intercalating and arm-coupling drugs.

2L ^{125}I-anti-ICAM/3DNA were I.V. injected in C57BL/6 mice at (A, B) different targeting valencies, or (C, D) different dose concentrations. Organs radioactive content and weight were determined at 60 min to calculate: (A, C) the number of DNA drug-intercalating sites per gram of organ; and (B, D) the number of outer arms free for drug coupling per gram of organ. Data are mean ± S.E.M. * Compares each condition with the condition of lowest parametric value, # compares remaining conditions with the condition of second lowest parametric value; ($n \geq 3$; $p < 0.05$ by Student's t-test).

7.2.5. Multiparametric Comparison Regarding the Biodistribution of 2-Layer and 4-Layer Anti-ICAM/3DNA

To further understand the potential factors, that could cause differences between 2L and 4L anti-ICAM/3DNA, besides the NP size, we made comparisons where some parameters were kept constant, while changing others. For example, if the same number of NCs and same Ab surface density were used for 4L and 2L structures, then the total number of Abs per injection would vary between these formulations, or if the same number of Abs per NC were used then the Ab density on the NC surface would vary, *etc.* Accordingly, we compared 2L and 4L formulations side-by-side by varying certain parameters while fixing others (**Figure 36**).

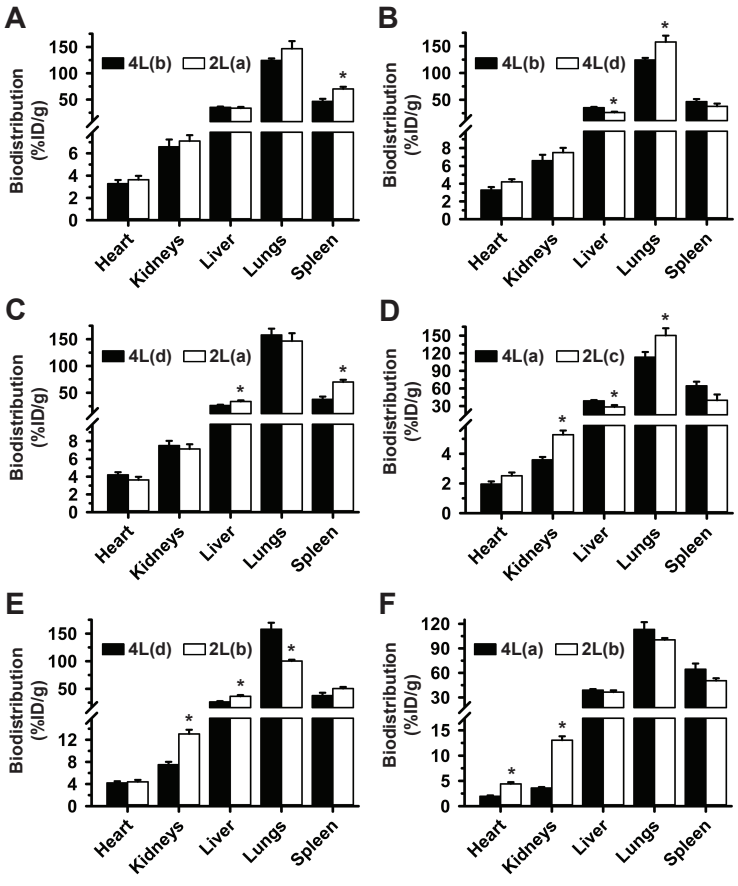

Figure 36. Multiparametric comparison between 2L and 4L anti-ICAM/3DNA biodistribution.

^{125}I-anti-ICAM/3DNA were I.V. injected in C57BL/6 mice at different sizes, targeting valencies, and/or dose concentrations, so that for each comparison certain parameters were keep similar while others changed, to infer their impact hierarchy on lung targeting and biodistribution. Organs radioactive content and weight were determined at 60 min to calculate the % injected dose per gram of organ (% ID/g). All formulations and parametric values are in Table 8. (A) Similar valency density, Ab dose, DNA dose, and total carrier surface, but different valency and number of NCs. (B) Similar Ab dose, greater valency density for 4L(d), and lower DNA dose, total carrier surface, and number of carriers for 4L(d). (C) Similar Ab dose, greater valency density for 4L, lower DNA dose, total carrier surface, and number of NCs for 4L, potentially close to a saturating condition for 4L(d). (D) Similar Ab dose, valency and number of NCs, greater valency density for 2L(c), and lower DNA dose, total carrier surface. (E) Greater valency density, Ab dose, DNA dose, total carrier surface, and number of NC for 2L(b), an oversaturating condition for 2L(b). (F) Similar valency, DNA dose and total carrier surface, although still greater Ab dose and number of NCs for 2L(b), an oversaturating condition for 2L(b). Data are mean ± S.E.M. n $\geq$ 5; * $p < 0.05$ by Student's t-test.

First, we compared valency 46 for 4L formulation to valency 6 for 2L counterpart (comparison 2L*(a)* vs. 4L*(b)* in **Table 8**), both at 400 μg DNA/kg BW dose concentration, using similar Ab per NC surface (valency density; 506-546 Ab/μm^2), similar Ab dose (250 μg/kg BW), and similar NC surface area (19-22 μm^2/kg BW). Differences were in the Ab/NC valency (6 for 2L vs. 46 for 4L) and number of NCs administered (9-fold lower for 4L). These formulations seemed to be at or below saturation in previous tests. These formulations had statistically similar targeting to the lungs and biodistribution to all other organs, except the spleen where 2L anti-ICAM/3DNA was enhanced (**Figure 36A**). This finding indicated that within the tested ranges, size, absolute valency, and NC concentration may not be predominant properties for biodistribution, in agreement with cell culture studies using other NCs.[163] However, it is also possible that this particular combination of size, absolute valency, and NC concentration caused no difference between the 2L and 4L formulations by serendipity. For example, although a higher valency of the 4L could lead to an increase in targeting for the 4L, a larger size of the 4L could lead to decrease in targeting, thereby causing the targeting effects for the two properties (i.e., valency and size) to cancel each other, resulting in no change overall. Hence, it is important to realize, that the aforementioned properties (size, valency, and NC concentration) did not affect the targeting in this particular combination, but their individual effects may not be distinguishable or known. Nevertheless, the remaining properties that could affect targeting were those among the group of valency density (density of Abs on the NP

surface), Ab dose administered, 3DNA dose administered, and total surface of the NCs injected, which were kept constant in this comparison. Yet, previous data had shown that valency density modulated biodistribution without varying the 3DNA dose administered or the total surface of all NCs injected (**Figure 31** or **Figure 34**); hence, these properties may be less predominant than valency density and Ab dose injected.

Next comparison was 4L*(b)* vs. 4L*(d)* (**Figure 36B**), which had similar Ab dose injected (249 μg/kg BW) but different valency density (506 vs. 879 Ab/μm^2; **Table 8**). This comparison showed enhanced lung targeting and lower liver distribution for the formulation carrying higher valency density, although this formulation was administered at lower DNA dose, NC concentration, and total NC surface per injection. A similar trend was observed when comparing 2L*(a)* vs. 4L*(d)* formulations (**Figure 36C**), which had similar Ab dose injected (249-250 μg/kg BW) but different valency density (546 vs. 879 Ab/μm^2; **Table 8**), although this was not statistically significant in the lungs likely because of the interplay of other parameters; 2L*(a)* had smaller size, greater DNA dose, greater NC concentration, and greater total NC surface per injection, which in this specific combination may have compensated for the lower valency density. In fact, comparing formulations 2L*(c)* vs. 4L*(a)* which also had similar Ab dose injected (63-69 μg/kg BW), 2L*(c)* resulted in greater lung targeting and lower liver distribution, in agreement with its greater valency density (1273 vs. 143 Ab/μm^2 for 4L), although the 2L formulation had lower DNA dose, lower total NC surface injected, and again smaller size (**Figure 36D**).

Altogether, these valency density comparisons suggest that within the appropriate parametric range, the valency density could drive targeting; yet, other properties and/or their combinations could be responsible for the valency density response since it is not possible to vary only one property at the time while keeping the others constant. Namely, along the variation in valency density, at least one other property is being varied. As seen, it is possible that other properties and/or their combinations can affect the proposed valency density response (compare **Figure 36C&D**). In addition, 2L*(b)* formulation with the same valency density as 2L*(c)* from the previous comparison (1273 Ab/μm^2) but administered at 10-times higher Ab and DNA dose than 2L*(c)*, had lower lung targeting and higher liver distribution than either the 2L*(c)* or the 4L*(d)* which had 879 Ab/μm^2 (**Figure 36E**). This would suggest that either the Ab dose or DNA dose for 2L*(b)* or the combination of the valency density, Ab dose and DNA dose for 2L*(b)* rendered oversaturation in the main target (lung), seen in **Figure 34A**. This was not observed for organs which received lower NC levels, the heart and kidneys, where biodistribution was enhanced for 2L*(b)*. Hence, since these organs (i.e., heart and kidneys) would receive the 2L*(b)* formulation with the same valency density (under the assumption of no degradation), but would receive different DNA and Ab dose due to the lungs acting as a first pass sink, the valency density could not be the reason for saturation as it was kept constant for the lungs vs. kidneys and heart. Nevertheless, it is possible that within the timeframe of the formulation transport from the lungs to the heart and the kidneys, some degradation

and Ab detachment may reduce the valency density by the time formulations reach other organs after passing the lungs. Hence, it is plausible that either valency density or Ab dose and DNA dose, or the combination of these parameters cause saturation. The comparison of 2L*(a) vs*. 2L*(b) vs*. 2L*(c)* however indicates that the saturation seen with the increase in valency density (from 2L*(a)* to 2L*(b)*) was resolved upon simply reducing the dose (from 2L*(b)* to 2L*(c)*). Hence, it is most likely that either the Ab dose or DNA dose caused saturation. Finally, comparing the 2L*(b)* (saturating condition) to 4L*(a)* formulation (low valency density condition) showed similar lung, liver, and spleen distribution. Since these formulations had the least desirable biodistribution regarding target to off-target delivery, this demonstrates that any property that is outside of the optimal parametric range, could hinder the targeting performance (**Figure 36F**).

Based on the results, it appears that the valency density response depended on the combination of other properties, as evidenced by the presence and absence of the correlation between the improved targeting and increased valency density (compare **Figure 36C&D**). Again, this could either be because the parametric range response curves for targeting are different or because the points of comparison are at different positions within the curves for the 2L vs. 4L, thereby preventing accurate comparisons of their responses. Besides the size difference, another confounding effect in the 2L vs. 4L comparisons may be due to the disparity in the density between the two 3DNA sizes (i.e., 2L is denser than 4L), which complicates the comparisons even further. Namely,

since each 3DNA branch propagates freely as a double stranded DNA from the core of 3DNA, and since, for the formulations tested in this thesis, the density of the outer arms decreases upon growing additional layers (i.e., from 2L to 4L), it is logical to assume that the third and the fourth layer of the 4L have more room for thermal motion than the second layer of the 2L. But this density difference may or may not play as important of a role depending on how the persistence length of double stranded DNA in 3DNA is affected with two-way branching with each new layer, as well as the crosslinking of 3DNA. Nevertheless, the free standing double stranded DNA has the approximate persistence length of 50 nm, which is the approximate diameter of the 2L and well below the diameter of the 4L (~170 nm). This overall indicates that 2L may have more defined surface, while 4L diameter falls in the range (170 nm) where the surface may no longer be as ordered as for the 2L. Hence, thermodynamics of surface interactions for these two 3DNA sizes may be very different and one of the 3DNA sizes may fall closer to the optimum. This parameter could then indeed introduce confounding effects when trying to establish the valency density response.

7.2.6. Comparative Drug Delivery Capacity for 2-Layer and 4-Layer Anti-ICAM/3DNA

Finally, we looked at the same comparisons as in previous section to examine the impact of all the tested properties on drug delivery. 2L and 4L formulations which had similar targeting in most organs (i.e., 2L*(a)* and 4L*(b)*) except the spleen, and had

equivalent parameters that are relevant in drug delivery, were logically equivalent in terms of biodistribution of drug-intercalating sites and arm-linked drugs, except for the spleen (**Figure 37A**). This simply reflected the biodistribution of these formulations (**Figure 36A**). Hence, the differences in size between 2L and 4L 3DNA did not play a major role in targeting/biodistribution at the organ level in this specific combination of parameters for the two formulations. Hence, both 3DNA sizes had similar drug delivery performance at the organ level under the assumption they can similarly protect the drugs from degradation.

Comparisons of 4L*(b)* vs. 4L*(d)* (**Figure 37B**), 4L*(d)* vs. 2L*(a)* (**Figure 37C**), and 4L*(a)* vs. 2L*(c)* (**Figure 37D**), which had shown increased lung targeting with increased valency density (**Figure 36B,C&D**), rendered enhanced drug-intercalating sites and drug-linking arms depending on the injected dose concentration. This is because although valency density more acutely ruled the proportion of the injected dose that reached the target (lungs) vs. clearance organs in the absence of saturating Ab dose or DNA dose concentrations, the injected dose concentration more directly modified the absolute amount of a drug reaching said tissues despite dose concentration being in the saturation range in terms of the biodistribution. This phenomenon did not depend on size, as the same trend was observed comparing formulations with same or different sizes (*e.g.*, **Figure 37B,C&D**). In all cases, the biodistribution of drug-linking arms appeared slightly more sensitive to parametric variations than the biodistribution of drug-intercalating sites.

For the comparison where the 2L formulation was oversaturating (2L*(b)* vs. 4L*(d);* **Figure 37E**) and had lowered lung targeting (**Figure 36E**), the greater dose concentration employed compensated for this saturation and resulted in a similar lung biodistribution for drug-intercalating sites and drug-linking arms as the 4L formulation. However, the greater dose concentration caused the 2L formulation to render much higher drug biodistribution in the liver and spleen. Comparing the same 2L*(b)* formulation to 4L*(a)*, so that other parametric differences were less acute, still showed a greater ratio for the lung over other organs for the 4L formulation in terms of drug-intercalating sites and drug-linking arms (**Figure 37F**). Hence, increasing the administered dose beyond the saturation point may not be ideal way to increase the delivery if the goal is lung targeting.

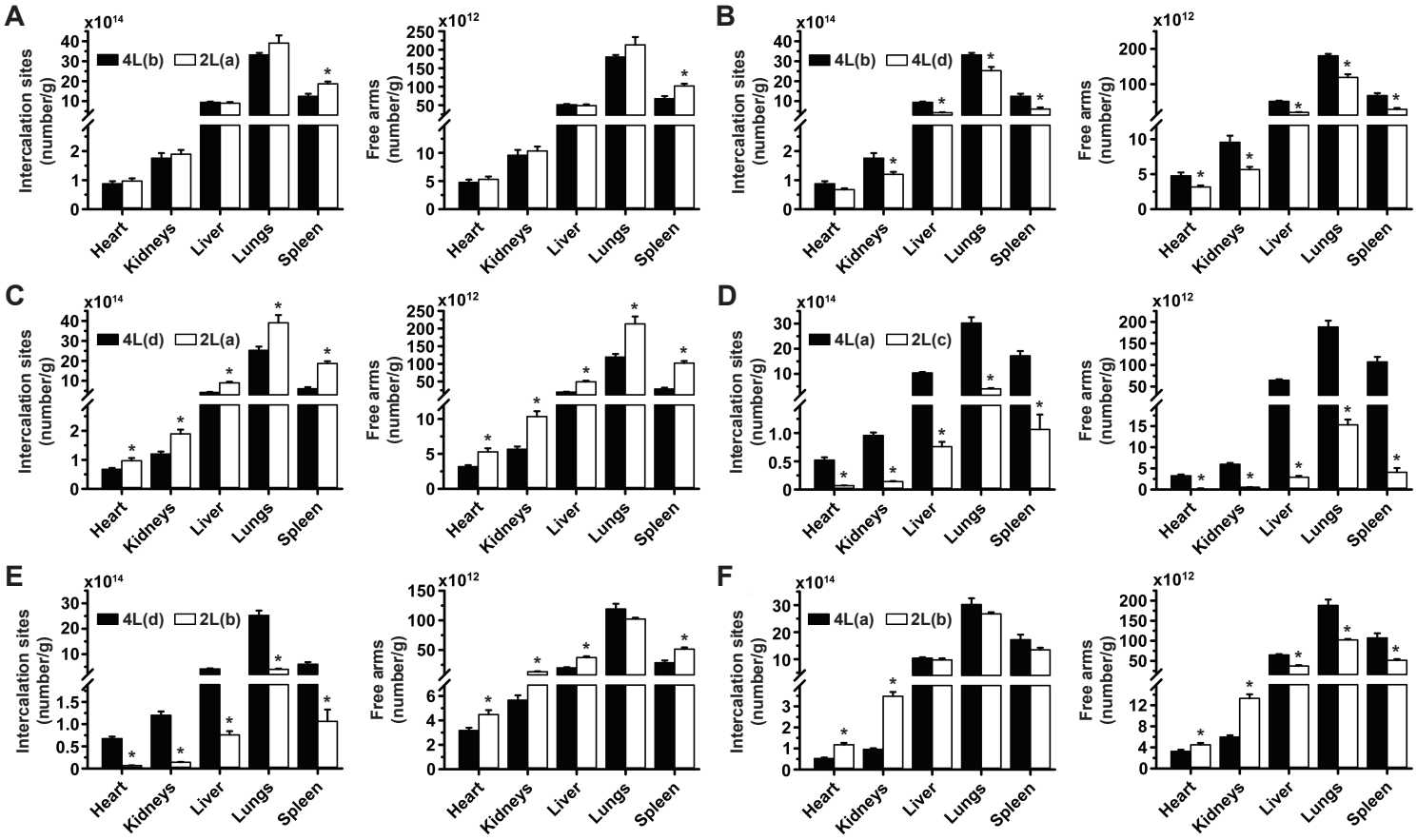

Figure 37. Comparative drug biodistribution capacity for 2L and 4L anti-ICAM/3DNA.

^{125}I-anti-ICAM/3DNA were I.V. injected in C57BL/6 mice at different sizes, targeting valencies, and/or dose concentrations, so that for each comparison certain parameters were kept similar while others changed, to infer their impact hierarchy on lung targeting and biodistribution. Organs radioactive content and weight were determined at 60 min to calculate the number of DNA drug-intercalating sites per gram of organ (left plot); and the number of outer arms free for drug coupling per gram of organ (right plot). All formulations and parametric values are in Table 8 and relative comparisons are described in Figure 36. Data are mean ± S.E.M. $n \geq 5$; * $p < 0.05$ by Student's t-test.

7.3. Conclusion

Both 2L and 4L anti-ICAM/3DNA formulations showed good lung specificity compared to IgG/3DNA and 3DNA controls.[110] The lungs clearly received higher concentrations of anti-ICAM/3DNA than the liver and spleen, while organs like the heart and kidneys received low, but specific concentrations of these carriers, resulting in a biodistribution profile similar to what has been observed for polystyrene or poly(lactic-co-glycolic acid) NPs coated with anti-ICAM Abs.[95,152] Noticeably, lung targeting was achieved at valencies much lower than previously observed for other polymeric carriers (only 6 Ab/2L-3DNA or 545 Ab/μm^2), which may be due to the way in which Ab was displayed on 3DNA. While anti-ICAM had previously been surface-adsorbed on polymer NPs, here it was annealed on the outer arms of 3DNA free-standing branches that propagate from the core of the 3DNA. This flexible attachment and the overall 3DNA flexibility may provide greater accessibility to the target, and a "liquid-like" Ab behavior on the 3DNA surface due to its freedom of movement. In contrast, many adsorbed Abs may not be able to bind the target. This difference in targeting efficiency would explain why an oversaturating anti-ICAM formulation was found here at 1273 Ab/μm^2 corresponding to Ab dose of 600 μg/kg BW, while this phenomenon had not been observed before for polymer NPs, even at ≈7,000 Ab/μm^2.[95] Thus, this analysis has allowed us to identify that the anti-ICAM/3DNA most likely utilizes a higher percentage of surface Abs, which can in return occupy more ICAM-1

molecules in the organs, causing saturation. The Ab dose delivered by anti-ICAM/3DNA where this saturation may occur was around 600 μg/kg BW and utilizing valency density of 1273 Ab/μm^2. Lowering the Ab dose to 60 μg/kg BW at valency density of 1273 Ab/μm^2 led to the recovery in targeting, indicating below saturation condition was obtained. Alternatively, the saturation could have been due to the DNA dose; although the same DNA doses did not have the same effect for the 4L, the 2L size could have caused the saturation for the DNA dose to be reached sooner by shifting the DNA dose response, or making the response range narrower. This will guide our future formulations and prompt the comparison of the anti-ICAM/3DNA vs. anti-ICAM Ab within their whole parametric range for dose concentration to further understand the relationship between the valency density and Ab dose of anti-ICAM/3DNA.

The difference in size between 2L and 4L did not seem to render any major differences in anti-ICAM/3DNA biodistribution, although multiple properties could have affected the size comparisons in different ways. When we kept constant parameters such as valency density, Ab dose, DNA dose*, etc.*, to obtain a similar biodistribution and drug-loading capacity, the absolute number of NCs arriving to the target organ was greater for 2L formulations, as expected given their smaller size. The size of 2L and 4L formulations is important to consider with respect to the capacity of internalization within cells. In the framework of ICAM-1 targeting, such size-dependency on cellular uptake has not been shown due to special properties of its

endocytic pathway.[130] When targeting receptors associated to size-sensitive routes, such as clathrin- or caveolae-mediated pathways,[113,270,271] 2L 3DNA formulations may be beneficial. Also, 2L formulations may be advantageous if the absolute number of NCs per cell would be relevant for intracellular effects. While this is not important for drugs that could diffuse through cells, like doxorubicin, it is key when therapeutics need to be delivered to subcellular compartments, such as replacement enzymes for lysosomal disorders.[272] Finally, taking into account that 2L synthesis is simpler than 4L, 2L 3DNA may be preferred.

We demonstrated that anti-ICAM valency density (number of Abs per NC surface) is a more relevant parameter than absolute valency (number of Abs per NC molecule) for targeting, as observed from multiple comparisons between 2L and 4L formulations. This finding is in agreement with our previous study showing that valency density drove binding, signaling, and internalization of anti-ICAM NCs in endothelial cells in culture,[163] and provides *in vivo* validation of our earlier observation. Since this phenomenon had been observed using polymer NCs bearing adsorbed anti-ICAM, while here the Ab was annealed to 3DNA, the prominent role of valency density stands across carriers and coupling modes.

In this system, targeting valency is a more relevant parameter than dose concentration for acutely targeting the lungs. Although both parameters caused changes in biodistribution, valency simultaneously lowered delivery to clearance organs while increasing delivery to the lungs. In addition, dose concentration could only modulate

biodistribution due to the oversaturation. Hence, it remains to be explored whether concentrations that are much lower than the ones tested could affect the biodistribution; nevertheless, such concentrations may not be therapeutically relevant. Furthermore, parameters such as the number of carriers injected or their total surface seemed less relevant. Parameters such as the total Ab dose, which is interdependent with dose concentration, size, valency density, and valency, could have also impacted lung targeting, but it is unclear which property had the greatest impact since none can be singled out as the only variable in each test due to the limitations of empirical studies. In the context of drug delivery, targeting valency may be considered the primary parameter to modulate site-specific delivery of drugs which can be highly toxic at off-target sites, as is the case for harsh chemotherapeutics used for lung cancer.[273] This parameter is less relevant in cases where patients may benefit from lung treatment and systemic delivery, such as enzyme replacement for type B Niemann-Pick disease, where the lung is the predominant but not the only organ involved.[237] Ultimately, valency and dose concentration could be adjusted to achieve the required level of lung specificity and absolute dose delivered to the lungs. In this regard, it would be relevant to take the saturation conditions into account, which should not be surpassed if side effects in off-target tissues are a concern. For instance, increasing the valency density of anti-ICAM/3DNA over the saturating point for a 2L formulation resulted in enhanced distribution to the heart and kidneys while lowering lung distribution, which

can be an advantage or disadvantage depending whether lung targeting alone or lung targeting and systemic biodistribution are required.

In general, data showed that the biodistribution of arm-linked drugs would be more sensitive to tuning anti-ICAM/3DNAvalency than intercalating drugs would be. Different drugs would differently benefit from varying valency parameters, but the delivery for all drugs and to all the organs would increase with increasing the administered dose. For instance, a consideration of increasing the targeting valency is that the number of arms free for drug coupling would be reduced, which would not be the case for intercalating drugs. Hence, valency must be balanced more carefully for arm-linked drugs to achieve sufficient lung specificity required while bringing adequate molecules of a therapeutic load. A possible solution to overcome this caveat is attaching multiple drug molecules to the same arm, which can be easily achieved by design of the DNA oligonucleotide used for drug conjugation.

In summary, the knowledge obtained is relevant in selecting which parameter(s) of anti-ICAM/3DNA to vary depending on the drug and application pursued.

Chapter 8: Final Remarks and Future Directions

8.1. Final Remarks

DNA-NPs hold promise in nanomedicine due to their precise, controllable, and versatile functionalities and bio-physicochemical characteristics that are compatible with the biological environment in the body.[19,57,71,72,200,204,214] Many of these functionalities, particularly the delivery of drugs and other cargos, may be enhanced and benefit from the accumulation of DNA-NPs within specific locations in the body.[1,2,75,81,196] Targeting accessible cell surface markers represents a viable option towards achieving this goal, but it is still poorly explored for DNA-NPs due to the novelty of the field.[274]

In this dissertation, we focus on ICAM-1 targeting as a clinically relevant therapeutic target that is readily available for binding from the bloodstream and primarily located in the lungs due to high ICAM-1 content and vascular density of this organ.[2,7,237,262,275–277] Due to these and other biological properties of ICAM-1,[95–97,170,276] our laboratory, among others, has been extensively exploring, characterizing, and applying ICAM-1 functionality towards site-specific localization of therapeutic interventions, many of which utilize multivalent binding.[14,49,95,237,275,278] Advancements of ICAM-1 applications have recently accelerated among research groups and our

laboratory has revealed much of the potential for this receptor, particularly for lung targeting.[152,242,279]

In light of this, our laboratory has started exploring ICAM-1 targeting of DNA NCs, particularly 3DNA.[58] 3DNA holds promise and is advancing towards various clinical applications across several laboratories.[19,89–93] 3DNA, a DNA-made branched structure of precise architecture and size, has promising cargo carrying capacity.[89] Our laboratory has demonstrated the highly efficient and ligand-specific targeting of various prototype multivalent Ab/3DNA NCs in endothelial and other cells.[58] Furthermore, our lab has shown that Ab/3DNA NCs can mediate intracellular drug delivery, including delivery to the cytosolic compartment.[58] However, the translation of targeting functionality *in vivo*, although promising, was modest for this prototype design,[110] which prompted us to test a new Ab/3DNA design.[89–91,93,110] To evaluate anti-ICAM/3DNA performance and bio-physicochemical properties, we studied the biodistribution and specific lung targeting of various anti-ICAM/3DNA formulations and the corresponding controls upon *in vivo* I.V. injection in mice, as well as compared these results with the PLGA counterparts of similar valency, size, and surface ζ-potential.

As a first step towards exploring anti-ICAM/3DNA targetability, we focused in the Chapter 5 of this dissertation on evaluating the accuracy of a radiotracing-based biodistribution method that we planned to utilize for the rest of our project; namely, despite being one of the most sensitive and quantitative methods,[236,254] radiotracing can

suffer from the uncertainty of whether the labeled samples or the free label are/is being traced. This is especially relevant when handling biodegradable samples as is in the case with anti-ICAM/3DNA.

Not surprisingly, we detected the generation of low but measurable levels of free radiolabel upon incubation of the Ab/3DNA samples in tissue homogenates and blood samples at the physiological temperature of 37 °C and confirmed that the TCA assay can be used to distinguish the free radiolabel from the radiolabeled samples despite the presence of tissue homogenates. The presence of free radiolabel in the injection and organ samples was assumed to confound the biodistribution results due to the expected differences in the biodistribution of the radiolabeled samples vs. free radiolabel, as well as the potential metabolic accumulation of free radiolabel *in vivo*. This has prompted us to modify the radiotracing-based biodistribution method, such that the signal originating exclusively from the label attached to the NP can be distinguished from the signal originating from the free label present in the samples. This would allow for a more robust quantification and tracing of NP biodistribution.

To accomplish this, we tested two methods for correcting the presence of free radiolabel and compared the results. First, in the indirect method, we measured the free radiolabel biodistribution upon injection of 100% free radiolabel and used this information to correct for the free radiolabel in the independent biodistribution experiment that encompassed the injection of the radiolabeled Ab/3DNA along with some free radiolabel. We compared this indirect method to a direct method where the

presence of free radiolabel was directly determined from the biodistribution samples (i.e. blood and organs) within the same experiment, encompassing the injection of radiolabeled Ab/3DNA along with some free radiolabel. Our results indicated that the presence of any free radiolabel in the biodistribution samples needs to be accounted specifically within the same experiment, for each organ or blood sample, in order to obtain accurate biodistribution results, rather than indirectly applying the corrections from the known biodistribution of free radiolabel. Overall, the TCA precipitation of animal samples permitted the accurate classification of signals originating from the free radiolabel vs. radiolabeled NP. The accurate biodistribution characterization achieved with this method may provide a vital step in designing and optimizing NP delivery.

In Chapter 6 of this dissertation, we investigated the biodistribution and lung targeting of a new anti-ICAM/3DNA design I.V. administered in mice, to learn about their bio-physicochemical characteristics from the aspect of a translationally relevant model of pulmonary ICAM-1 targeting. Since the new anti-ICAM/3DNA design requires that the anti-ICAM Abs be conjugated to oligonucleotides to allow for Ab hybridization to 3DNA, we first confirmed that the modification of the Ab with oligonucleotides did not impair their targeting compared to unmodified anti-ICAM Ab. Furthermore, compared to anti-ICAM Ab, the anti-ICAM-oligo Ab showed improved targeting to the lungs, although also had enhanced accumulation in the liver and spleen.

Next, we verified the efficient coupling of 3DNA with anti-ICAM-oligo Abs. Also, anti-ICAM/3DNA had a uniform size and surface charge suitable for *in vivo*

applications (~180 nm hydrodynamic diameter and ~-38 mV ζ-potential). Then, we demonstrated the stability of this efficient Ab to 3DNA functionalization, under degradation conditions, in a serum at the physiological temperature of 37 °C. Moreover, our results are in agreement with Genisphere® LLC's observation that 3DNA exhibited amenable resistance to degradation in the serum (~9.5 h half-life), which was further improved upon by coating Abs on the 3DNA surface (~26 h half-life), thereby suggesting the protective role of Abs linked to the 3DNA surface.

Most importantly, anti-ICAM/3DNA had efficient and specific accumulation in the targeted organ, the lungs, along with reduced accumulation in the clearance organs such as the liver, spleen, and kidneys. To the best of our knowledge, no other report has demonstrated such high targeting specificity for an Ab-DNA-built NP *in vivo*; per the specificity index, anti-ICAM/3DNA accumulated in the lungs 424-fold over control IgG/3DNA, despite serum proteins, degrading enzymes, and the presence of scavenger receptors throughout the body. Indeed, ICAM-1-targeted systems have been reported by our lab and others to be capable of highly specific and efficient targeting to the lungs and other organs.[7,96,107] The targeting specificity for ICAM-1-targeted NPs is remarkable compared to most other targeted NPs, which highlights the fact that active targeting by Abs and perhaps other affinity ligands offers a great opportunity to enhance site-specific drug delivery; the enhanced site-specific drug delivery should be possible if the selected targets are expressed at specific sites and are accessible from the bloodstream, as in the case of ICAM-1 targeting. In addition, by comparing anti-

ICAM/3DNA to anti-ICAM Ab, we demonstrated enhanced targeting for anti-ICAM/3DNA due to its size and multivalent binding interactions to the lungs. We further demonstrated the relevance of anti-ICAM/3DNA for clinical applications of lung targeting by outperforming an anti-ICAM/PLGA NP of similar size, PDI, ζ-potential, and number of targeting Abs; PLGA is widely used in clinical applications, including drug delivery.

In Chapter 7 of this dissertation, we further explored anti-ICAM/3DNA properties. We evaluated their targeting Ab valency, their dose concentration of targeted formulations, and their size to better understand the role of these properties in the parametric modulation of anti-ICAM/3DNA biodistribution and drug delivery. We specifically looked at the potential of anti-ICAM/3DNA to deliver drugs that can be loaded on the inner core of 3DNA (e.g., intercalating drugs) or loaded on the surface of 3DNA (e.g., DNA hybridization of peripheral arms). We have shown that within the tested parametric ranges, all three properties could play a role in kinetics and biodistribution, perhaps via different mechanisms. As an example, the modulation of valency density had the most important role in lung targeting (the major target), while the formulation size seemed to affect spleen targeting. On the other hand, the dose concentration did not seem to affect lung targeting, unless saturating conditions were exceeded. This was possible since the lungs were found to act as a sink for targeted formulations, most likely due to the high ICAM-1 content and being the first capillary network to be supplied upon I.V. injection, before any other organ would have a chance

to accumulate NPs. This phenomenon has allowed for the reduced accumulation to clearance organs despite the presence of ICAM-1 in these organs. Furthermore, this sink phenomenon which could get saturate in combination with the valency density or dose concentration, or the combination of the aforementioned factors and other properties such as Ab dose, 3DNA size, DNA dose, etc. could have contributed to the modulation of targeting to other organs as well as their saturation, as demonstrated by the lack of response in the heart under certain tested conditions. In fact, all organs demonstrated variable biodistribution responsiveness to the parametric modulations tested, indicating a complex interplay between the parameters and the biological environment. This was the first time that the saturating condition was found for the ICAM-1 targeted formulations *in vivo*.

The absolute delivery of anti-ICAM/3DNA was greatly affected by modulating the dose concentration, but other properties had an effect as well. Nevertheless, as mentioned, the dose concentration seemed to affect organ delivery without much influence on lung targeting. Looking at how the aforementioned anti-ICAM/3DNA properties affected drug delivery, we found that the delivery of surface loaded drugs was sensitive to valency modulation. Namely, although increased valency density could lead to improved targeting, it also reduces the number of free arms available for drug coupling. In this manner, the effect of the decreased drug loading capacity was greater than the effect of improved targeted delivery, causing an overall reduction in the delivery of surface drugs to the lungs. In contrast, the drugs incorporated within the

inner core of the 3DNA were not affected by valency modulation and their delivery resembled the absolute delivery and biodistribution trends obtained for the respective anti-ICAM/3DNA formulations.

Overall, given the tunability and versatility of DNA-NP properties that allow for precise control in numerous applications, the success of many of these applications will ultimately be limited by the accessibility and expression profile of biological targets (e.g., disease markers) *in vivo*, for which we currently may have very limited control over. Hence, this is going to require the incorporation of additional functionalities (e.g., various targeting modalities) in future DNA-NP designs. From this aspect, anti-ICAM/3DNA represents a promising approach to improve site-specific drug delivery due to ICAM-1 accessibility and overexpression at the diseased sites.[7] Indeed, it has been found that the behavior of DNA-NCs utilized in this work, namely 3DNA®, depends on the surface molecules functionalized on 3DNA, and not the 3DNA itself. Hence, 3DNA seems like a highly adequate NC for targeted drug delivery and is intensively being explored across academia and big pharma companies.[19,58,89–93,280,281]

8.2. Future Directions

As summarized above, the findings in this dissertation have shown high potential for the utilization of DNA-NPs and targeting ligands as tools to direct drug delivery to specific sites within the body, particularly utilizing anti-ICAM/3DNA as an

example of a lung targeting application. The modification of a radiotracing-based biodistribution method with TCA precipitation assay was found to be particularly useful in accurately evaluating anti-ICAM/3DNA targeting *in vivo*. However, several characterization aspects and design parameters pertaining to the translation of this technology remain to be evaluated.

The TCA assay modification of the biodistribution method allowed for the accurate tracing of presumably intact radiolabeled samples. Nevertheless, future work must verify the degradation state of radiolabeled NPs and determine conditions under which the degradation fractions of radiolabeled NPs can still be found in the TCA precipitate fraction vs supernatant fraction. Future work must also determine the origins of the difference between free radiolabel biodistribution vs. the biodistribution of free radiolabel co-injected with radiolabeled NPs, to determine whether the difference is due to metabolic degradation, the concentration dependency of free radiolabel administered, or the influence of the presence of NPs. In case the difference is due to metabolic degradation, future work will focus on developing a TCA method that can be used to detect free label generation to help measure/trace the degradation of NPs *in vivo*. This is important as different organs have different capacities to accumulate and metabolize the labeled NP components and the sites where degradation occurs also vary. Testing the free label content in each organ at different time points may provide valuable information that will reveal the potential interdependency between NP accumulation and NP degradation processes in a particular organ.

While we show the efficient and ICAM-1-specific targeted delivery of anti-ICAM/3DNA in this dissertation, future work must also focus on expanding our understanding of the obtained results, with a focus on its mechanistic aspects. This improved understanding can then allow for a rational design in the future. For example, the focus in this dissertation was on tracing the Ab component of anti-ICAM/3DNA. Currently, we are working on directly confirming the delivery of the 3DNA component of anti-ICAM/3DNA to the blood and organs. Our preliminary results show that tracing the 3DNA component of anti-ICAM/3DNA also results in lung-specific targeting, yet some biodistribution values vary. To rationally improve the anti-ICAM/3DNA design, it is necessary to first understand the mechanisms driving the observed outcomes, which may be due to different tissue processing of Ab vs. 3DNA components prior or after targeting, or after uptake by tissue cells. Hence this will require a detailed investigation in the future. For instance, preliminary examination of the bladder accumulation of degraded fractions shows a higher degradation rate for the 3DNA component compared to the Ab component of anti-ICAM/3DNA. This is in accord with the fact that Ab degradation rates are known to be slower compared to most DNA structures.[3,19,187,251]

Furthermore, anti-ICAM/3DNA interactions with biological environment and how this affects each stage of transport and targeting requires detailed evaluation. This includes interactions with blood components (e.g., opsonins), the response to ICAM-1 binding due to activation of acidification mechanisms via NHE pump, ICAM-1

clustering and mobility, etc. The binding and intracellular transport needs to be evaluated in major cell types including endothelial cells, immune cells, hepatocytes, etc.[47,71,72] In this regard, we have started quantitative and qualitative characterization of anti-ICAM/3DNA of different sizes and conjugated with a model cargo (e.g., biotin) in endothelial cells *in vitro*. Furthermore, the behavior of anti-ICAM/3DNA and recognition by cell machinery in each cellular compartment needs to be characterized in detail. For example, lysosomal fractions may be degraded due to lysosomal degrading enzymes, while cytosolic fractions may not only be degraded enzymatically, but also be recognized by an acid sensing DNA sensor, which is sequence independent but cell dependent.[282,283] Potential utilization of anti-ICAM/3DNA by the cells as building blocks also needs to be evaluated. Particular focus should be given to understanding the ability of DNA-NPs to saturate the metabolic capacity and NP uptake abilities in the clearance organs (e.g., liver), compared to the stiffer and less biodegradable NPs. Namely, the accumulation and storage of NPs in lysosomes can affect autophagy and drastically affect the cell function.[284] Hence, intracellular transport, which may be different for 3DNA compared to other NP systems, may play a role in target vs. off-target accumulation *in vivo*. The comprehensive knowledge of anti-ICAM/3DNA binding interactions and transport can then be utilized to optimize the design parameters for each of the transport stages and enhance the overall site-specific drug delivery.

Future work must also focus on the better understanding of *in vivo* targeting differences between anti-ICAM/3DNA and anti-ICAM/PLGA NPs, by evaluating their binding aspects and deciphering the role of different Ab functionalization strategies for the anti-ICAM/3DNA vs. anti-ICAM/PLGA NPs. To further understand the differences in the results between the anti-ICAM/3DNA and anti-ICAM/PLGA tested formulations, it is necessary to better understand whether the differences were solely due to the material which most often arises from different opsonization profiles, or due to the different overall flexibility of the formulations. Moreover, to improve our understanding of anti-ICAM targeted DNA-NPs, different DNA designs should be tested (e.g., different geometries, structures, sequences etc.). In addition, to better understand the interplay between NP material and architecture (3DNA vs. PLGA NPs), the role of functionalization methodology (Ab surface adsorption vs. direct Ab hybridization via oligos vs. Ab based affinity coupling), the presence of flexible linkers, and the blood flow in endothelial targeting, flow chamber studies may be used to reveal additional mechanistic aspects of the observed results *in vivo*.

As mentioned, the role of opsonization of Ab/3DNA, including the potential synergetic effects on ICAM-1 targeting, will require careful examination. It is expected that opsonization would be similar for anti-ICAM/3DNA and IgG/3DNA due to the similarity between their surface characteristics. Namely, specific anti-ICAM and non-specific IgG are a similar molecular species and were used at the same Ab valency and on the same nanoconstruct (i.e. 3DNA). Nevertheless, synergetic effects between the

opsonins or other blood components (e.g., ions, DNA degrading enzymes, DNA binding proteins, cells, etc.) and ICAM-1 targeting cannot be disregarded. In addition, the surface of immune cells in the blood, liver, etc. that have the presence of the ICAM-1 receptor can express scavenger receptors, Fc receptors, and TLR9 which is present in endothelial cells internally.[107,285,286] This is relevant since anti-ICAM/3DNA NCs contain ICAM-1 targeting regions, Fc targeting regions, and TLR9 targeting regions even in the absence of CpG sequences. How TLR9 activation and the potential ICAM-1 overexpression by anti-ICAM/3DNA would influence targeting is another question to be explored.[285] Hence, both components, anti-ICAM and 3DNA, may interact with various species and cells in the blood, besides the endothelium, and could potentially generate synergetic targeting mechanisms to ICAM-1. Moreover, to measure DNA NPs ability to avoid scavenger receptor clearance, future work must employ targeting ligands that do not target Fc receptors on cells that simultaneously express scavenger receptors. Various knock out models will need to be employed to test these differences (e.g., ICAM-1, TLR-9, nucleic acid sensing knock outs, as well as immunodeficient mice). Whichever interactions are found to be the case in future studies, it still does not change the fact that the presence of ICAM-1 targeting functionality is necessary for the preferential anti-ICAM/3DNA distribution to the lungs, as observed for the control anti-ICAM and other anti-ICAM-targeted NPs.

Future work must also examine the cause of the differences in behavior between the anti-ICAM that was conjugated to the oligo vs. the one that was not. Potential

reasons that could alter targeting and need to be explored are: 1) the manufacturing and purification process of anti-ICAM-oligo 2) the conjugation that could cause an Ab conformation with increased affinity 3) a site-specific charge alteration due to the DNA oligonucleotides presence that could affect binding with blood components, transport and binding with targets 4) DNA oligonucleotides could alter the state of the cell, such as causing stimulation of ICAM-1 overexpression which may or may not be relevant within the timeframes used in this work, but may be important for other targeted delivery applications.[282,285]

While the work in this dissertation started exploring the parametric range for anti-ICAM/3DNA valency, dose, and size, the evaluation of additional parametric points *in vivo* and a detailed study *in vitro* are necessary to complete our understanding of anti-ICAM/3DNA's role and hierarchy. It is important to evaluate additional parametric points because each property could become the most important at a particular parametric value. For example, administering NPs that are too large would lead them to be mechanically trapped before reaching any major organs and therefore would automatically classify this size parameter as the most important. Alternatively, administering the dose close to zero would give this property the most importance, similar to driving the targeting valency to zero condition.[31,43,115,117,130,161] The interplay between parameters and hierarchy ranking shifts can be understood from the complete response curves obtained for each of the properties. The practical significance of the optimal parametric range for each property and the relevance of its hierarchy can then

be evaluated from the aspect of relevant drug delivery dosages necessary to induce an optimal therapeutic effect, while achieving optimal biodistribution. To optimize dosage schedule and frequency for clinical use, the optimal therapeutic performance needs to be balanced with the cost and convenience of treatment. In addition, the role of 3DNA flexibility and density and the properties that are different between 2L vs. 4L 3DNA formulations needs to be better understood.

Due to the high targeting efficiency of anti-ICAM/3DNA, the parametric range for their valency and dose was probably narrow in the *in vivo* healthy model, which lacks ICAM-1 overexpression (yet the expression of ICAM-1 in healthy animals is sufficient for targeting). To broaden the parametric ranges and demonstrate clinical relevance, future studies should explore these properties in diseased models associated to ICAM-1 overexpression. Our preliminary results show that similar to other ICAM-1-targeted formulations,[262] anti-ICAM/3DNA targeting could increase by 22% in the lungs (the target organ) of the LPS induced, systemic inflammation mouse-model. Nevertheless, due to the systemic inflammation in this particular model, which is not lung specific, the targeting in other organs increased up to 160%. Hence, the future studies will focus on lung-specific inflammation models, such as intratracheal LPS administration. Each intended application often requires a unique combination of targeting parameters that are specific to the formulation, the targeted marker/s, the biological environment, and the drug to be delivered.[7,10,33] For example, tumor targeting may require a low number of targeting moieties (targeting valency) per NP to

maximize the EPR effects and minimize targeting to healthy cells that have a basal expression of the targeted receptors.[33] Targeting diseased sites while avoiding healthy tissues may require a particular targeting avidity for each application to allow for preferential targeting.[107] Hence, future studies must explore the potential of the anti-ICAM/3DNA system for site specific drug delivery in specific applications, such as targeting to disease sites in lung cancer, as well as for applications requiring systemic organ delivery for the treatment of genetic diseases. Most importantly, to allow for comparisons with other DNA-NP targeting systems reported in literature and to determine the role of EPR in ICAM-1 targeting, anti-ICAM/3DNA would need to be tested in cancer models other than lung cancer, with and without the presence of EPR-associated pathology.

Moreover, the ability of anti-ICAM/3DNA to carry and deliver drugs needs to be verified for a variety of cargos in *in vitro* and *in vivo* models. While in this dissertation we have estimated the delivery of drug types carried within the 3DNA core or carried on the 3DNA surface, it is not known how different parameters would affect the protection of the drug, or whether the drugs would affect the targeting of anti-ICAM/3DNA. For example, while higher targeting valency of anti-ICAM/3DNA may allow lower drug loading on the surface, the higher valency may also contribute to the greater degree of protection to both the drug and the 3DNA. Our results in this dissertation did show that Abs can potentially protect Ab/3DNA formulations. In

addition, it remains to be measured whether all the free arms that are not occupied with Abs could be loaded with a drug.

Furthermore, most therapeutics require cytosolic access to execute their functions.[10,46,58,70,143,282] The exploration of DNA-NP properties and endocytic receptors that support cytosolic delivery phenomena is another very novel and active area of research, as unrestrained access to target sites at the subcellular level is considered the holy grail of targeted drug delivery. Moreover, the influence of design parameters on cell uptake and the overall intracellular transport beyond the cytosolic compartment must be evaluated. It is interesting to note that the cytosolic delivery function of 3DNA *in vitro* is possible without the need to load the cargo on 3DNA, and hence this function is independent of the 3DNA cargo carrying ability, as demonstrated by early *in vitro* work in our lab. Therefore, future work must test the cytosolic delivery function of *in vivo* anti-ICAM/3DNA independently of the drug carriage function, since the targeted localization of the cell uptake and cytosolic delivery functions has the potential to create a site-specific sink condition for the therapeutics that are co-administered along with the anti-ICAM/3DNA, and hence concomitantly contribute to drug accumulation in a site-specific manner. It is not known whether the attachment of drugs onto 3DNA may potentially reduce the efficiency of cytosolic delivery, despite increasing the site-specific accumulation. The best strategy needs to be validated *in vitro* and *in vivo* and will depend on the requirements of the application, particularly pertaining to the therapeutic side effects, stability of the therapeutics in blood, and

financial costs. Currently, we are exploring the anti-ICAM/3DNA-mediated targeted cytosolic delivery of a model siRNA for the treatment of a model lung disease.

While the work presented here is highly supportive of advancing preclinical testing toward focused clinical applications, future work must carefully examine aspects regarding the potential side effects of the anti-ICAM/3DNA platform. The clearance, toxicity, immune response, long term safety, and dose responses all need to be evaluated. Current research points to DNA-NPs being safe in general. However, the high versatility of DNA-NP designs, and the known influence of DNA sequences, size, flexibility, degradation rates, surface topography, etc. demand detailed evaluations of DNA-NPs on their individual bases. Furthermore, to evaluate the anti-ICAM/3DNA safety, more relevant materials need to be utilized for clinical applications, such as targeting moieties that are not recognized by immune cells (e.g., peptides, antigen-binding fragments, aptamers, etc.) Due to anti-ICAM/3DNA's highly efficient targeting requiring only 15 or less Abs for highly specific targeting, this technology may work well with aptamers that have much lower binding affinities. This would allow for the tuning of the design to avoid healthy tissues, similarly to the effect of decreased valency, which has been shown to result in improved selectivity, thereby contributing to the overall therapeutic safety. While PEG functionalization may improve selectivity by balancing the targeting avidity initially, the long term safety and Ab generation need to be considered.[287] As shown by our lab, CD47, a self-recognition signal molecule, may be a better choice to balance targeting functions.[238] Future work

will also explore whether a similar degree of specificity will be achieved by targeting 3DNA to other markers that engage various sizes and valencies of binding, and how the selection of biological targets and other design properties affect DNA-NP safety.

8.3. Overall Conclusion

Overall, the work in this dissertation has significantly contributed to the advancement of the anti-ICAM/3DNA targeting platform towards effective lung targeting. Using a modified radiotracing-based biodistribution method, we obtained a detailed, accurate, and quantitative biodistribution characterization of anti-ICAM/3DNA *in vivo*, evaluated anti-ICAM/3DNA targeting specificity to the lungs and other organs, and tested the response of biodistribution, specific targeting, and hypothetical drug delivery to the parametric modulation of anti-ICAM/3DNA targeting valency, dose, and size. The results demonstrate the high tunability of the anti-ICAM/3DNA system for efficient and specific delivery, showing promise for lung therapy.

Appendices

Publications

The text, data, and figures are from the following publications and prepared manuscripts:

1) **Roki, Nikša**, Zois Tsinas, Melani Solomon, Jessica Bowers, Robert C. Getts, and Silvia Muro. "Unprecedently high targeting specificity toward lung ICAM-1 using 3DNA nanocarriers." Journal of Controlled Release 305 (2019): 41-49.

2) **Nikša Roki**, Lou Casta, Melani Solomon, Jessica Bowers, Robert C. Getts, and Silvia Muro, A Method to Improve Quantitative Radiotracing-Based Analysis of the In Vivo Biodistribution of Drug Carriers, Pharmaceutical Research, 2020, (invited and awaiting submission)

3) **Nikša Roki**, Melani Solomon, Jessica Bowers, Robert C. Getts, and Silvia Muro, Modulating Design Parameters of ICAM-1-Targeted 3DNA Nanocarriers to Tune Pulmonary Targeting for Drug Delivery, Advanced Functional Materials, 2020, (in preparation)

Abstracts

1) **Nikša Roki**, Jessica Bowers, Robert C. Getts, Silvia Muro. “ICAM-1 Targeting In Vivo Using a DNA-Built Nanodevice”. Abstract for the NanoDDS Symposium, 15th International Nanomedicine & Drug Delivery Symposium, 2017 *poster

2) **Nikša Roki**, Jessica Bowers, Robert C. Getts, Silvia Muro. “ICAM-1 Targeting In Vivo Using a DNA-Built Nanodevice”. CT3N Symposium, Center for Targeted Therapeutics and Translational Nanomedicine Symposium. Philadelphia, PA (2017). *poster

3) **Nikša Roki**, Jessica Bowers, Robert C. Getts, Silvia Muro. "Role of Valency and Concentration Dose of ICAM-1-Targeted 3DNA Carriers In Vivo". Abstract for the BMES, Biomedical Engineering Society. Atlanta, GA (2018). *poster

4) **Nikša Roki**, Jessica Bowers, Robert C. Getts, Silvia Muro. "Role of Valency and Concentration Dose of ICAM-1-Targeted 3DNA Carriers In Vivo". CT3N Symposium, Center for Targeted Therapeutics and Translational Nanomedicine Symposium. Philadelphia, PA (2018). *poster

5) **Nikša Roki**, Melani Solomon, Jessica Bowers, Robert C. Getts, Silvia Muro, "In vivo Biodistribution of an Anti-ICAM-Functionalized Drug Delivery Nanocarrier made of DNA (3DNA)". Mid-Atlantic DNA Nanotechnology Symposium (MADNano2019) at NIST. Gaithersburg, MD (2019). *oral presentation

Fellowships and Awards

Ann G. Wylie Semester Dissertation Fellowship (December-May 2020)

Graduate fellowship, Genisphere® LLC (April 2017-December 2019)

References

1. Langer, R. Drug delivery and targeting. *Nature* **392**, 5–10 (1998).
2. Muzykantov, V. & Muro, S. Targeting delivery of drugs in the vascular system. *International journal of transport phenomena* **12**, 41 (2011).
3. Awwad, S. & Angkawinitwong, U. Overview of Antibody Drug Delivery. *Pharmaceutics* **10**, (2018).
4. Cressey, P., Zhang, W., Turcanu, M., Cochran, S. & Thanou, M. Design of Nanoparticles for Focused Ultrasound Drug Delivery. in *Nanotechnology Characterization Tools for Tissue Engineering and Medical Therapy* (ed. Kumar, C. S. S. R.) 205–239 (Springer, 2019). doi:10.1007/978-3-662-59596-1_5.
5. Pillai, G. Nanomedicines for Cancer Therapy: An Update of FDA Approved and Those under Various Stages of Development. 13 (2014).
6. Beltrán-Gracia, E., López-Camacho, A., Higuera-Ciapara, I., Velázquez-Fernández, J. B. & Vallejo-Cardona, A. A. Nanomedicine review: clinical developments in liposomal applications. *Cancer Nano* **10**, 11 (2019).
7. Muro, S. Intercellular Adhesion Molecule-1 and Vascular Cell Adhesion Molecule-1. in *W.C. Aird (Ed.) Endothelial biomedicine* 1058–1070 (Cambridge University Press, New York, 2007).
8. Kaplon, H., Muralidharan, M., Schneider, Z. & Reichert, J. M. Antibodies to watch in 2020. *mAbs* **12**, 1703531 (2020).

9. McMillan, J., Batrakova, E. & Gendelman, H. E. Cell Delivery of Therapeutic Nanoparticles. *Prog Mol Biol Transl Sci* **104**, 563–601 (2011).

10. Muro, S. Challenges in design and characterization of ligand-targeted drug delivery systems. *Journal of controlled release* **164**, 125–137 (2012).

11. Shih, Y.-C. T., Smieliauskas, F., Geynisman, D. M., Kelly, R. J. & Smith, T. J. Trends in the Cost and Use of Targeted Cancer Therapies for the Privately Insured Nonelderly: 2001 to 2011. *J Clin Oncol* **33**, 2190–2196 (2015).

12. Aggarwal, S. Targeted cancer therapies. *Nature Reviews Drug Discovery* **9**, 427–428 (2010).

13. Champion, J. A. & Mitragotri, S. Role of target geometry in phagocytosis. *PNAS* **103**, 4930–4934 (2006).

14. Hsu, J. B., Bhowmick, T., Burks, S. R., Kao, J. P. & Muro, S. Enhancing biodistribution of therapeutic enzymes in vivo by modulating surface coating and concentration of ICAM-1-targeted nanocarriers. *Journal of biomedical nanotechnology* **10**, 345–354 (2014).

15. Papademetriou, I. T., Garnacho, C., Schuchman, E. H. & Muro, S. In vivo performance of polymer nanocarriers dually-targeted to epitopes of the same or different receptors. *Biomaterials* **34**, 3459–3466 (2013).

16. Torchilin, V. P. Multifunctional nanocarriers. *Advanced Drug Delivery Reviews* **64**, 302–315 (2012).

17. Yao, Z., Dai, W., Perry, J., Brechbiel, M. W. & Sung, C. Effect of albumin fusion on the biodistribution of interleukin-2. *Cancer Immunology, Immunotherapy* **53**, 404–410 (2004).

18. Zhang, Q. *et al.* DNA Origami as an In Vivo Drug Delivery Vehicle for Cancer Therapy. *ACS Nano* **8**, 6633–6643 (2014).

19. Getts, R. & Muro, S. DNA-based drug carriers: the paradox of a classical "cargo" material becoming a versatile "carrier" to overcome barriers in drug delivery. *Current pharmaceutical design* **22**, 1245–1258 (2016).

20. Jiang, D., England, C. G. & Cai, W. DNA nanomaterials for preclinical imaging and drug delivery. *Journal of Controlled Release* **239**, 27–38 (2016).

21. Gatoo, M. A. *et al.* Physicochemical Properties of Nanomaterials: Implication in Associated Toxic Manifestations. *BioMed Research International* https://www.hindawi.com/journals/bmri/2014/498420/ (2014) doi:10.1155/2014/498420.

22. Wang, J., Lu, Z., Wientjes, M. G. & Au, J. L.-S. Delivery of siRNA Therapeutics: Barriers and Carriers. *The AAPS Journal* **12**, 492–503 (2010).

23. Davis, M. E. *et al.* Evidence of RNAi in humans from systemically administered siRNA via targeted nanoparticles. *Nature* **464**, 1067–1070 (2010).

24. Jones, A. T. Gateways and tools for drug delivery: Endocytic pathways and the cellular dynamics of cell penetrating peptides. *International Journal of Pharmaceutics* **354**, 34–38 (2008).

25. Fehring, V. *et al.* Delivery of Therapeutic siRNA to the Lung Endothelium via Novel Lipoplex Formulation DACC. *Molecular Therapy* **22**, 811–820 (2014).

26. Lorenzer, C., Dirin, M., Winkler, A.-M., Baumann, V. & Winkler, J. Going beyond the liver: Progress and challenges of targeted delivery of siRNA therapeutics. *Journal of Controlled Release* **203**, 1–15 (2015).

27. Douglas, S. M., Bachelet, I. & Church, G. M. A Logic-Gated Nanorobot for Targeted Transport of Molecular Payloads. *Science* **335**, 831–834 (2012).

28. Giljohann, D. A. *et al.* Oligonucleotide Loading Determines Cellular Uptake of DNA-Modified Gold Nanoparticles. *Nano Letters* **7**, 3818–3821 (2007).

29. Anselmo, A. & Mitragotri, S. Designing drug-delivery nanoparticles. *Chem. Eng. Prog* **112**, 52–57 (2016).

30. Moghimi, S. M. & Szebeni, J. Stealth liposomes and long circulating nanoparticles: critical issues in pharmacokinetics, opsonization and protein-binding properties. *Progress in Lipid Research* **42**, 463–478 (2003).

31. Albanese, A., Tang, P. S. & Chan, W. C. W. The Effect of Nanoparticle Size, Shape, and Surface Chemistry on Biological Systems. *Annual Review of Biomedical Engineering* **14**, 1–16 (2012).

32. Nehoff, H., Parayath, N. N., Domanovitch, L., Taurin, S. & Greish, K. Nanomedicine for drug targeting: strategies beyond the enhanced permeability and retention effect. *Int J Nanomedicine* **9**, 2539–2555 (2014).

33. Bae, Y. H. & Park, K. Targeted drug delivery to tumors: Myths, reality and possibility. *Journal of Controlled Release* **153**, 198–205 (2011).

34. Coats, S. *et al.* Antibody–Drug Conjugates: Future Directions in Clinical and Translational Strategies to Improve the Therapeutic Index. *Clin Cancer Res* **25**, 5441–5448 (2019).

35. Lambert, J. M. & Morris, C. Q. Antibody–Drug Conjugates (ADCs) for Personalized Treatment of Solid Tumors: A Review. *Adv Ther* **34**, 1015–1035 (2017).

36. Sassoon, I. & Blanc, V. Antibody–Drug Conjugate (ADC) Clinical Pipeline: A Review. in *Antibody-Drug Conjugates* (ed. Ducry, L.) 1–27 (Humana Press, 2013). doi:10.1007/978-1-62703-541-5_1.

37. Wicki, A., Witzigmann, D., Balasubramanian, V. & Huwyler, J. Nanomedicine in cancer therapy: Challenges, opportunities, and clinical applications. *Journal of Controlled Release* **200**, 138–157 (2015).

38. Weller, G. E. R., Villanueva, F. S., Tom, E. M. & Wagner, W. R. Targeted ultrasound contrast agents: In vitro assessment of endothelial dysfunction and multi-targeting to ICAM-1 and sialyl Lewisx. *Biotechnology and Bioengineering* **92**, 780–788 (2005).

39. Afonin, K. A. *et al.* Activation of different split functionalities on re-association of RNA–DNA hybrids. *Nature Nanotechnology* **8**, 296–304 (2013).

40. Afonin, K. A. *et al.* Triggering of RNA Interference with RNA–RNA, RNA–DNA, and DNA–RNA Nanoparticles. *ACS Nano* **9**, 251–259 (2015).

41. Li, S. *et al.* A DNA nanorobot functions as a cancer therapeutic in response to a molecular trigger in vivo. *Nat. Biotechnol.* **36**, 258–264 (2018).

42. Yu, B., Tai, H. C., Xue, W., Lee, L. J. & Lee, R. J. Receptor-targeted nanocarriers for therapeutic delivery to cancer. *Molecular Membrane Biology* **27**, 286–298 (2010).

43. Dhand, C. *et al.* Role of size of drug delivery carriers for pulmonary and intravenous administration with emphasis on cancer therapeutics and lung-targeted drug delivery. *RSC Adv.* **4**, 32673–32689 (2014).

44. Hua, S. Targeting sites of inflammation: intercellular adhesion molecule-1 as a target for novel inflammatory therapies. *Front Pharmacol* **4**, 127 (2013).

45. Kolhar, P. *et al.* Using shape effects to target antibody-coated nanoparticles to lung and brain endothelium. *PNAS* **110**, 10753–10758 (2013).

46. Cho, Y. W., Kim, J.-D. & Park, K. Polycation gene delivery systems: escape from endosomes to cytosol. *Journal of Pharmacy and Pharmacology* **55**, 721–734 (2003).

47. Barnaby, S. N., Lee, A. & Mirkin, C. A. Probing the inherent stability of siRNA immobilized on nanoparticle constructs. *Proceedings of the National Academy of Sciences* **111**, 9739–9744 (2014).

48. Biswas, S. & Torchilin, V. Dendrimers for siRNA Delivery. *Pharmaceuticals* **6**, 161–183 (2013).

49. Guo, P., Yang, J., Jia, D., Moses, M. A. & Auguste, D. T. ICAM-1-Targeted, Lcn2 siRNA-Encapsulating Liposomes are Potent Anti-angiogenic Agents for Triple Negative Breast Cancer. *Theranostics* **6**, 1–13 (2016).

50. Ahmad, A. *et al.* Novel endosomolytic peptides for enhancing gene delivery in nanoparticles. *Biochimica et Biophysica Acta (BBA) - Biomembranes* **1848**, 544–553 (2015).

51. Mout, R., Ray, M., Lee, Y.-W., Scaletti, F. & Rotello, V. M. In Vivo Delivery of CRISPR/Cas9 for Therapeutic Gene Editing: Progress and Challenges. *Bioconjugate Chemistry* **28**, 880–884 (2017).

52. Sun, W. *et al.* Self-assembled DNA nanoclews for the efficient delivery of CRISPR-Cas9 for genome editing. *Angew. Chem. Int. Ed. Engl.* **54**, 12029–12033 (2015).

53. Tan, G.-R., Feng, S.-S. & Leong, D. T. The reduction of anti-cancer drug antagonism by the spatial protection of drugs with PLA–TPGS nanoparticles. *Biomaterials* **35**, 3044–3051 (2014).

54. Deodhar, G. V., Adams, M. L. & Trewyn, B. G. Controlled release and intracellular protein delivery from mesoporous silica nanoparticles. *Biotechnology Journal* **12**, 1600408 (2017).

55. Ghaffarian, R., Bhowmick, T. & Muro, S. Transport of nanocarriers across gastrointestinal epithelial cells by a new transcellular route induced by targeting ICAM-1. *Journal of controlled release* **163**, 25–33 (2012).

56. Ghaffarian, R., Pérez-Herrero, E., Oh, H., Raghavan, S. R. & Muro, S. Targeted Oral Drug Delivery: Chitosan–Alginate Microcapsules Provide Gastric Protection and Intestinal Release of ICAM-1-Targeting Nanocarriers, Enabling GI Targeting In Vivo (Adv. Funct. Mater. 20/2016). *Advanced Functional Materials* **26**, 3373–3373 (2016).

57. Campolongo, M. J., Tan, S. J., Xu, J. & Luo, D. DNA nanomedicine: Engineering DNA as a polymer for therapeutic and diagnostic applications. *Advanced Drug Delivery Reviews* **62**, 606–616 (2010).

58. Muro, S. A DNA device that mediates selective endosomal escape and intracellular delivery of drugs and biologicals. *Advanced functional materials* **24**, 2899–2906 (2014).

59. Muro, S. Alterations in Cellular Processes Involving Vesicular Trafficking and Implications in Drug Delivery. *Biomimetics* **3**, 19 (2018).

60. Muro, S. & Muzykantov, V. R. Design parameters modulating intracellular drug delivery: anchoring to specific cellular epitopes, carrier geometry, and use of auxiliary pharmacological agents. *Organelle-Specific Pharmaceutical Nanotechnology* 449–474 (2010).

61. Liu, X. *et al.* A DNA Nanostructure Platform for Directed Assembly of Synthetic Vaccines. *Nano Letters* **12**, 4254–4259 (2012).

62. Dejana, E. Endothelial cell-cell junctions: happy together. *Nat. Rev. Mol. Cell Biol.* **5**, 261–270 (2004).

63. Stevens, T., Garcia, J. G., Shasby, D. M., Bhattacharya, J. & Malik, A. B. Mechanisms regulating endothelial cell barrier function. *American Journal of Physiology-Lung Cellular and Molecular Physiology* **279**, L419–L422 (2000).

64. Koffie, R. M. *et al.* Nanoparticles enhance brain delivery of blood–brain barrier-impermeable probes for in vivo optical and magnetic resonance imaging. *PNAS* **108**, 18837–18842 (2011).

65. Lane, L. A., Qian, X., Smith, A. M. & Nie, S. Physical Chemistry of Nanomedicine: Understanding the Complex Behaviors of Nanoparticles in Vivo. *Annual Review of Physical Chemistry* **66**, 521–547 (2015).

66. Cao, J. *et al.* The effects of ligand valency and density on the targeting ability of multivalent nanoparticles based on negatively charged chitosan nanoparticles. *Colloids and Surfaces B: Biointerfaces* **161**, 508–518 (2018).

67. Elias, D. R., Poloukhtine, A., Popik, V. & Tsourkas, A. Effect of ligand density, receptor density, and nanoparticle size on cell targeting. *Nanomedicine* **9**, 194–201 (2013).

68. Bastings, M. M. C. *et al.* Modulation of the Cellular Uptake of DNA Origami through Control over Mass and Shape. *Nano Letters* **18**, 3557–3564 (2018).

69. Mikkilä, J. *et al.* Virus-Encapsulated DNA Origami Nanostructures for Cellular Delivery. *Nano Lett.* **14**, 2196–2200 (2014).

70. Blanco, E., Shen, H. & Ferrari, M. Principles of nanoparticle design for overcoming biological barriers to drug delivery. *Nat Biotechnol* **33**, 941–951 (2015).

71. Hu, Q., Li, H., Wang, L., Gu, H. & Fan, C. DNA Nanotechnology-Enabled Drug Delivery Systems. *Chemical Reviews* (2018) doi:10.1021/acs.chemrev.7b00663.

72. Chen, Y.-J., Groves, B., Muscat, R. A. & Seelig, G. DNA nanotechnology from the test tube to the cell. *Nature Nanotechnology* **10**, 748–760 (2015).

73. Keum, J.-W. & Bermudez, H. DNA-based delivery vehicles: pH-controlled disassembly and cargo release. *Chemical Communications* **48**, 12118 (2012).

74. Rothemund, P. W. K. Folding DNA to create nanoscale shapes and patterns. *Nature* **440**, 297–302 (2006).

75. Lee, H. *et al.* Molecularly self-assembled nucleic acid nanoparticles for targeted in vivo siRNA delivery. *Nature Nanotechnology* **7**, 389–393 (2012).

76. Afonin, K. A. *et al.* Multifunctional RNA Nanoparticles. *Nano Letters* **14**, 5662–5671 (2014).

77. Mariottini, D., Idili, A., Vallée-Bélisle, A., Plaxco, K. W. & Ricci, F. A DNA Nanodevice That Loads and Releases a Cargo with Hemoglobin-Like Allosteric Control and Cooperativity. *Nano Lett.* **17**, 3225–3230 (2017).

78. Han, X., Zhou, Z., Yang, F. & Deng, Z. Catch and Release: DNA Tweezers that Can Capture, Hold, and Release an Object under Control. *J. Am. Chem. Soc.* **130**, 14414–14415 (2008).

79. Krishnan, S. *et al.* Molecular transport through large-diameter DNA nanopores. *Nat Commun* **7**, 12787 (2016).

80. Ijäs, H., Hakaste, I., Shen, B., Kostiainen, M. A. & Linko, V. Reconfigurable DNA Origami Nanocapsule for pH-Controlled Encapsulation and Display of Cargo. *ACS Nano* **13**, 5959–5967 (2019).

81. Bagalkot, V., Farokhzad, O. C., Langer, R. & Jon, S. An aptamer-doxorubicin physical conjugate as a novel targeted drug-delivery platform. *Angew. Chem. Int. Ed. Engl.* **45**, 8149–8152 (2006).

82. Zhang, K., Hao, L., Hurst, S. J. & Mirkin, C. A. Antibody-Linked Spherical Nucleic Acids for Cellular Targeting. *Journal of the American Chemical Society* **134**, 16488–16491 (2012).

83. Liu, J. *et al.* Multifunctional aptamer-based nanoparticles for targeted drug delivery to circumvent cancer resistance. *Biomaterials* **91**, 44–56 (2016).

84. Bhatia, D., Surana, S., Chakraborty, S., Koushika, S. P. & Krishnan, Y. A synthetic icosahedral DNA-based host–cargo complex for functional in vivo imaging. *Nature Communications* **2**, (2011).

85. Han, X. *et al.* Multivalent aptamer-modified tetrahedral DNA nanocage demonstrates high selectivity and safety for anti-tumor therapy. *Nanoscale* **11**, 339–347 (2019).

86. Timmins, P. Industry update: the latest developments in the field of therapeutic delivery, 1–31 December 2018. *Therapeutic Delivery* **10**, 215–226 (2019).

87. Schüller, V. J. *et al.* Cellular Immunostimulation by CpG-Sequence-Coated DNA Origami Structures. *ACS Nano* **5**, 9696–9702 (2011).

88. Surana, S., Shenoy, A. R. & Krishnan, Y. Designing DNA nanodevices for compatibility with the immune system of higher organisms. *Nature Nanotechnology* **10**, 741–747 (2015).

89. Getts, R. C. & Bowers, J. The 3DNA® Platform for Targeted Drug Delivery. *Drug Development* **16**, 6 (2016).

90. Huang, Y.-H. *et al.* Delivery of Therapeutics Targeting the mRNA-Binding Protein HuR Using 3DNA Nanocarriers Suppresses Ovarian Tumor Growth. *Cancer Res.* **76**, 1549–1559 (2016).

91. Gerhart, J. *et al.* Antibody-Conjugated, DNA-Based Nanocarriers Intercalated with Doxorubicin Eliminate Myofibroblasts in Explants of Human Lens Tissue. *J. Pharmacol. Exp. Ther.* **361**, 60–67 (2017).

92. Sawicki, J. A., Peng, W., Rhodes, K. & Getts, R. Abstract 700: Systemic administration of DNA nanoparticles containing the diphtheria toxin gene reduces pancreatic tumor load in mice. *Cancer Res* **74**, 700–700 (2014).

93. Gerhart, J. *et al.* Depletion of Myo/Nog Cells in the Lens Mitigates Posterior Capsule Opacification in Rabbits. *Invest. Ophthalmol. Vis. Sci.* **60**, 1813–1823 (2019).

94. Muro, S. *et al.* Slow intracellular trafficking of catalase nanoparticles targeted to ICAM-1 protects endothelial cells from oxidative stress. *American Journal of Physiology-Cell Physiology* **285**, C1339–C1347 (2003).

95. Calderon, A. J. *et al.* Optimizing endothelial targeting by modulating the antibody density and particle concentration of anti-ICAM coated carriers. *Journal of controlled release* **150**, 37–44 (2011).

96. Lanza, G. M. ICAM-1 and Nanomedicine: Nature's Doorway to the Extravascular Tissue Realm. *Arteriosclerosis, Thrombosis, and Vascular Biology* **32**, 1070–1071 (2012).

97. Haug, C. E. *et al.* A phase I trial of immunosuppression with anti-ICAM-1 (CD54) mAb in renal allograft recipients. *Transplantation* **55**, 766–772; discussion 772-773 (1993).

98. Muro, S. *et al.* Control of endothelial targeting and intracellular delivery of therapeutic enzymes by modulating the size and shape of ICAM-1-targeted carriers. *Molecular Therapy* **16**, 1450–1458 (2008).

99. Garnacho, C. *et al.* Delivery of acid sphingomyelinase in normal and niemann-pick disease mice using intercellular adhesion molecule-1-targeted polymer

nanocarriers. *Journal of Pharmacology and Experimental Therapeutics* **325**, 400–408 (2008).

100. Hsu, J. *et al.* Enhanced endothelial delivery and biochemical effects of α-galactosidase by ICAM-1-targeted nanocarriers for Fabry disease. *Journal of controlled release* **149**, 323–331 (2011).

101. Muro, S., Koval, M. & Muzykantov, V. Endothelial endocytic pathways: gates for vascular drug delivery. *Current vascular pharmacology* **2**, 281–299 (2004).

102. Papademetriou, J. *et al.* Comparative binding, endocytosis, and biodistribution of antibodies and antibody-coated carriers for targeted delivery of lysosomal enzymes to ICAM-1 versus transferrin receptor. *Journal of inherited metabolic disease* **36**, 467–477 (2013).

103. Muro, S. *et al.* A novel endocytic pathway induced by clustering endothelial ICAM-1 or PECAM-1. *Journal of cell science* **116**, 1599–1609 (2003).

104. Murciano, J.-C. *et al.* ICAM-directed vascular immunotargeting of antithrombotic agents to the endothelial luminal surface: Presented in part as posters at the American Thoracic Society (ATS) Meeting, May 5-10, 2000, Toronto, ON, Canada. *Blood* **101**, 3977–3984 (2003).

105. Rothlein, R., Dustin, M. L., Marlin, S. D. & Springer, T. A. A human intercellular adhesion molecule (ICAM-1) distinct from LFA-1. *J. Immunol.* **137**, 1270–1274 (1986).

106. Ward, P. A. Acute lung injury: how the lung inflammatory response works. *European Respiratory Journal* **22**, 22s–23s (2003).

107. Howard, M. *et al.* Vascular Targeting of Nanocarriers: Perplexing Aspects of the Seemingly Straightforward Paradigm. *ACS Nano* **8**, 4100–4132 (2014).

108. Muzykantov, V. R. Targeted therapeutics and nanodevices for vascular drug delivery: quo vadis? *IUBMB life* **63**, 583–585 (2011).

109. Galindo, S. M. & Ghaffarian, R. Targeted carriers for drug delivery across the gastrointestinal epithelium. (2014).

110. Roki, N. *et al.* Unprecedently high targeting specificity toward lung ICAM-1 using 3DNA nanocarriers. *Journal of Controlled Release* **305**, 41–49 (2019).

111. Fenton, O. S., Olafson, K. N., Pillai, P. S., Mitchell, M. J. & Langer, R. Advances in Biomaterials for Drug Delivery. *Advanced Materials* **30**, 1705328 (2018).

112. Ragelle, H., Danhier, F., Préat, V., Langer, R. & Anderson, D. G. Nanoparticle-based drug delivery systems: a commercial and regulatory outlook as the field matures. *Expert Opinion on Drug Delivery* **14**, 851–864 (2017).

113. Ansar, M., Serrano, D., Papademetriou, I., Bhowmick, T. K. & Muro, S. Biological functionalization of drug delivery carriers to bypass size restrictions of receptor-mediated endocytosis independently from receptor targeting. *ACS nano* **7**, 10597–10611 (2013).

114. Bourdenx, M. *et al.* Nanoparticles restore lysosomal acidification defects: Implications for Parkinson and other lysosomal-related diseases. *Autophagy* **12**, 472–483 (2016).

115. Lundqvist, M. *et al.* Nanoparticle size and surface properties determine the protein corona with possible implications for biological impacts. *PNAS* **105**, 14265–14270 (2008).

116. Gonzalez Solveyra, E. & Szleifer, I. What is the role of curvature on the properties of nanomaterials for biomedical applications? *Wiley Interdiscip Rev Nanomed Nanobiotechnol* **8**, 334–354 (2016).

117. Longmire, M., Choyke, P. L. & Kobayashi, H. Clearance Properties of Nano-sized Particles and Molecules as Imaging Agents: Considerations and Caveats. *Nanomedicine (Lond)* **3**, 703–717 (2008).

118. Navya, P. N. & Daima, H. K. Rational engineering of physicochemical properties of nanomaterials for biomedical applications with nanotoxicological perspectives. *Nano Convergence* **3**, 1 (2016).

119. Zhao, Y.-X. *et al.* DNA Origami Delivery System for Cancer Therapy with Tunable Release Properties. *ACS Nano* **6**, 8684–8691 (2012).

120. Alkilany, A. M. *et al.* Ligand density on nanoparticles: A parameter with critical impact on nanomedicine. *Advanced Drug Delivery Reviews* **143**, 22–36 (2019).

121. Houck, K. S. & Huang, L. The role of multivalency in antibody mediated liposome targeting. *Biochemical and Biophysical Research Communications* **145**, 1205–1210 (1987).

122. Fung, K. Y. Y., Fairn, G. D. & Lee, W. L. Transcellular vesicular transport in epithelial and endothelial cells: Challenges and opportunities. *Traffic* **19**, 5–18 (2018).

123. Cheng, J. *et al.* Formulation of functionalized PLGA–PEG nanoparticles for in vivo targeted drug delivery. *Biomaterials* **28**, 869–876 (2007).

124. Farokhzad, O. C. *et al.* Targeted nanoparticle-aptamer bioconjugates for cancer chemotherapy in vivo. *Proceedings of the National Academy of Sciences* **103**, 6315–6320 (2006).

125. Foroozandeh, P. & Aziz, A. A. Insight into Cellular Uptake and Intracellular Trafficking of Nanoparticles. *Nanoscale Res Lett* **13**, (2018).

126. Fakhari, A., Baoum, A., Siahaan, T. J., Le, K. B. & Berkland, C. Controlling Ligand Surface Density Optimizes Nanoparticle Binding to ICAM-1. *Journal of Pharmaceutical Sciences* **100**, 1045–1056 (2011).

127. Wang, S. & E. Dormidontova, E. Nanoparticle targeting using multivalent ligands : computer modeling. *Soft Matter* **7**, 4435–4445 (2011).

128. Shen, B.-Q. *et al.* Conjugation site modulates the in vivo stability and therapeutic activity of antibody-drug conjugates. *Nature biotechnology* **30**, 184 (2012).

129. Choi, K.-S. *et al.* Inflammation-Specific T1 Imaging Using Anti-Intercellular Adhesion Molecule 1 Antibody-Conjugated Gadolinium Diethylenetriaminepentaacetic Acid. *Mol Imaging* **6**, 7290.2007.00005 (2007).

130. Muro, S. *et al.* Control of endothelial targeting and intracellular delivery of therapeutic enzymes by modulating the size and shape of ICAM-1-targeted carriers. *Molecular Therapy* **16**, 1450–1458 (2008).

131. Han, J. *et al.* Acute and chronic shear stress differently regulate endothelial internalization of nanocarriers targeted to platelet-endothelial cell adhesion molecule-1. *Acs Nano* **6**, 8824–8836 (2012).

132. Carboni, E. J. The Margination and Transport of Particles in Blood Flow. 135.

133. Gait, M. J. *et al.* Nucleic acids: new life, new materials. *Organic & Biomolecular Chemistry* **11**, 2058 (2013).

134. Han, S. *et al.* Gold and Hairpin DNA Functionalization of Upconversion Nanocrystals for Imaging and In Vivo Drug Delivery. *Advanced Materials* **29**, 1700244 (2017).

135. Miyata, K. *et al.* Enhanced transfection with silica-coated polyplexes loading plasmid DNA. *Biomaterials* **31**, 4764–4770 (2010).

136. Yan, J. *et al.* Growth and Origami Folding of DNA on Nanoparticles for High-Efficiency Molecular Transport in Cellular Imaging and Drug Delivery. *Angewandte Chemie International Edition* **54**, 2431–2435 (2015).

137. Charbgoo, F. *et al.* MUC1 aptamer-targeted DNA micelles for dual tumor therapy using doxorubicin and KLA peptide. *Nanomedicine: Nanotechnology, Biology and Medicine* **14**, 685–697 (2018).

138. Sang Yoo, H. & Gwan Park, T. Biodegradable nanoparticles containing protein-fatty acid complexes for oral delivery of salmon calcitonin. *Journal of Pharmaceutical Sciences* **93**, 488–495 (2004).

139. Rosi, N. L. Oligonucleotide-Modified Gold Nanoparticles for Intracellular Gene Regulation. *Science* **312**, 1027–1030 (2006).

140. Zhao, Y. *et al.* Copper-64-alloyed gold nanoparticles for cancer imaging: improved radiolabel stability and diagnostic accuracy. *Angew. Chem. Int. Ed. Engl.* **53**, 156–159 (2014).

141. Willoughby, J. L. S. *et al.* Evaluation of GalNAc-siRNA Conjugate Activity in Pre-clinical Animal Models with Reduced Asialoglycoprotein Receptor Expression. *Molecular Therapy* **26**, 105–114 (2018).

142. Auvinen, H. *et al.* Protein Coating of DNA Nanostructures for Enhanced Stability and Immunocompatibility. *Advanced Healthcare Materials* **6**, 1700692 (2017).

143. Tiwari, S., Gupta, M. & Vyas, S. P. Nanocarrier Mediated Cytosolic Delivery of Drug, DNA and Proteins. *Proc. Natl. Acad. Sci., India, Sect. B Biol. Sci.* **82**, 127–150 (2012).

144. Zhang, X.-Y., Dinh, A., Cronin, J., Li, S.-C. & Reiser, J. Cellular uptake and lysosomal delivery of galactocerebrosidase tagged with the HIV Tat protein transduction domain. *Journal of neurochemistry* **104**, 1055–1064 (2008).

145. Kornbrust, D. *et al.* Oligo Safety Working Group Exaggerated Pharmacology Subcommittee Consensus Document. *Nucleic Acid Therapeutics* **23**, 21–28 (2013).

146. Szeto, G. L. & Lavik, E. B. Materials design at the interface of nanoparticles and innate immunity. *Journal of Materials Chemistry B* **4**, 1610–1618 (2016).

147. Huang, K., Voss, B., Kumar, D., Hamm, H. E. & Harth, E. Dendritic Molecular Transporters Provide Control of Delivery to Intracellular Compartments. *Bioconjugate Chem.* **18**, 403–409 (2007).

148. Stylianopoulos, T. Intelligent drug delivery systems for the treatment of solid tumors. *European Journal of Nanomedicine* **8**, (2016).

149. Khondee, S., Baoum, A., Siahaan, T. J. & Berkland, C. Calcium condensed LABL-TAT complexes effectively target gene delivery to ICAM-1 expressing cells. *Molecular pharmaceutics* **8**, 788–798 (2011).

150. Kiseleva, R. Yu. *et al.* Targeting therapeutics to endothelium: are we there yet? *Drug Delivery and Translational Research* **8**, 883–902 (2018).

151. Grove, J. & Marsh, M. The cell biology of receptor-mediated virus entry. *J Cell Biol* **195**, 1071–1082 (2011).

152. Muro, S. *et al.* Endothelial targeting of high-affinity multivalent polymer nanocarriers directed to intercellular adhesion molecule 1. *Journal of Pharmacology and Experimental Therapeutics* **317**, 1161–1169 (2006).

153. Schuchman, E. H. & Muro, S. The development of enzyme replacement therapy for lysosomal diseases: Gaucher disease and beyond. *GAUCHER* (2006).

154. Muro, S. *et al.* Control of intracellular trafficking of ICAM-1-targeted nanocarriers by endothelial Na+/H+ exchanger proteins. *American Journal of Physiology-Lung Cellular and Molecular Physiology* **290**, L809–L817 (2006).

155. Sakhalkar, H. S. *et al.* Leukocyte-inspired biodegradable particles that selectively and avidly adhere to inflamed endothelium in vitro and in vivo. *Proceedings of the National Academy of Sciences* **100**, 15895–15900 (2003).

156. Anselmo, A. C. *et al.* Delivering Nanoparticles to Lungs while Avoiding Liver and Spleen through Adsorption on Red Blood Cells. *ACS Nano* **7**, 11129–11137 (2013).

157. Ehrenberg, M. S., Friedman, A. E., Finkelstein, J. N., Oberdörster, G. & McGrath, J. L. The influence of protein adsorption on nanoparticle association with cultured endothelial cells. *Biomaterials* **30**, 603–610 (2009).

158. Behzadi, S. *et al.* Cellular Uptake of Nanoparticles: Journey Inside the Cell. *Chem Soc Rev* **46**, 4218–4244 (2017).

159. Palecanda, A. *et al.* Role of the Scavenger Receptor MARCO in Alveolar Macrophage Binding of Unopsonized Environmental Particles. *The Journal of Experimental Medicine* **189**, 1497–1506 (1999).

160. Braet, F. & Wisse, E. Structural and functional aspects of liver sinusoidal endothelial cell fenestrae: a review. *Comp Hepatol* **1**, 1 (2002).

161. Hoshyar, N., Gray, S., Han, H. & Bao, G. The effect of nanoparticle size on in vivo pharmacokinetics and cellular interaction. *Nanomedicine (Lond)* **11**, 673–692 (2016).

162. Ta, H. T., Truong, N. P., Whittaker, A. K., Davis, T. P. & Peter, K. The effects of particle size, shape, density and flow characteristics on particle margination to vascular walls in cardiovascular diseases. *Expert Opinion on Drug Delivery* **15**, 33–45 (2018).

163. Serrano, D., Manthe, R. L., Paul, E., Chadha, R. & Muro, S. How carrier size and valency modulate receptor-mediated signaling: understanding the link between binding and endocytosis of ICAM-1-targeted carriers. *Biomacromolecules* **17**, 3127–3137 (2016).

164. Jin, Z.-H. *et al.* In vivo optical imaging of integrin αV-β3 in mice using multivalent or monovalent cRGD targeting vectors. *Molecular Cancer* **6**, 41 (2007).

165. V. Munsell, E., L. Ross, N. & O. Sullivan, M. Journey to the Center of the Cell: Current Nanocarrier Design Strategies Targeting Biopharmaceuticals to the Cytoplasm and Nucleus. *Current Pharmaceutical Design* **22**, 1227–1244 (2016).

166. Saha, B., Evers, T. H. & Prins, M. W. How antibody surface coverage on nanoparticles determines the activity and kinetics of antigen capturing for biosensing. *Analytical chemistry* **86**, 8158–8166 (2014).

167. Liu, J. *et al.* Computational model for nanocarrier binding to endothelium validated using in vivo, in vitro, and atomic force microscopy experiments. *Proc Natl Acad Sci U S A* **107**, 16530–16535 (2010).

168. Muzykantov, V. R. Biomedical aspects of targeted delivery of drugs to pulmonary endothelium. *Expert Opin Drug Deliv* **2**, 909–926 (2005).

169. Ho, K., Lapitsky, Y., Shi, M. & Shoichet, M. S. Tunable immunonanoparticle binding to cancer cells: thermodynamic analysis of targeted drug delivery vehicles. *Soft Matter* **5**, 1074–1080 (2009).

170. Calderon, A. J., Muzykantov, V., Muro, S. & Eckmann, D. M. Flow dynamics, binding and detachment of spherical carriers targeted to ICAM-1 on endothelial cells. *Biorheology* **46**, 323–341 (2009).

171. Farokhirad, S., Bradley, R. P. & Radhakrishnan, R. Thermodynamic analysis of multivalent binding of functionalized nanoparticles to membrane surface reveals the importance of membrane entropy and nanoparticle entropy in adhesion of flexible nanoparticles. *Soft Matter* **15**, 9271–9286 (2019).

172. Zern, B. J. *et al.* Reduction of Nanoparticle Avidity Enhances the Selectivity of Vascular Targeting and PET Detection of Pulmonary Inflammation. *ACS Nano* **7**, 2461–2469 (2013).

173. Qureshi, O. S. *et al.* Constitutive Clathrin-mediated Endocytosis of CTLA-4 Persists during T Cell Activation. *Journal of Biological Chemistry* **287**, 9429–9440 (2012).

174. Qureshi, O. S. *et al.* Trans-Endocytosis of CD80 and CD86: A Molecular Basis for the Cell-Extrinsic Function of CTLA-4. *Science* **332**, 600–603 (2011).

175. You, J.-O., Guo, P. & Auguste, D. T. A Drug-Delivery Vehicle Combining the Targeting and Thermal Ablation of HER2+ Breast-Cancer Cells with Triggered Drug Release. *Angewandte Chemie International Edition* **52**, 4141–4146 (2013).

176. Altschuler, Y. *et al.* Clathrin-mediated Endocytosis of MUC1 Is Modulated by Its Glycosylation State. *Molecular Biology of the Cell* **11**, 819–831 (2000).

177. Toy, R., Hayden, E., Shoup, C., Baskaran, H. & Karathanasis, E. The effects of particle size, density and shape on margination of nanoparticles in microcirculation. *Nanotechnology* **22**, 115101 (2011).

178. Ye, H., Shen, Z., Yu, L., Wei, M. & Li, Y. Manipulating nanoparticle transport within blood flow through external forces: an exemplar of mechanics in nanomedicine. *Proc. Math. Phys. Eng. Sci.* **474**, 20170845 (2018).

179. Müller, K., Fedosov, D. A. & Gompper, G. Margination of micro- and nano-particles in blood flow and its effect on drug delivery. *Scientific Reports* **4**, 4871 (2014).

180. Lalor, P., Lai, W., Curbishley, S., Shetty, S. & Adams, D. Human hepatic sinusoidal endothelial cells can be distinguished by expression of phenotypic markers related to their specialised functions in vivo. *World J Gastroenterol* **12**, 5429–5439 (2006).

181. Alexis, F., Pridgen, E., Molnar, L. K. & Farokhzad, O. C. Factors affecting the clearance and biodistribution of polymeric nanoparticles. *Mol. Pharm.* **5**, 505–515 (2008).

182. Rosenblum, D., Joshi, N., Tao, W., Karp, J. M. & Peer, D. Progress and challenges towards targeted delivery of cancer therapeutics. *Nature Communications* **9**, 1410 (2018).

183. Wilhelm, S. *et al.* Analysis of nanoparticle delivery to tumours. *Nature Reviews Materials* **1**, 16014 (2016).

184. Nascimento, A. V. *et al.* Biodistribution and pharmacokinetics of *Mad2* siRNA-loaded EGFR-targeted chitosan nanoparticles in cisplatin sensitive and resistant lung cancer models. *Nanomedicine* **11**, 767–781 (2016).

185. Baker, J. R. Dendrimer-based nanoparticles for cancer therapy. *Hematology* **2009**, 708–719 (2009).

186. Hu, Q., Wang, S., Wang, L., Gu, H. & Fan, C. DNA Nanostructure-Based Systems for Intelligent Delivery of Therapeutic Oligonucleotides. *Advanced Healthcare Materials* **7**, 1701153 (2018).

187. Goltry, S. *et al.* DNA topology influences molecular machine lifetime in human serum. *Nanoscale* **7**, 10382–10390 (2015).

188. Benson, E. *et al.* Effects of Design Choices on the Stiffness of Wireframe DNA Origami Structures. *ACS Nano* **12**, 9291–9299 (2018).

189. Andersen, E. S. *et al.* Self-assembly of a nanoscale DNA box with a controllable lid. *Nature* **459**, 73–76 (2009).

190. Giljohann, D. A., Seferos, D. S., Prigodich, A. E., Patel, P. C. & Mirkin, C. A. Gene Regulation with Polyvalent siRNA−Nanoparticle Conjugates. *Journal of the American Chemical Society* **131**, 2072–2073 (2009).

191. Perrault, S. D. & Shih, W. M. Virus-Inspired Membrane Encapsulation of DNA Nanostructures To Achieve In Vivo Stability. *ACS Nano* **8**, 5132–5140 (2014).

192. Roh, Y. H. *et al.* DNAsomes: Multifunctional DNA-Based Nanocarriers. *Small* **7**, 74–78 (2011).

193. Lacroix, A., Edwardson, T. G. W., Hancock, M. A., Dore, M. D. & Sleiman, H. F. Development of DNA Nanostructures for High-Affinity Binding to Human Serum Albumin. *J. Am. Chem. Soc.* **139**, 7355–7362 (2017).

194. Seferos, D. S., Prigodich, A. E., Giljohann, D. A., Patel, P. C. & Mirkin, C. A. Polyvalent DNA Nanoparticle Conjugates Stabilize Nucleic Acids. *Nano Letters* **9**, 308–311 (2009).

195. Shen, X. *et al.* Visualization of the intracellular location and stability of DNA origami with a label-free fluorescent probe. *Chem. Commun.* **48**, 11301–11303 (2012).

196. Taghdisi, S. M., Danesh, N. M., Ramezani, M., Yazdian-Robati, R. & Abnous, K. A Novel AS1411 Aptamer-Based Three-Way Junction Pocket DNA Nanostructure Loaded with Doxorubicin for Targeting Cancer Cells in Vitro and in Vivo. *Molecular Pharmaceutics* **15**, 1972–1978 (2018).

197. Halley, P. D. *et al.* Daunorubicin-Loaded DNA Origami Nanostructures Circumvent Drug-Resistance Mechanisms in a Leukemia Model. *Small* **12**, 308–320 (2016).

198. Horkay, F. & Basser, P. J. DNA gels: pH mediated structural changes. 2 (2009).

199. Murakami, Y. & Maeda, M. DNA-Responsive Hydrogels That Can Shrink or Swell. *Biomacromolecules* **6**, 2927–2929 (2005).

200. Bath, J. & Turberfield, A. J. DNA nanomachines. *Nature Nanotechnology* **2**, 275–284 (2007).

201. Amir, Y. *et al.* Universal computing by DNA origami robots in a living animal. *Nature Nanotechnology* **9**, 353–357 (2014).

202. Erben, C. M., Goodman, R. P. & Turberfield, A. J. Single-Molecule Protein Encapsulation in a Rigid DNA Cage. *Angewandte Chemie International Edition* **45**, 7414–7417 (2006).

203. Ottaviani, A. *et al.* Engineering a responsive DNA triple helix into an octahedral DNA nanostructure for a reversible opening/closing switching mechanism: a computational and experimental integrated study. *Nucleic Acids Res* **46**, 9951–9959 (2018).

204. Roh, Y. H., Ruiz, R. C. H., Peng, S., Lee, J. B. & Luo, D. Engineering DNA-based functional materials. *Chemical Society Reviews* **40**, 5730 (2011).

205. Wang, P. *et al.* Visualization of the Cellular Uptake and Trafficking of DNA Origami Nanostructures in Cancer Cells. *Journal of the American Chemical Society* **140**, 2478–2484 (2018).

206. Howorka, S. Building membrane nanopores. *Nature Nanotechnology* **12**, 619–630 (2017).

207. Khisamutdinov, E. F. *et al.* Enhancing immunomodulation on innate immunity by shape transition among RNA triangle, square and pentagon nanovehicles. *Nucleic Acids Research* **42**, 9996–10004 (2014).

208. Nishikawa, M. *et al.* Biodegradable CpG DNA hydrogels for sustained delivery of doxorubicin and immunostimulatory signals in tumor-bearing mice. *Biomaterials* **32**, 488–494 (2011).

209. Taghdisi, S. M. *et al.* Double targeting and aptamer-assisted controlled release delivery of epirubicin to cancer cells by aptamers-based dendrimer in vitro and in vivo. *Eur J Pharm Biopharm* **102**, 152–158 (2016).

210. Kim, K.-R. *et al.* Drug delivery by a self-assembled DNA tetrahedron for overcoming drug resistance in breast cancer cells. *Chemical Communications* **49**, 2010 (2013).

211. Chang, M., Yang, C.-S. & Huang, D.-M. Aptamer-Conjugated DNA Icosahedral Nanoparticles As a Carrier of Doxorubicin for Cancer Therapy. *ACS Nano* **5**, 6156–6163 (2011).

212. Huang, Y., Huang, W., Chan, L., Zhou, B. & Chen, T. A multifunctional DNA origami as carrier of metal complexes to achieve enhanced tumoral delivery and nullified systemic toxicity. *Biomaterials* **103**, 183–196 (2016).

213. Kocabey, S. *et al.* Cellular Uptake of Tile-Assembled DNA Nanotubes. *Nanomaterials* **5**, 47–60 (2014).

214. Bujold, K. E., Lacroix, A. & Sleiman, H. F. DNA Nanostructures at the Interface with Biology. *Chem* **4**, 495–521 (2018).

215. Jensen, S. A. *et al.* Spherical Nucleic Acid Nanoparticle Conjugates as an RNAi-Based Therapy for Glioblastoma. *Science Translational Medicine* **5**, 209ra152-209ra152 (2013).

216. Rink, J. S. *et al.* Knockdown of Intraislet IKKβ by Spherical Nucleic Acid Conjugates Prevents Cytokine-Induced Injury and Enhances Graft Survival: *Transplantation Journal* **96**, 877–884 (2013).

217. Ko, S., Liu, H., Chen, Y. & Mao, C. DNA Nanotubes as Combinatorial Vehicles for Cellular Delivery. *Biomacromolecules* **9**, 3039–3043 (2008).

218. Charoenphol, P. & Bermudez, H. Aptamer-Targeted DNA Nanostructures for Therapeutic Delivery. *Mol. Pharmaceutics* **11**, 1721–1725 (2014).

219. Santos, T. dos, Varela, J., Lynch, I., Salvati, A. & Dawson, K. A. Effects of Transport Inhibitors on the Cellular Uptake of Carboxylated Polystyrene Nanoparticles in Different Cell Lines. *PLOS ONE* **6**, e24438 (2011).

220. Patel, P. C. *et al.* Scavenger Receptors Mediate Cellular Uptake of Polyvalent Oligonucleotide-Functionalized Gold Nanoparticles. *Bioconjugate Chemistry* **21**, 2250–2256 (2010).

221. Rosales, C. & Uribe-Querol, E. Phagocytosis: A Fundamental Process in Immunity. *BioMed Research International* https://www.hindawi.com/journals/bmri/2017/9042851/ (2017) doi:10.1155/2017/9042851.

222. PrabhuDas, M. R. *et al.* A Consensus Definitive Classification of Scavenger Receptors and Their Roles in Health and Disease. *J. Immunol.* **198**, 3775–3789 (2017).

223. Hemmi, H. *et al.* A Toll-like receptor recognizes bacterial DNA. *Nature* **408**, 740–745 (2000).

224. Lehmann, M. J. & Sczakiel, G. Spontaneous uptake of biologically active recombinant DNA by mammalian cells via a selected DNA segment. *Gene Ther.* **12**, 446–451 (2005).

225. Vindigni, G. *et al.* Receptor-Mediated Entry of Pristine Octahedral DNA Nanocages in Mammalian Cells. *ACS Nano* **10**, 5971–5979 (2016).

226. Kustanovich, A., Schwartz, R., Peretz, T. & Grinshpun, A. Life and death of circulating cell-free DNA. *Cancer Biol Ther* **20**, 1057–1067 (2019).

227. Capaldi, S., Getts, R. C. & Jayasena, S. D. Signal amplification through nucleotide extension and excision on a dendritic DNA platform. *Nucleic Acids Res* **28**, e21–e21 (2000).

228. Gerhart, J. *et al.* DNA Dendrimers Localize Myod mRNA in Presomitic Tissues of the Chick Embryo. *J Cell Biol* **149**, 825–834 (2000).

229. Kadushin, J. & Getts, R. C. Long-Acting DNA Dendrimers and Methods Thereof. (2012).

230. Leong, H. S. *et al.* On the issue of transparency and reproducibility in nanomedicine. *Nature Nanotechnology* **14**, 629–635 (2019).

231. Agrahari, V. & Agrahari, V. Facilitating the translation of nanomedicines to a clinical product: challenges and opportunities. *Drug Discovery Today* **23**, 974–991 (2018).

232. Nilsen, T. W., Grayzel, J. & Prensky, W. Dendritic nucleic acid structures. *Journal of theoretical biology* **187**, 273–284 (1997).

233. Mora, J. R. & Getts, R. C. High-sensitivity detection methods for low-abundance RNA species: applications for functional genomics research. *Expert Review of Molecular Diagnostics* http://link.galegroup.com/apps/doc/A232493540/AONE?sid=googlescholar (2007).

234. Muro-Galindo, S. & Muzykantov, V. R. Targeted carriers for intracellular drug delivery. (2010).

235. Muro-Galindo, S. & Muzykantov, V. R. Targeted carriers for intracellular drug delivery. (2017).

236. Liu, Y., Tseng, Y. & Huang, L. Biodistribution Studies of Nanoparticles Using Fluorescence Imaging: A Qualitative or Quantitative Method? *Pharmaceutical Research* **29**, 3273–3277 (2012).

237. Garnacho, C., Dhami, R., Solomon, M., Schuchman, E. H. & Muro, S. Enhanced delivery and effects of acid sphingomyelinase by ICAM-1-targeted nanocarriers in type B Niemann-Pick disease mice. *Molecular Therapy* **25**, 1686–1696 (2017).

238. Kim, J. *et al.* Co-coating of receptor-targeted drug nanocarriers with anti-phagocytic moieties enhances specific tissue uptake versus non-specific phagocytic clearance. *Biomaterials* **147**, 14–25 (2017).

239. Jo, J.-H. *et al.* Recycling and LFA-1-dependent trafficking of ICAM-1 to the immunological synapse. *Journal of cellular biochemistry* **111**, 1125–1137 (2010).

240. Serrano, D. & Muro, S. *Endothelial cell adhesion molecules and drug delivery applications*. (CRC Press: Boca Raton, FL, 2015).

241. Papademetriou, I., Tsinas, Z., Hsu, J. & Muro, S. Combination-targeting to multiple endothelial cell adhesion molecules modulates binding, endocytosis, and in vivo biodistribution of drug nanocarriers and their therapeutic cargoes. *Journal of Controlled Release* **188**, 87–98 (2014).

242. Coll Ferrer, M. C. *et al.* ICAM-1 Targeted Nanogels Loaded with Dexamethasone Alleviate Pulmonary Inflammation. *PLoS ONE* **9**, e102329 (2014).

243. Park, S. *et al.* Self-assembled nanoplatform for targeted delivery of chemotherapy agents via affinity-regulated molecular interactions. *Biomaterials* **31**, 7766–7775 (2010).

244. Neumann, B. *et al.* Mechanisms of acute inflammatory lung injury induced by abdominal sepsis. *International Immunology* **11**, 217–227 (1999).

245. Rappaport, J., Manthe, R. L., Solomon, M., Garnacho, C. & Muro, S. A comparative study on the alterations of endocytic pathways in multiple lysosomal storage disorders. *Molecular pharmaceutics* **13**, 357–368 (2016).

246. Ghaffarian, R., Roki, N., Abouzeid, A., Vreeland, W. & Muro, S. Intra-and trans-cellular delivery of enzymes by direct conjugation with non-multivalent anti-ICAM molecules. *Journal of Controlled Release* **238**, 221–230 (2016).

247. Manthe, R. L. & Muro, S. Lysosomes and nanotherapeutics: diseases, treatments, and side effects. in *HANDBOOK OF NANOBIOMEDICAL RESEARCH: Fundamentals, Applications and Recent Developments: Volume 2. Applications in Therapy* 261–305 (World Scientific, 2014).

248. Serrano, D., Bhowmick, T., Chadha, R., Garnacho, C. & Muro, S. Intercellular adhesion molecule 1 engagement modulates sphingomyelinase and ceramide, supporting uptake of drug carriers by the vascular endothelium. *Arteriosclerosis, thrombosis, and vascular biology* **32**, 1178–1185 (2012).

249. Ghaffarian, R. & Muro, S. Distinct subcellular trafficking resulting from monomeric vs multimeric targeting to endothelial ICAM-1: implications for drug delivery. *Molecular pharmaceutics* **11**, 4350–4362 (2014).

250. Ghaffarian, R., Pérez-Herrero, E., Oh, H., Raghavan, S. R. & Muro, S. Chitosan–Alginate Microcapsules Provide Gastric Protection and Intestinal Release of ICAM-1-Targeting Nanocarriers, Enabling GI Targeting In Vivo. *Advanced functional materials* **26**, 3382–3393 (2016).

251. Demanèche, S., Jocteur-Monrozier, L., Quiquampoix, H. & Simonet, P. Evaluation of biological and physical protection against nuclease degradation of clay-bound plasmid DNA. *Appl. Environ. Microbiol.* **67**, 293–299 (2001).

252. Zhang, Y., Huo, M., Zhou, J. & Xie, S. PKSolver: An add-in program for pharmacokinetic and pharmacodynamic data analysis in Microsoft Excel. *Computer methods and programs in biomedicine* **99**, 306–314 (2010).

253. Silva Lima, B. & Videira, M. A. Toxicology and Biodistribution: The Clinical Value of Animal Biodistribution Studies. *Molecular Therapy - Methods & Clinical Development* **8**, 183–197 (2018).

254. Arms, L. *et al.* Advantages and Limitations of Current Techniques for Analyzing the Biodistribution of Nanoparticles. *Frontiers in Pharmacology* **9**, (2018).

255. Sivaraman, T., Kumar, T. K., Jayaraman, G. & Yu, C. The mechanism of 2,2,2-trichloroacetic acid-induced protein precipitation. *J. Protein Chem.* **16**, 291–297 (1997).

256. Rajalingam, D., Loftis, C., Xu, J. J. & Kumar, T. K. S. Trichloroacetic acid-induced protein precipitation involves the reversible association of a stable partially structured intermediate. *Protein Sci* **18**, 980–993 (2009).

257. Spetz, J., Rudqvist, N. & Forssell-Aronsson, E. Biodistribution and dosimetry of free 211At, 125I- and 131I- in rats. *Cancer Biother. Radiopharm.* **28**, 657–664 (2013).

258. Spitzweg, C. *et al.* Expression of the sodium iodide symporter in human kidney. *Kidney Int.* **59**, 1013–1023 (2001).

259. Merlot, A. M., Kalinowski, D. S. & Richardson, D. R. Unraveling the mysteries of serum albumin—more than just a serum protein. *Frontiers in physiology* **5**, 299 (2014).

260. Harmatz, P. R., Walsh, M. K., Walker, W. A., Hanson, D. G. & Bloch, K. J. Trichloroacetic acid (TCA) precipitability of 125I in the blood of mice fed 125I. *Journal of immunological methods* **102**, 213–219 (1987).

261. Choi, C. H. J., Hao, L., Narayan, S. P., Auyeung, E. & Mirkin, C. A. Mechanism for the endocytosis of spherical nucleic acid nanoparticle conjugates. *Proceedings of the National Academy of Sciences* **110**, 7625–7630 (2013).

262. Muro, S. & Serrano, D. Endothelial cell adhesion molecules and drug delivery applications. in *Mechanobiology of the endothelium* 185–226 (CRC Press, Boca Raton, 2014).

263. Nourshargh, S., Hordijk, P. L. & Sixt, M. Breaching multiple barriers: leukocyte motility through venular walls and the interstitium. *Nature Reviews Molecular Cell Biology* **11**, 366–378 (2010).

264. Ley, K., Laudanna, C., Cybulsky, M. I. & Nourshargh, S. Getting to the site of inflammation: the leukocyte adhesion cascade updated. *Nat. Rev. Immunol.* **7**, 678–689 (2007).

265. Hofland, H. E., Shephard, L. & Sullivan, S. M. Formation of stable cationic lipid/DNA complexes for gene transfer. *PNAS* **93**, 7305–7309 (1996).

266. Hsu, J., Northrup, L., Bhowmick, T. & Muro, S. Enhanced delivery of α-glucosidase for Pompe disease by ICAM-1-targeted nanocarriers: comparative performance of a strategy for three distinct lysosomal storage disorders. *Nanomedicine: Nanotechnology, Biology and Medicine* **8**, 731–739 (2012).

267. Mohita Upadhyay, R. M. Design Considerations for Chemotherapeutic Drug Nanocarriers. *Pharmaceutica Analytica Acta* **05**, (2013).

268. Selzner, N. *et al.* ICAM-1 triggers liver regeneration through leukocyte recruitment and Kupffer cell–dependent release of TNF-α/IL-6 in mice. *Gastroenterology* **124**, 692–700 (2003).

269. Yusuf-Makagiansar, H., Anderson, M. E., Yakovleva, T. V., Murray, J. S. & Siahaan, T. J. Inhibition of LFA-1/ICAM-1 and VLA-4/VCAM-1 as a therapeutic approach to inflammation and autoimmune diseases. *Medicinal Research Reviews* **22**, 146–167 (2002).

270. Gratton, S. E. A. *et al.* The effect of particle design on cellular internalization pathways. *PNAS* **105**, 11613–11618 (2008).

271. Carver, L. A. & Schnitzer, J. E. Caveolae: mining little caves for new cancer targets. *Nature Reviews Cancer* **3**, 571–581 (2003).

272. Solomon, M. & Muro, S. Lysosomal enzyme replacement therapies: Historical development, clinical outcomes, and future perspectives. *Advanced drug delivery reviews* **118**, 109–134 (2017).

273. Purdie, L., Alexander, C., Spain, S. G. & Magnusson, J. P. Influence of Polymer Size on Uptake and Cytotoxicity of Doxorubicin-Loaded DNA–PEG Conjugates. *Bioconjugate Chemistry* **27**, 1244–1252 (2016).

274. Yang, D. *et al.* Novel DNA materials and their applications. *Wiley Interdiscip Rev Nanomed Nanobiotechnol* **2**, 648–669 (2010).

275. Greineder, C. F. *et al.* ICAM-1–targeted thrombomodulin mitigates tissue factor–driven inflammatory thrombosis in a human endothelialized microfluidic model. *Blood Advances* **1**, 1452–1465 (2017).

276. Marcos-Contreras, O. A. *et al.* Combining vascular targeting and the local first pass provides 100-fold higher uptake of ICAM-1-targeted vs untargeted nanocarriers in the inflamed brain. *Journal of Controlled Release* **301**, 54–61 (2019).

277. Marcos-Contreras, O. A. *et al.* Selective targeting of nanomedicine to inflamed cerebral vasculature to enhance the blood–brain barrier. *PNAS* (2020) doi:10.1073/pnas.1912012117.

278. Myerson, J. W. *et al.* Cross-linker-Modulated Nanogel Flexibility Correlates with Tunable Targeting to a Sterically Impeded Endothelial Marker. *ACS Nano* **13**, 11409–11421 (2019).

279. Kang, X.-Q. *et al.* Effective targeted therapy for drug-resistant infection by ICAM-1 antibody-conjugated TPGS modified β-Ga2O3:Cr3+ nanoparticles. *Theranostics* **9**, 2739–2753 (2019).

280. Genisphere Signs Collaborative Research, Option to License Agreement with MedImmune. *Genisphere* https://genisphere.com/news/genisphere-signs-collaborative-research-option-license-agreement-medimmune (2016).

281. Genisphere and AstraZeneca's MedImmune ink R&D, licensing deal. *FiercePharma* https://www.fiercepharma.com/drug-delivery/genisphere-and-astrazeneca-s-medimmune-ink-r-d-licensing-deal.

282. Iurescia, S., Fioretti, D. & Rinaldi, M. Targeting Cytosolic Nucleic Acid-Sensing Pathways for Cancer Immunotherapies. *Front Immunol* **9**, (2018).

283. Stein, S. C., Lam, E. & Falck-Pedersen, E. Cell-Specific Regulation of Nucleic Acid Sensor Cascades: a Controlling Interest in the Antiviral Response. *J Virol* **86**, 13303–13312 (2012).

284. Yu, L., Chen, Y. & Tooze, S. A. Autophagy pathway: cellular and molecular mechanisms. *Autophagy* **14**, 207–215 (2018).

285. El Kebir, D., József, L., Pan, W., Wang, L. & Filep, J. G. Bacterial DNA Activates Endothelial Cells and Promotes Neutrophil Adherence through TLR9 Signaling. *The Journal of Immunology* **182**, 4386–4394 (2009).

286. Byers, V. S. & Baldwin, R. W. Therapeutic strategies with monoclonal antibodies and immunoconjugates. *Immunology* **65**, 329–335 (1988).

287. Judge, A., McClintock, K., Phelps, J. R. & MacLachlan, I. Hypersensitivity and Loss of Disease Site Targeting Caused by Antibody Responses to PEGylated Liposomes. *Molecular Therapy* **13**, 328–337 (2006).